



저작자표시-비영리-변경금지 2.0 대한민국

이용자는 아래의 조건을 따르는 경우에 한하여 자유롭게

- 이 저작물을 복제, 배포, 전송, 전시, 공연 및 방송할 수 있습니다.

다음과 같은 조건을 따라야 합니다:



저작자표시. 귀하는 원저작자를 표시하여야 합니다.



비영리. 귀하는 이 저작물을 영리 목적으로 이용할 수 없습니다.



변경금지. 귀하는 이 저작물을 개작, 변형 또는 가공할 수 없습니다.

- 귀하는, 이 저작물의 재이용이나 배포의 경우, 이 저작물에 적용된 이용허락조건을 명확하게 나타내어야 합니다.
- 저작권자로부터 별도의 허가를 받으면 이러한 조건들은 적용되지 않습니다.

저작권법에 따른 이용자의 권리는 위의 내용에 의하여 영향을 받지 않습니다.

이것은 [이용허락규약\(Legal Code\)](#)을 이해하기 쉽게 요약한 것입니다.

[Disclaimer](#)

공학박사학위논문

**Multiscale Design and Fabrication of
Bioinspired Multifunctional
Superomniphobic Surfaces**

자연모사 기반 멀티스케일 다기능성
옴니포빅 표면의 설계 및 제작

2015 년 2 월

서울대학교 대학원

기계항공공학부

강 성 민

Abstract

In this thesis, we studied the multiscale design and fabrication method of superomniphobic surfaces using bio-inspired approaches for multifunctional device applications. The water and oil repellent surfaces are based on polymeric structural design with chemical/plasma treatment. Theoretical analysis for water and oil wetting behaviors is presented based on the microfluidics. Through the various properties such as omniphobicity, directional liquid sliding, self-cleaning and anti-reflection effect, the multiscale bio-inspired surfaces can demonstrate useful applications to industrial energy device fields.

First, we presented bio-inspired polymeric superomniphobic surfaces by using low-expertise yet robust over-etching fabrication process. The structure of gecko foot in nature has been used for various applications particularly in dry adhesive researches. However, we had an inspiration from the end tips of a gecko foot which have similar shape with the re-entrant structures. Using the conventional deep reactive ion etching process with silicon on insulator (SOI) wafer, we could make a wide-tip microstructure through the over-etching step at the etch-stop layer (SiO_2), and then replicate the structure on flexible and transparent polymer surfaces. To evaluate superomniphobic properties of fabricated polymer surfaces, we measured static contact angle and hysteresis from water ($\gamma_{lv} = 72.1 \text{ mN/m}$) to ethanol ($\gamma_{lv} = 22.3 \text{ mN/m}$). Additionally, the

transmittance and aging effect were analyzed for enhanced applicability.

Next, we developed overhang micro line arrays inspired from microgrooves of rice leaf to merge two features, omniphobicity and anisotropic wetting property, on the desired surfaces. As previously reported, the UV-assisted micromolding process with a mixture of photoinitiator and acrylate functionalized prepolymer containing aluminum oxide nanoparticles (Al_2O_3) is a controllable, cheap and low-expertise route to mass production for fabricating a superhydrophobic hierarchical structure. We proposed three different cross-sectional shapes of the micro line arrays, which are prism, rectangle, and overhang structures, to evaluate the surfaces' directional sliding effect for water and oil. It was found that the surfaces with overhang structure line arrays have the allowable anisotropic oil sliding effect resulting from contact angles and roll-off angles (sliding angles) of mineral oil. Also, it was worthwhile noting that we successfully mimic the rice leaf, using dual roughness prism arrays pattern. Furthermore, we demonstrated that the directional non-wetting movement of photoresist (AZ 1512) on the fabricated surfaces and the line tracing of water and mineral oil, verifying wide application in several fields.

Finally, we showed a facile fabrication method to make robust and flexible PDMS films with lotus leaf-inspired dual-scale hierarchical pyramidal arrays for high efficiency of perovskite solar cells, by securing bifunctional roles of "anti-reflection" and "self-cleaning". Fabricated H.P. PDMS film by micromolding and

Ar ion surface treatment was easily attached to a bare FTO glass, which is the substrate of perovskite solar cell devices, without any additional adhesives. It turned out that the H.P. PDMS film has the anti-reflection property with structural advantages of the pyramid shapes, leading to an improvement in the J_{sc} and PCE of perovskite solar cells. Also, the film demonstrated excellent superhydrophobicity and self-cleaning behavior with long-term stability like the well-known lotus leaf. The experimental results revealed that this simple, yet durable anti-reflection and self-cleaning PDMS film would be useful in various energy applications in which transparent substrates require both light-harvesting and self-cleaning.

Key Words : Bio-inspired, Re-entrant structures, Mushroom-shape, Lotus effect, Superomniphobic, Directional sliding, Anisotropic wetting, Multi-scale structures, Self-cleaning, Anti-reflection, Perovskite solar cell

Student Number: 2010-20648

Contents

Abstract	i
List of tables	vii
List of figures	viii
Nomenclature	xiv
Chapter 1. Introduction	1
Chapter 2. Fabrication of Bioinspired Re-entrant/Overhang Structures for Multifunctional Surfaces	
2-1. Introduction	10
2-2. Over-etching method to prepare Gecko-inspired mushroom-like micropillars with re-entrant curvature	12
2-3. Experimental results and discussion of fabricated mushroom-like micropillar arrays	15
2-4. Fabrication of overhang line arrays using SU-8 photolithography with partial UV exposure	19
Chapter 3. Development of Robust Polymeric Superomniphobic Surfaces with Mushroom-like Micropillar Arrays	
3-1. Introduction	21
3-2. Experimental	24
3-3. Results and Discussion	27

3-3-1. Fabrication of gecko-inspired polymeric mushroom-like micropillar arrays	27
3-3-2. Measurement superomniphobic properties on the fabricated polymer surfaces for optimal design parameters	30
3-3-3. Effect of re-entrant curvature on superomniphobic surfaces ...	34
3-3-4. Additional test for various useful applications: (1) Transparency	38
3-3-5. Additional test for various useful applications: (2) Long term stability	41
3-4. Summary	43

Chapter 4. Directional Water/Oil Sliding Surfaces with Bio-inspired Hierarchical Anisotropic Groove Micro-structures

4-1. Introduction	45
4-2. Experimental	48
4-3. Results and Discussion	55
4-3-1. Morphologies of fabricated rice-leaf-inspired line arrays	55
4-3-2. Directional hydrophobicity on the fabricated surfaces	59
4-3-3. Directional oleophobicity on the fabricated surfaces	62
4-3-4. Theoretical analysis of directional oil sliding phenomenon ...	66
4-3-5. Additional experiments using directional sliding properties for practical applications	73
4-4. Summary	76

Chapter 5. Robust, Flexible Anti-Reflection and Self-Cleaning Surfaces with Hierarchical Pyramidal Arrays for Efficiency Enhancement of Perovskite Solar Cells

5-1. Introduction	77
5-2. Experimental	80
5-3. Results and Discussion	87
5-3-1. The structure of fabricated PDMS film and perovskite solar cell device	87
5-3-2. Anti-reflection effect of the fabricated H.P. PDMS film	90
5-3-3. Analysis of the optical property of H.P. PDMS film	92
5-3-4. Performances of perovskite solar cell device with H.P. PDMS film	99
5-3-5. Superhydrophobicity and Self-cleaning effect of the fabricated H.P. PDMS film	103
5-4. Summary	107
References	108
국문초록	119

List of Tables

- Table 5-1.** Short-circuit photocurrent density (J_{sc}), open-circuit voltage (V_{oc}), fill factor (FF), and power conversion efficiency (PCE) of the perovskite solar cells with and without the H.P. PDMS film. The data were collected under AM 1.5G one sun illumination (100 mW/cm^2).

List of Figures

- Figure 1-1.** Various examples of functional systems from nature. (a) Superhydrophobic from lotus leaf, (b) dry adhesives from gecko foot, (c) drag reduction from shark skin and (d) anti-reflection from moth-eye.
- Figure 1-2.** (a) Surface energy balance interaction of Young's equation model. (b-c) Schematic illustration of wetting behavior on the Wenzel and Cassie-Baxter state.
- Figure 2-1.** A schematic illustration for the fabrication procedure of PDMS and PFPE mushroom-like micropillar arrays.
- Figure 2-2.** (a) A schematic illustration for the detailed MEMS over-etching process and (b) footing effect at the etch-stop layer (SiO_2 layer) with SOI wafer. (c) Representative SEM images of fabricated mushroom-like micropillar using footing effect.
- Figure 2-3.** Tip size variation with increasing over-etching time. The red squared SEM images (e-f) are selected mushroom-like re-entrant structure in this work.
- Figure 2-4.** Schematic illustration of partial UV exposure method. Negative photoresist (SU-8) is spin-coated on the silicon wafer (a), and then partial UV exposure is conducted by utilizing the refractive index gap between air and SU-8 layer (b-c). (d) The final overhang structure after developing SU-8 on the substrate. (e) PDMS replication from SU-8 mold.
- Figure 3-1.** Surface modification results by C_4F_8 treatment. No significant differences were observed between non- C_4F_8 treatment PDMS surface (a-c) and the same surface with C_4F_8 treatment (d-f). As shown, the deposited layer of fluorocarbon compounds was thin (~ 50 nm) and uniformly coated.
- Figure 3-2.** The SEM images show that the two structures have the identical geometry after dual duplication processes. SEM images of the fabricated PDMS (a-c) and PFPE micropillars

(d-f) with side (upper panels) and top views (lower panels), respectively. The micropillars have 5 μm pillar diameter, 8.5 μm top disk diameter, 10 μm height with different SRs: SR = 1 for (a), (d), 6 for (b), (e), and 10 for (c), (f).

Figure 3-3. Static CAs and CAH graphs of DI water (a) and ethanol (c) on the PDMS micropillar arrays as a function of SR. Inset images are representative CAs at specific SR.

Figure 3-4. Static CAs and CAH graphs of DI water (a) and ethanol (c) on the PFPE micropillar arrays as a function of SR. Inset images are representative CAs at specific SR.

Figure 3-5. Schematic illustrations for the competition between Laplace (P_c) and internal pressures (P_i) of a droplet on truncated pyramids ($W_t < W_b$) (a), overhang structures ($W_t > W_b$) (b), and mushroom-like structures (c). As shown, the mushroom-like shape can be viewed as an extreme case of overhang structures. The arrows denoted relative magnitude and direction of each pressure.

Figure 3-6. Change of static CAs with two types of PDMS micropillar arrays as a function of SR: Red line represents mushroom-like micropillar arrays with ethanol for SR < 8, showing superomniphobic properties (see Figure 3-3(b)). Blue line is for regular micropillar arrays having 5 μm pillar diameter and 10 μm height. The inset photograph shows the wetting shape of ethanol on the surface.

Figure 3-7. (a) Transmittance spectra of various samples over UV-VIS wavelength regime. (b) Photographs of the PDMS and PFPE samples (bare and structured) on a text paper. No significant difference was observed from both samples.

Figure 3-8. Demonstration of superomniphobic surfaces on touch-phone screens. The left figure shows that the superoleophobic surface (PDMS micropillar arrays, SR = 6) is not contaminated by various liquids: DI water (transparent), mineral oil (blue), hexadecane (red) and ethanol (yellow). In contrast, the unmodified surface on the right is immediately wetted by the liquids upon contact.

- Figure 3-9.** (a-b) Measurement of static CAs of the PDMS (a) and PFPE (b) samples (SR = 6) over a time period of 6 months. Inset photographs show the CAs of various liquids: DI water (transparent), mineral oil (blue), hexadecane (red) and ethanol (yellow) at different time points.
- Figure 4-1.** (a-b) SEM images for rice leaf surface at two different magnifications. (c-d) Photographs of water (red) and mineral oil (transparent) droplets (volume of 5 μ l) placed on the rice leaf surface.
- Figure 4-2.** Fabrication scheme of anisotropic line arrays with dual-scale hierarchical roughness.
- Figure 4-3.** Fabrication scheme of dual-scale prism (a) and rectangle (b) line arrays. The dimensions of the three line arrays were chosen in such a way that length scales are similar except for the cross-sectional profile.
- Figure 4-4.** (a-c) SEM images of prism, rectangle and overhang groove microstructures where each magnified view is shown in (d-f). The arrows indicate the parallel and perpendicular directions with respect to the direction of microgrooves. The inset clearly shows the presence of a nanoroughness with 40 nm- Al_2O_3 nanoparticles after UVO treatment.
- Figure 4-5.** SEM images of micro-only line arrays with rectangle (a) and overhang (b) shapes. (c-d) Magnified SEM images of the fabricated micro line arrays where the inset shows smooth surface without nanoroughness.
- Figure 4-6.** These SEM images indicate that the fabrication can be conducted over large areas with high physical integrity and pattern fidelity.
- Figure 4-7.** Advancing and receding CAs (a) and SAs (b) of DI water on the fabricated surfaces (flat, prism, rectangle and overhang structures, respectively) along the parallel and perpendicular directions. The SA of 90° means that the droplet would not slide on the surface with any tilting angle of substrate.

- Figure 4-8.** CA images of DI water and mineral oil on the various microgroove structures in the parallel and perpendicular directions.
- Figure 4-9.** Advancing and receding CAs (a) and SAs (b) of mineral oil on the fabricated surfaces (flat, prism, rectangle and overhang structures, respectively) along the parallel and perpendicular directions (see the inset image).
- Figure 4-10.** Optical microscope (OM) images showing the existence of air pocket between a mineral oil and an underlying overhang structure (see the zoomed areas). In the case of prism and rectangle structures, the grooves were wetted by the oil. In particular, the overhang structures were not wetted before and even after an external perturbation such as inclining, which means that the surface is stable with the Cassie state.
- Figure 4-11.** (a) Schematic illustration for the competition between internal (P_i) and Laplace (P_c) pressures of an oil droplet on the prism (i), rectangle (ii), and overhang structures (iii). The arrows indicate the direction and relative magnitude of each pressure. The edge angle α is determined by the cross-sectional shape of microgrooves. (b) Schematic illustration of critical contact angle at the edge in the perpendicular direction for DI water (i) and mineral oil (ii).
- Figure 4-12.** (a) Geometric description of overhang structures. Liquid-solid-air interface with DI water (b) and mineral oil (c) on the fabricated overhang structures.
- Figure 4-13.** Anisotropic factors (AFs) on the fabricated surfaces with DI water and mineral oil where the characters M and H represent micro only and hierarchical structures, respectively. The rice leaf has a low AF of 0.052 and that of lotus leaf is almost zero.
- Figure 4-14.** (a) Surface sliding of photoresist (AZ 1512) on (i) rice leaf-like prism arrays and (ii) overhang line arrays. (b) Curved line tracing of mineral oil on the S-shaped overhang structure. The arrows indicate the direction of oil sliding. (c) Droplet images of DI water (blue, red, and yellow) and mineral oil (transparent) on the horizontal and inclined surfaces (tilting

angle = 60°). (d) Anisotropic liquid sliding railroad where each DI water droplet (red and yellow) smoothly slides along the path without any collision or mixing.

- Figure 5-1.** Fabrication scheme of dual-scale hierarchical pyramid (H.P.) PDMS arrays and perovskite solar cell device with the H.P. PDMS film on the glass-side.
- Figure 5-2.** (a-c) SEM images of micro pyramidal arrays before Ar ion treatment.
- Figure 5-3.** (a-c) SEM images for H.P. structures with different magnifications and view angles. The inset clearly shows the nano-wrinkled roughness on the fabricated micro pyramid arrays after Ar ion treatment. There are no significant structural different between micro pyramidal arrays and H.P. structures (see Figure 5-2), but roughness of pyramid surface as shown in inset image of (c).
- Figure 5-4.** (a) Schematic illustration for structure of perovskite solar cell and (b) focused ion beam assisted cross-sectional SEM image of the perovskite solar cell with two-step deposition process. mp-TiO₂ and bl-TiO₂ represent mesoporous TiO₂ and blocking layer TiO₂, respectively. (c) The photograph and schematics of fabricated perovskite solar cells device with multi-functional H.P. PDMS film.
- Figure 5-5.** Transmittance (a) and reflectance spectra (b) of FTO glass with three different cases, bare FTO, flat PDMS and H.P. PDMS. The inset photographs represent the fabricated flexible H.P. PDMS film attached on a FTO glass showing visual effect of anti-reflection.
- Figure 5-6.** Self-cleaning and optical properties of two different micro structures. Superomniphobicity and low optical advantages of mushroom-like micropillar arrays. Superhydrophobicity and structural anti-reflection effect of H.P. PDMS film.
- Figure 5-7.** (a) SEM images of the H.P. arrays with 45° angle of bottom edge side. The H.P. PDMS film serves as anti-reflection layer on the perovskite solar cell device. (b) Theoretical scheme of

anti-reflection mechanism on the H.P. PDMS film. The size and color of arrows indicate relative magnitude and direction of each light. (c-d) Refractive index profiles of the bare FTO glass and the FTO glass with a flat PDMS layer.

Figure 5-8. The path of the incident light (green) with reflection (red) and transmission (blue) between air and pyramid PDMS surfaces. The length and width of arrows roughly indicate the direction and intensity of each path way. Parentheses represent refractive indices.

Figure 5-9. (a) Current density-voltage curves and (b) EQE of perovskite solar cell devices with and without (bare FTO) the H.P. PDMS film.

Figure 5-10. (a) Static CAs (green line) and ROAs (blue line) of de-ionized (DI) water on the three different surfaces. Microscope images of a droplet on the each surface are shown in the insets. (b) Time-dependent CA and ROA of the H.P. PDMS film measured over a time period of one month. Inset photograph shows the degree of reflectivity and superhydrophobicity for the different areas with and without a H.P. PDMS film on the same perovskite solar cell. Water was coloured with red dye to demonstrate visually.

Figure 5-11. (a) Schematic illustration of self-cleaning effect on the H.P. PDMS surface. (b) Self-cleaning experiments for the perovskite solar cell devices without (i) and with (ii) the H.P. PDMS film.

Nomenclature

γ_{lv}	Interfacial tension at the liquid/vapor interface
λ	Wavelength
γ	Surface tension
θ	Contact angle
f	solid fraction at the liquid-solid-air interface
L	Perimeter of structure
A	Cross sectional area
V	Volume of a liquid droplet
ρ	Density of liquid
g	Gravitational constant
$R(\theta)$	Radius of liquid droplet
α	Edge angle subtended by the microstructures
//	Parallel direction
\perp	Perpendicular direction
n	Refractive index
R	Fresnel's reflectance coefficient
r	Ratio of the reflective/incident light amplitude

Chapter 1. Introduction

Nature has developed various functional systems of its own, which have hierarchical structures with a wide range of dimensions from the the nanoscale size to the macroscale one. [1-5] Biomimetics mimicking nature are the promising technology to realize desirable properties on human life. There are many creatures in nature with interesting functions such as gecko foot, lotus leaf, rice leaf, moth eye, butterfly wings and shark skin as shown in Figure 1-1. [6-9] These objects have specific materials, structures and process so as to provide certain properties which are dry or wet adhesions, superhydrophobicity, self-cleaning, drag reduction, structural coloration, anti-reflection and self-healing, etc.

Most of all, research for controlling surface wetting property, which may be inspired from nature such as plant leaves or insect legs/wings, have been recently carried out with considerable attention from various scientific area. [2, 10] The extensive efforts to control the water repellent property have been made over the past decade. A lot of fabrication methods, including photolithography, micromolding and surface wrinkling have been employed to create the bio-inspired superhydrophobic surfaces. Also, water on the surfaces tends to move along parallel direction with texture because of the energy barrier principles which cause sliding angle difference with perpendicular direction. It is well established

that the anisotropic wetting properties can be controlled by introducing texture modification and chemical treatment on surfaces according to the Wenzel and Cassie-Baxter models. Figure 1-2 shows schematic illustration of the Wenzel and Cassie-Baxter state, which are derived from Young's equilibrium equation. [11, 12] In contrast to fully wetted phenomenon by water in Wenzel state, Cassie-Baxter state repellent water with air pocket underneath the droplet. More detailed, the Young's equation which gives,

$$\cos \theta = \frac{\gamma_{sv} - \gamma_{sl}}{\gamma_{lv}}$$

may be used to design appropriate parameters for robust composite interface. A liquid droplet forms either in the state of Wenzel or Cassie model according to shape of microstructures and surface energy of the structures. Based on the previous works, Cassie state propose a heterogeneous composite surface composed of liquid, solid and air , which gives,

$$\cos \theta_c = f \cos \theta_{liquid} + (1 - f) \cos \theta_{air} = f(\cos \theta_{liquid} + 1) - 1$$

where θ_c is the apparent contact angle on a Cassie state surface, θ_{liquid} is equilibrium contact angle of liquid on a flat surface and f is the area fraction factor of each material. In this Cassie state equation, area fraction factor f can be described as,

$$f = \frac{\text{wetted area}}{\text{normal area}} = \frac{\pi^2}{4(d+s)^2}$$

where d is the diameter, s is space between the structures and t is the tip diameter of micro-pillar structures (Figure 1-2(c)). From the relationship of area fraction factor f and Cassie state equation, to obtain high apparent contact angle of liquid on a surface, the value of f need to be low. Continually, the value of area fraction factor between liquid and surface may be decrease with increasing spacing ratio (s/d).

In the same manner, research on controllable oil sliding surfaces has been triggered. Since the discovery of superoleophobic surfaces by Cohen and coworkers,[13, 14] the omniphobic surfaces, which repel various liquids with a wide range of surface tensions, have been developed with several significant results. Inhibiting liquids with low surface tensions fully wetting on the surfaces, negative slope structures such as overhang and re-entrant shapes, which are inverse shape of truncated pyramid structures, have been suggested to resist the energetically favorable Wenzel state. As such, omniphobic surfaces demonstrate the non-wetting property with a high contact angle (CA) ($> \sim 150^\circ$) and a low contact angle hysteresis (CAS, difference between advancing and receding contact angles) ($< \sim 10^\circ$) for low surface tension liquids due to the fact that the surfaces consist of re-entrant texture randomly or uniformly fabricated with beads or pillars. From a wide variety of areas such as microfluidic channels, mobile market,

oil transportation and semiconductor industry, superomniphobic surfaces are needed, to transport or collect remaining oil efficiently and to prevent contamination from the oil. In particular, developed and combined surfaces having the self-cleaning effect of the superomniphobic surfaces and anti-reflection property are very useful for the performance of solar cell devices.

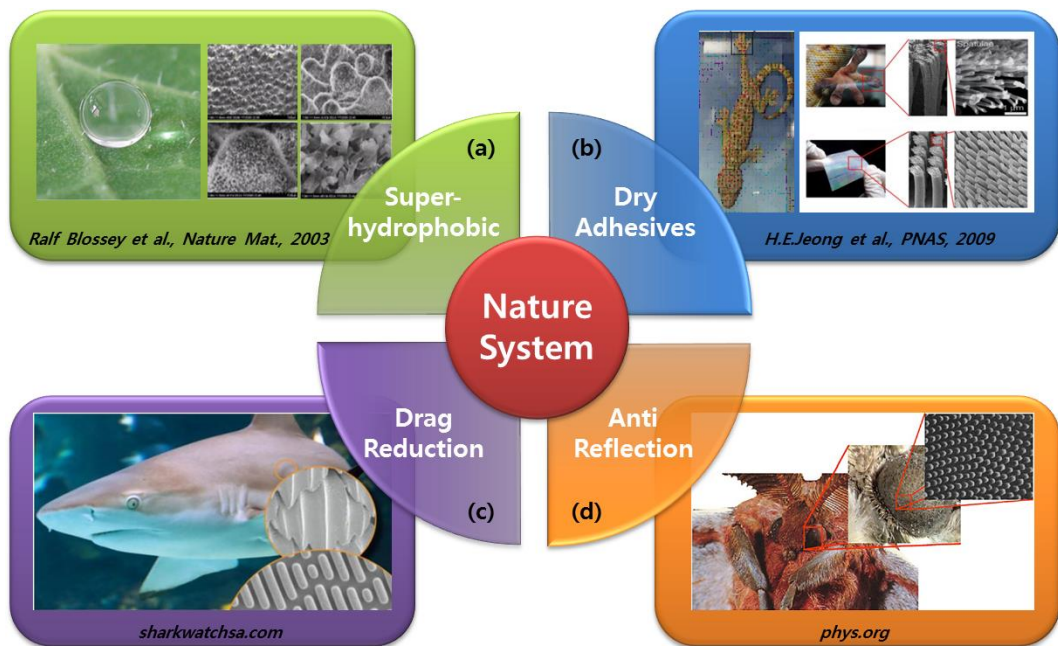


Figure 1-1. Various examples of functional systems from nature. (a) Superhydrophobic from lotus leaf, (b) dry adhesives from gecko foot, (c) drag reduction from shark skin and (d) anti-reflection from moth eye.

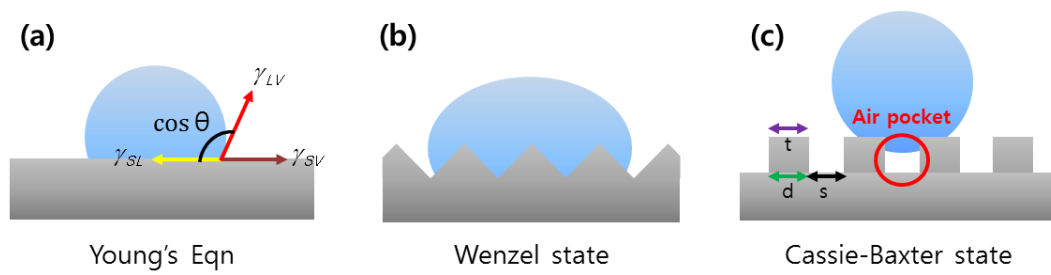


Figure 1-2. (a) Surface energy balance interaction of Young's equation model. (b-c) Schematic illustration of wetting behavior on the Wenzel and Cassie-Baxter state.

In this thesis, we presented the multiscale fabrication approaches of nature-inspired superomniphobic surfaces for multifunctional applications such as structural design for water and oil repellent surfaces, directional liquid sliding surfaces, enhancing photovoltaics performances using self-cleaning and anti-reflection properties.

In *Chapter 2*, we introduced bioinspired polymeric re-entrant (overhang) structures by using low-expertise yet robust over-etching fabrication process and SU-8 photolithography with partial UV exposure. The structure of gecko foot in nature has been used for various applications particularly in dry adhesive researches. However, we had interests in the end tips of a gecko foot which have similar shape with the re-entrant structures. Using the conventional deep reactive ion etching process with silicon on insulator (SOI) wafer, we could make wide-tip microstructures through the over-etching step at the etch-stop layer (SiO_2), and then replicate the structure on flexible and transparent polymer surfaces. Also, inspired from rice leaf morphology, overhang line arrays were fabricated by partial UV exposure method using SU-8 negative photoresist.

In *Chapter 3*, we demonstrate superomniphobic properties of fabricated polymer surfaces. Such re-entrant structures were found to be highly resistant against wetting of various liquids and oils with a wide range of surface tensions

(γ_{lv}) from 22.3 (ethanol) to 72.1 mN/m (water) by measuring the static contact angle and contact angle hysteresis. Additionally, transmittance and aging effect were investigated for greater applicability.

In *Chapter 4*, we presented overhang micro line arrays inspired from microgrooves of rice leaf to merge two features, omniphobicity and anisotropic wetting property, on the desired surfaces. As previously reported, the UV-assisted micromolding process with a mixture of photoinitiator and acrylate functionalized prepolymer containing aluminum oxide nanoparticles (Al_2O_3) is a controllable, cheap and low-expertise route to mass production for fabricating a superhydrophobic hierarchical structure. We proposed three different cross-sectional shapes of the micro line arrays, which are prism, rectangle, and overhang structures, to evaluate the surfaces' directional sliding effect for water and oil. It was found that the surfaces with overhang structure line arrays have the allowable anisotropic oil sliding effect, resulting from contact angles and roll-off angles (sliding angles) of mineral oil. Also, it was worthwhile noting that we successfully mimic the rice leaf, using dual roughness prism arrays pattern. Furthermore, we demonstrated the directional non-wetting movement of photoresist (AZ 1512) on the fabricated surfaces and the line tracing of water and mineral oil, verifying effective application in several fields.

In *Chapter 5*, we further developed a facile fabrication method to make robust and flexible PDMS films with lotus leaf-inspired dual-scale hierarchical pyramidal arrays for high efficiency of perovskite solar cells, by means of securing bifunctional roles of “anti-reflection“ and “self-cleaning“. Fabricated H.P. PDMS film by micromolding and Ar ion surface treatment was easily attached to a bare FTO glass, which is the substrate of perovskite solar cell devices, without any additional adhesives. It turned out that the H.P. PDMS film has the anti-reflection property with structural advantages of the pyramid shapes, leading to an improvement in the J_{sc} and PCE of perovskite solar cells. Also, the film demonstrated excellent superhydrophobicity and self-cleaning behavior with long-term stability like the well-known lotus leaf. The experimental results revealed that this simple, yet durable anti-reflection and self-cleaning PDMS film would be useful in various energy applications in which transparent substrates require both light-harvesting and self-cleaning.

Chapter 2. Fabrication of Bioinspired Re-entrant/ Overhang Structures for Multifunctional Surfaces

2-1. Introduction

Recently, a number of fabrication methods have been used to make multiscale and multifunctional structures on a desired polymeric substrate. For examples, conventional MEMS etch process and photolithography are used to fabricate semi-conductor silicon master, soft and micro/nanoimprint lithography are performed to make hierarchical polymer structures, also capillary force lithography are developed to produce uniform and controllable multiscale structures. [15-18] Although these methods for polymeric structures are useful, it is difficult to fabricate superomniphobic surfaces with various applicable properties. To demonstrate superomniphobicity, many research groups have suggested re-entrant structures (or overhang structures) in recent works. [13, 14] Nevertheless, due to the re-entrant structured surfaces have been almost fabricated by using chemically treated rigid and inorganic materials such as glass based substrate or silicon dioxides, those surfaces have been easily contaminated upon multiple usages and usually involved a complicate and high-cost process.

Herein we describe smart, robust and facile method to fabricate bioinspired re-

entrant/overhang structures for superomniphobic surfaces with multifunctional properties. From nature, structure of gecko-foot-shape has been used for various applications particularly in dry adhesive researches. [5, 9] However, we have an inspired from the existence of end tips of gecko-foot which have similar shape with the re-entrant structures. Using conventional deep reactive ion etching process with silicon on insulator (SOI) wafer, we could make a wide tip microstructure owing to over-etching step at the etch-stop layer (SiO_2), then replicate the structure on flexible and transparent polymer surfaces. Also, using partial UV exposure method with SU-8 negative photoresist, re-entrant line structure arrays could be tuned by controlling exposure time.

2-2. Over-etching method to prepare Gecko-inspired mushroom-like micropillars with re-entrant curvature

A schematic flow of the fabrication process is shown in Figure 2-1. The 4-inch silicon on insulator (SOI) wafer was purchased from Mico MST Co. (Korea) The wafer consists of three layers: a p-type (100) bare silicon wafer (resistivity: 1~30 Ω), a SiO₂ etch-stop layer of 500-nm-thickness, and a polysilicon layer of 10- μ m-thickness. First, using tetraethoxysilane (TEOS), an 800-nm-thick SiO₂ layer was deposited on the SOI wafer by the plasma-enhanced chemical vapor deposition process. Then, hole patterns of 5- μ m-diameter and 10- μ m-height with 10 different spacing ratios (SR = space/diameter) were formed by the conventional photolithography using AZ1512 photoresist (PR). Subsequently, pattern transfer to the SiO₂ layer was carried out using the PR etch mask, which was followed by removal of the PR. Then, the polysilicon layer (the upper gray area of SOI wafer in Figure 2-1) was anisotropically etched via SF₆ and Ar gas plasma until the exposure of the SiO₂ etch-stop layer (the lower yellow area of SOI wafer in Figure 2-1) in an inductively coupled plasma (ICP) chamber with 13.56-MHz radio-frequency power generators. The same etching was performed further utilizing an extremely high etch selectivity between polysilicon and SiO₂ etch-stop layer in order to over-etch the polysilicon layer to the lateral direction. [9]

To fabricate robust polymeric superomniphobic surfaces, a mixture of 10:1

polydimethylsiloxane (PDMS) pre-polymer (Sylgard 184 Silicon elastomer, Dow Corning, USA) and curing agent was poured on the patterned SOI wafer and placed in an oven at 70 °C for 1 h. Then, the PDMS replica was peeled off from the SOI wafer (1st replica). [19] The UV-curable polyurethane acrylate (PUA) precursor was drop-dispensed on the PDMS 1st replica and gently covered by a 50 µm PET film, which was followed by UV ($\lambda = 250$ to ~ 400 nm) exposure for a few tens of seconds. After obtaining the PUA replica, the 2nd perfluoropolyether (PFPE) replica (PFPE precursor, Solvay Co. LTD, USA) was replicated using the same process after overnight curing of the PUA replica (> 12 h). This step was a prerequisite to ensure a sufficiently inert, non-reactive PUA surface with clean release of the 2nd PFPE replica. The resulting PDMS and PFPE replicas had mushroom-like micropillar arrays with re-entrant profiles (see Figure 2-1).

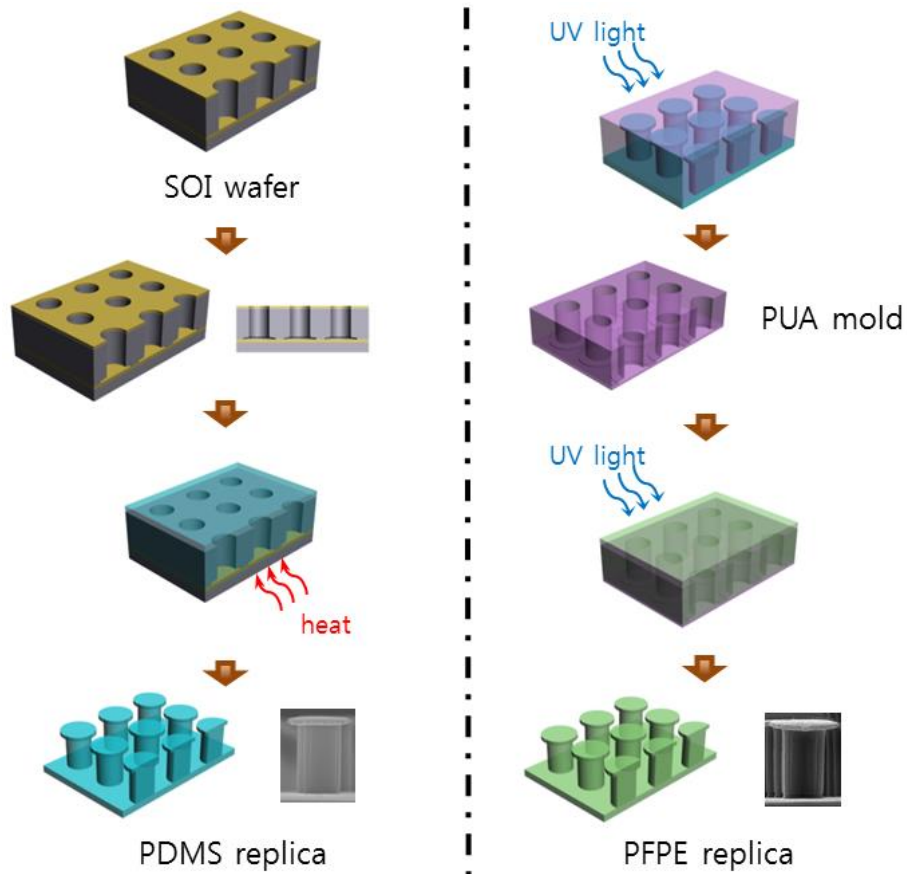


Figure 2-1. A schematic illustration for the fabrication procedure of PDMS and PFPE mushroom-like micropillar arrays.

2-3. Experimental results and discussion of fabricated mushroom-like micropillar arrays

A detailed schematic flow of the advanced MEMS fabrication method using over-etching process is shown in Figure 2-2(a). Conventional MEMS dry etching system has methodological advantages that it could perform anisotropic, directional etching with high resolution and cleanliness. Such MEMS dry etching processes are consist of main three parts, which called BOSCH process. First, silicon etch using SF_6 and Ar gas and deposit passivation layer with polymer gas (C_4F_8 gas), finally bottom side polymer etch and repeat the cycle with 1st step again. Performing these repetitive dry etch process with silicon wafer containing etch-stop layer (SiO_2), the SF_6 and Ar gas plasma etch the silicon layer to the lateral direction upon facing silicon oxide (SiO_2) layer. Sequentially, it could be footing effect due to the different etch selectivity between silicon and SiO_2 etch-stop layer as shown in Figure 2-2(b). Using SiO_2 etch-stop layer of SOI wafer, we could carry out over-etching process and obtain flat bottom area which mimics gecko foot and has mushroom-like re-entrant curvature characteristic at the etch-stop layer (see Figure 2-2(c)). This wide and flat tip is a key structure of this experiment and its size can be controlled by modulating etching time as shown in Figure 2-3. The tip size of mushroom-like micropillar becomes wider with increasing over-etching time. However, it could be stuck by PDMS polymer in

replicating process because of too large flat bottom area of SOI wafer due to the excessive over-etch time (see Figure 2-3(g-h)). It is envisioned that this low-expertise yet robust fabrication route could present wide insight to the bioinspired omniphobic system.

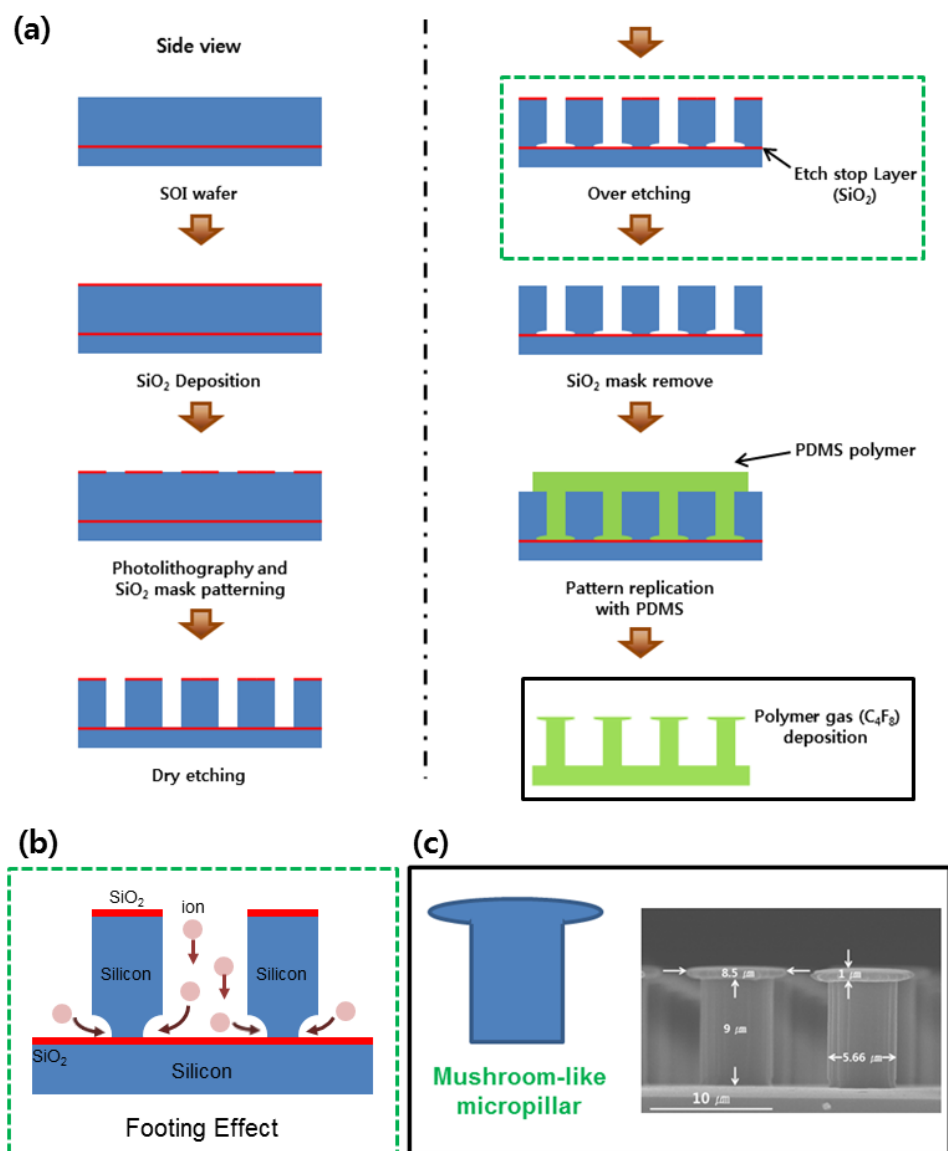


Figure 2-2. (a) A schematic illustration for the detailed MEMS over-etching process and (b) footing effect at the etch-stop layer (SiO₂ layer) with SOI wafer. (c) Representative SEM images of fabricated mushroom-like micropillar using footing effect.

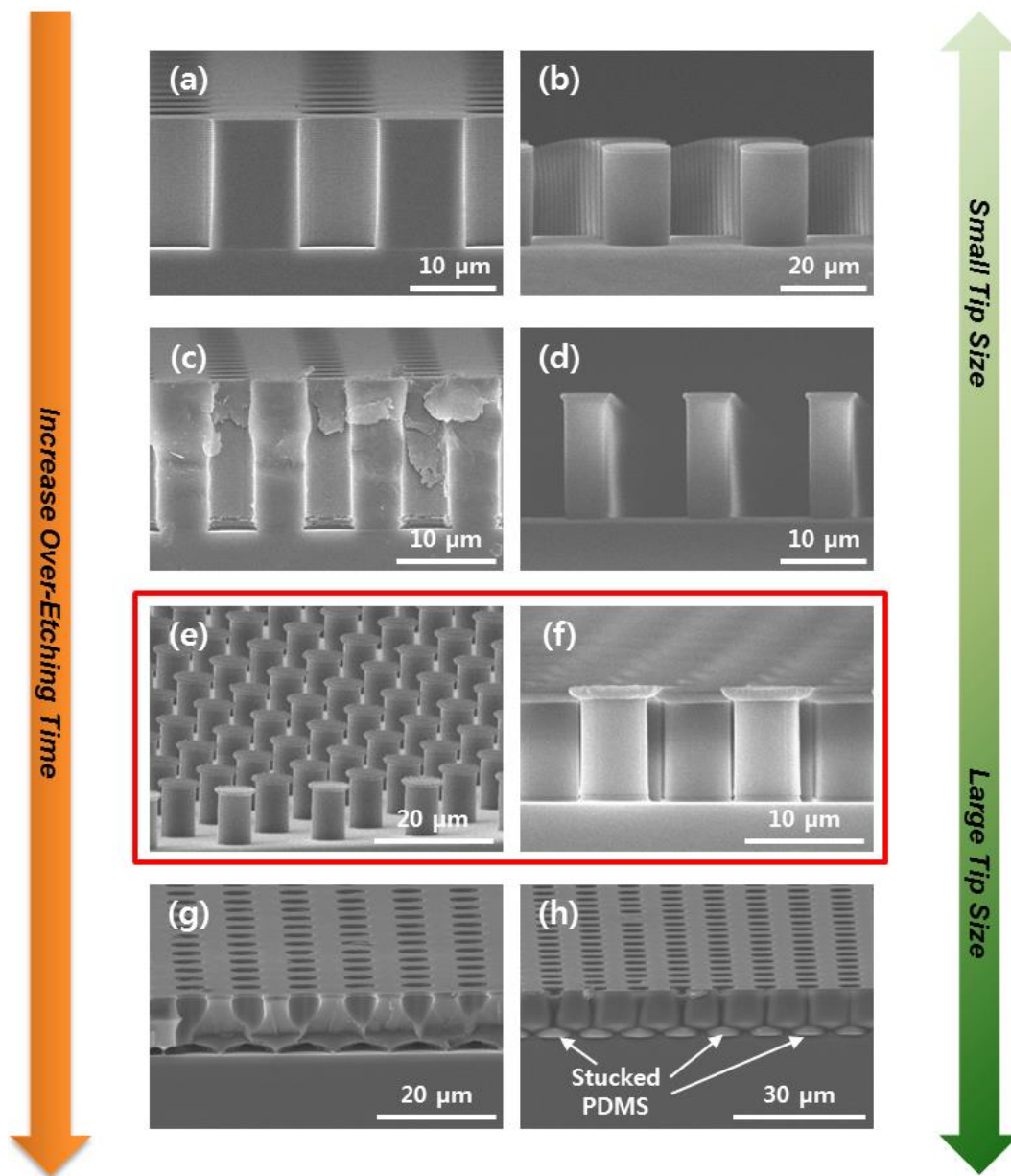


Figure 2-3. Tip size variation with increasing over-etching time. The red squared SEM images (e-f) are selected mushroom-like re-entrant structure in this work.

2-4. Fabrication of overhang line arrays using SU-8 photolithography with partial UV exposure

After cleaning 4-inch silicon wafer using ethanol and isopropyl-alcohol, a 20- μm -thick negative photoresist (SU-8, Micro Chem Co., USA) was deposited by spin coating (1500 rpm, 30 s) on the wafer. Then, overhang line arrays with a patterned field of 20 mm \times 20 mm were formed by conventional photolithography using the partial exposure method, as shown in Figure 2-4. As the thickness of SU-8 is relatively high, the bottom area of SU-8 layer would be partially cured in the case of an insufficient exposure time aided by the difference of UV-light refractive index between air and SU-8 layer. As a result, the shapes of microstructure can be tuned by controlling the exposure time. In particular, an overhang structure with a 20- μm -thick SU-8 layer was obtained by decreasing the exposure time to 8 s with an intensity of 15 mJ/cm^2 as compared to the normal exposure time of 10 s under the same intensity to obtain the vertical profile (see Figure 2-4(c-d)). The replicated PDMS mold contained equally-spaced inverse trapezoidals with 20 μm bottom and 30 μm top widths of 20 μm depth. Such an overhang line array would be used throughout the experiment along with the prism and rectangular line arrays.

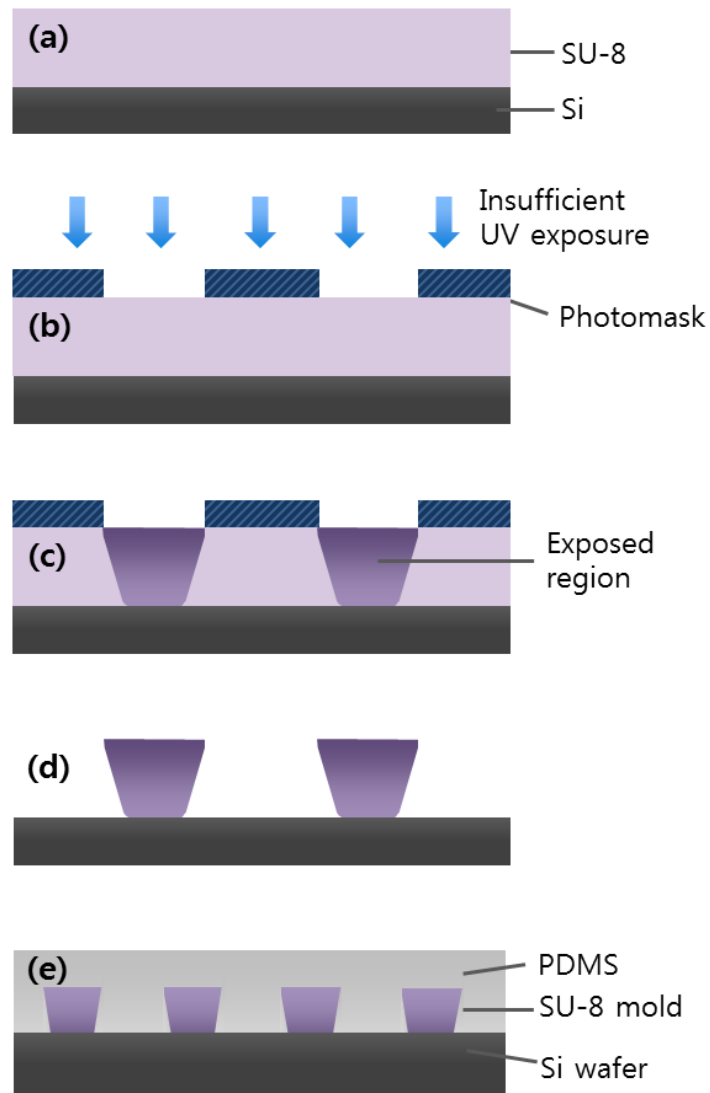


Figure 2-4. Schematic illustration of partial UV exposure method. Negative photoresist (SU-8) is spin-coated on the silicon wafer (a), and then partial UV exposure is conducted by utilizing the refractive index gap between air and SU-8 layer (b-c). (d) The final overhang structure after developing SU-8 on the substrate. (e) PDMS replication from SU-8 mold.

Chapter 3. Development of Robust Polymeric Super- omniphobic Surfaces with Mushroom-like Micropillar Arrays

Published in Soft Matter, 2012, 8, 8563-8568

3-1. Introduction

Research for superhydrophobic surfaces, which may be defined as surfaces with a high contact angle (CA) ($> \sim 150^\circ$) and a low contact angle hysteresis (CAH) ($< \sim 10^\circ$), has become mature in terms of fundamental understanding and fabrication skills. Extensive efforts have been made for the last few decades to develop fabrication techniques for superhydrophobic surfaces based on various top-down and bottom-up approaches. [10, 20-23] It is now well understood that the wetting state can be accurately described by the Wenzel and Cassie-Baxter models for fully and partially wetted surfaces. The key contributions from surface modification (chemical) and surface texture (physical) are also well described by the two models. [24, 25]

Since the discovery of Cohen and coworkers for oleophobic and superoleophobic surfaces,[13, 14, 26, 27] the oil-repellent surfaces are also gaining interest from the academia as well as from the industry. Practically, these

non-sticky surfaces to oils and inks are important in various applications such as inkjet printing,[28] xerography,[29] home appliances,[30] etc. In general, oils have relatively low surface tension and smaller CA than water, which causes a significant hurdle to superoleophobic surfaces; most surfaces would be oleophilic according to the Wenzel's model. [31, 32] To address this challenge, researchers have introduced several unusual surfaces such as reentrant, negative-slope structures, to make the surface "metastable" in the Cassie-Baxter regime. [11, 12] Obviously, in such a metastable state, it would be difficult to develop a robust, superoleophobic surface that can resist the energetically favorable Wenzel state. [33, 34] To achieve both mechanically robust and energetically favorable omniphobic surfaces, it is of paramount importance to form a unique, re-entrant profile of microstructures. Microstructures of a simple negative slope (e.g., overhanging shapes such as inverse-trapezoidal microstructures[30]) are also helpful, but it was reported that a permanent Cassie-Baxter state cannot be ensured for such structures. Although dual scale (typically micro/nano) structures, when combined with a suitable fluorocarbon surface treatment, also turned out to be useful for oleophobic surfaces, [35-37] a genuine superoleophobic surface has not been demonstrated to date using this approach.

In the re-entrant surface structures, a central idea is that the meniscus of a liquid droplet has a convex curvature, thus getting pinned to the entrance part of the microstructure. Then, the meniscus exerts a net force upward, competing with

the collapse of the droplet by the internal pressure (i.e., gravity) to a certain extent even for liquids with low surface tension. Accordingly, recent approaches have employed chemically treated rigid or inorganic materials such as glass and silicon oxides to make re-entrant, oil-repellent structures. [14, 30, 37] The widespread use of the methods has been limited in that they are prone to surface contamination upon multiple usages and involve complicated and high-cost processes.

To solve some of these limitations, in this chapter, we presented polymeric superomniphobic surfaces by utilizing simple micromolding and fluorocarbon surface treatment. The micromolding approach is an intrinsically cheap, low-expertise route to mass production; polymer replicas are generated without limitation from the same master pattern. We proposed that mushroom-like micropillars, which have been proven effective for smart dry adhesive surfaces inspired from gecko toe pad, [31, 38-40] also represent efficient re-entrant profiles, thus allowing superomniphobic surfaces for a wide range of liquids with different surface tension. To evaluate superomniphobic properties, we measured static CA and CAH of various liquids, ranging from water ($\gamma_{lv} = 72.1$ mN/m) to ethanol ($\gamma_{lv} = 22.3$ mN/m). Furthermore, the fabricated surfaces were transparent in the visible spectrum and durable for a long period of time up to 6 months as evidenced by the UV-VIS transmittance measurement and aging experiment.

3-2. Experimental

3-2-1. Fluorocarbon surface treatment

To make the surface even more omniphobic, a fluorocarbon source of octafluorocyclobutane (C_4F_8) was treated on the fabricated surface of micropillars in *Chapter 2* by chemical plasma deposition with an ICP etching chamber. [41] The C_4F_8 gas is frequently adopted in the famous BOSCH process in deep reactive ion etch (DRIE) system. The samples were exposed to the gas steam under the conditions of 2000 W power, 10 W bias power, 25 mTorr and C_4F_8 150 sccm gas flow for 8 sec. It is known that a thin polymeric film of ~50 nm forms as a result of this surface treatment. [42] In our experiment, the use of C_4F_8 gas polymerization offers better reproducibility and robustness compared with previous surface treatment methods. Also, as shown in Figure 3-1, it was found that the modification is uniform and does not significantly influence the as-prepared polymer structures.

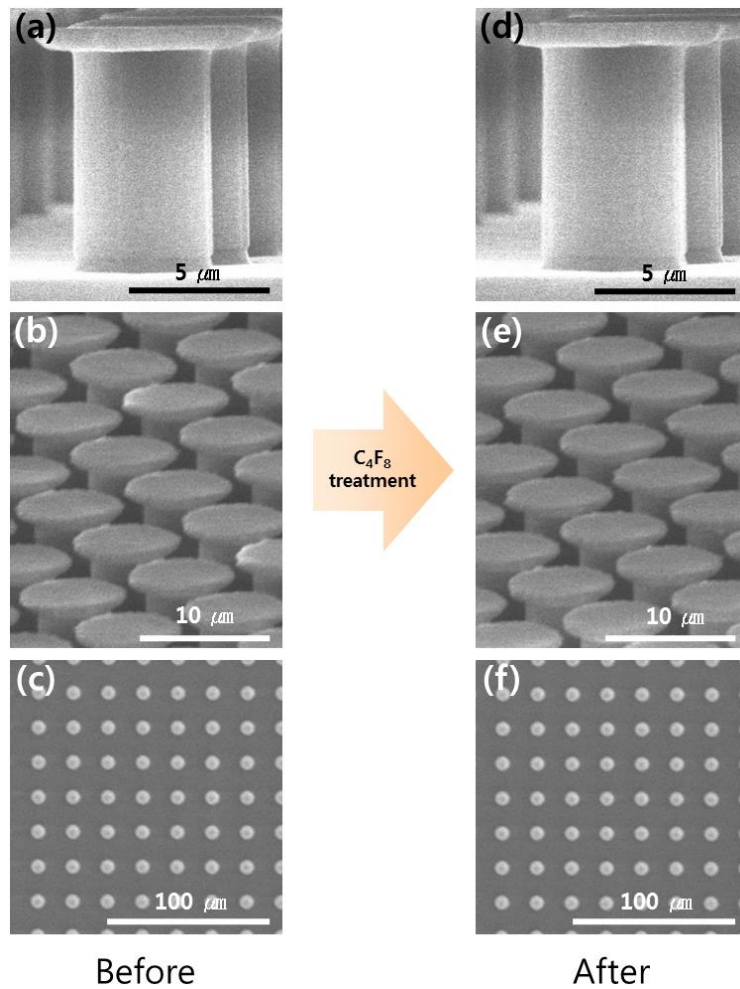


Figure 3-1. Surface modification results by C₄F₈ treatment. No significant differences were observed between non-C₄F₈ treatment PDMS surface (a-c) and the same surface with C₄F₈ treatment (d-f). As shown, the deposited layer of fluorocarbon compounds was thin (~50 nm) and uniformly coated.

3-2-2. Measurement of CA and CAH

The static CAs of various liquids was measured by using a contact angle analyzer (Drop Shape Analysis System DSA100, Kruss, Germany). Drops of 5 ~ 10 μl of each liquid were gently placed on the micro-structured surface and the CAH was calculated by taking time-period pictures.

3-2-3. Analysis of transmittance

UV/VIS transmittance spectra taken from PerkinElmer Lambda 45 UV/VIS spectrometer were used to analyze the transmittance of fabricated PDMS and PFPE samples in the range of visible light wavelength of 190 ~ 800 nm.

3-2-4. Scanning electron microscopy (SEM)

A 20-nm-thick platinum (Pt) layer was deposited on the micro-structured surface to avoid charging effects. High-resolution SEM images of the micropillars were obtained by using a HITACHI S-48000 scanning electron microscope (Hitachi, Japan).

3-3. Results and Discussion

3-3-1. Fabrication of gecko-inspired polymeric mushroom-like micropillar arrays

Figure 3-2(a-f) shows representative SEM images of PDMS and PFPE micropillar arrays replicated from the SOI master pattern (5 μm diameter, 10 μm height with SR of 1 ~ 10). As shown in the figure, the PDMS and PFPE microstructures exhibited high structural fidelity with well-defined vertical edge profiles. No structural differences were observed between the PDMS and PFPE microstructures. Furthermore, the same microstructures could be produced without structural defects or degradations (~ 20 times) over a large area. For generating uniform microstructured surfaces, care should be taken during the 2nd replication step so as to preserve on original height of the PDMS replica. To expel trapped air in the replication, a roller was mildly rounded several times on top of a flat polyethylene terephthalate (PET) film that was used as a supporting substrate (see experimental section). Also, the curing time needs to be controlled for maintaining the PFPE surface inactive to the PUA material, recognizing that the same double bonds are present in the backbone of both materials. It turned out that an overnight curing step (> 12 h) was a prerequisite to ensure a sufficiently inert, non-reactive PUA surface with clean release of the 2nd PFPE replica. [43] It is worthwhile noting that the fabrication method presented here is highly

reproducible and scalable with an ability to tailor the geometry of replicated micropillars.

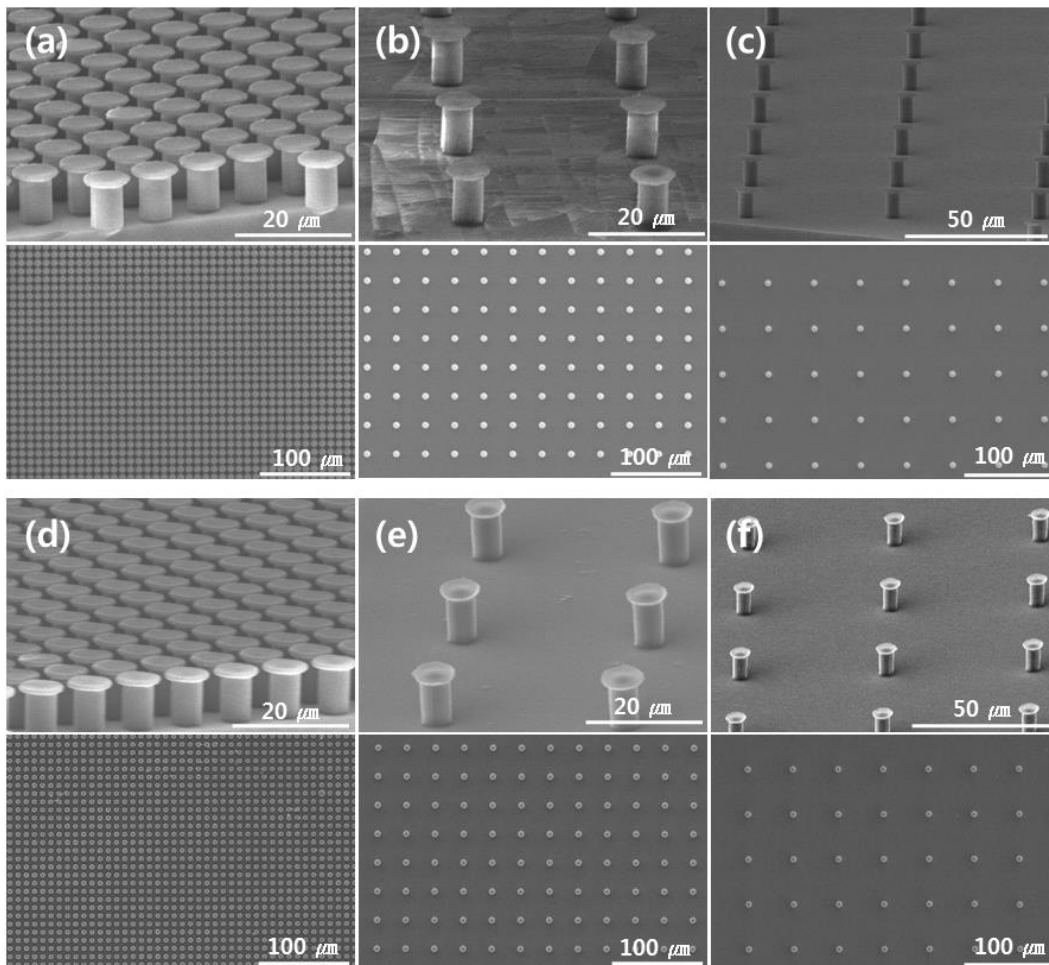


Figure 3-2. The SEM images show that the two structures have the identical geometry after dual duplication processes. SEM images of the fabricated PDMS (a-c) and PFPE micropillars (d-f) with side (upper panels) and top views (lower panels), respectively. The micropillars have 5 μm pillar diameter, 8.5 μm top disk diameter, 10 μm height with different SRs: SR = 1 for (a), (d), 6 for (b), (e), and 10 for (c), (f).

3-3-2. Measurement superomniphobic properties on the fabricated polymer surfaces for optimal design parameters

Figure 3-3 and Figure 3-4 show the measurement of CA and CAH for various re-entrant, mushroom-like structures with 10 different SRs (SR = 1 ~ 10). For consistency, the micropillars of 5 μm diameter and 10 μm heights were used throughout the experiment. The liquids and oils tested here display a wide range of surface tensions (γ_{lv}): water = 72.1 (highest), glycerol = 63, mineral oil = 32, hexadecane = 27.5, and ethanol = 22.3 mN/m (lowest).

Several notable findings are derived from the figures. First, the microstructured PDMS surface shows omniphobic characteristic (CA \sim 160°) regardless of the surface tension of the liquid. According to the Wenzel model, the structured surfaces would be more oleophilic for low surface tension liquids like ethanol. It appears that the wetting state consists of “metastable” configurations where a meniscus is pinned to the undercut profiles of the re-entrant structures. Second, a certain SR is needed to maintain superomniphobicity both on the PDMS and PFPE surfaces. As shown in Figure 3-3(a), water drops prefer to exist in the Cassie-Baxter regime with the increase of SR. No collapse of the drops was observed for the entire SR range. In sharp contrast, for ethanol drops, the SR should be higher than 4 so as to yield superoleophobicity with a CA $>$ 150°. If the SR is too high, i.e., $>$ 7, then the drops started to penetrate into the structures,

resulting in lower CA and higher CAH. Third, a unique wetting profile was observed for the ethanol drops in contact with the PFPE micropillar arrays. For the structured PDMS surfaces, the Cassie-Baxter state was maintained in the range of $SR = 4 \sim 7$ and decayed afterwards, which corresponds to our earlier observations for water drops on structured PDMS surfaces. [44] The initial CA ($\sim 140^\circ$) was relatively higher even for a dense micropillar array ($SR = 1$). For the structured PFPE surfaces, the initial three SRs gave rise to composite wetting states of the Wenzel and Cassie-Baxter models with oleophilicity. At least, the ratio should be higher than 4 to exhibit superoleophobicity. This dramatic wetting transition is not accurately described by the existing wetting models; one possible explanation is that the ethanol has affinity to the fluorocarbon-modified Teflon surface, so that the liquid might collapse into the structures for dense pillar arrays.

Based on these observations, optimal design parameters for both materials can be derived to achieve robust superomniphobicity with a large CA and a lower CAH. Considering difficulty in preparing high aspect ratio master patterns, a microstructured PDMS or PFPE surface with an SR of 5-6 would be optimal to maintain stable superomniphobicity. Therefore, the optimal SR was set at 6 for the conditions used in our experiment, which was used for the transmittance and durability tests unless otherwise noted. Although we have not tested the variation of the pillar height, a sufficiently high micropillar array would be needed to avoid direct contact of a local meniscus to the bottom of the substrate.

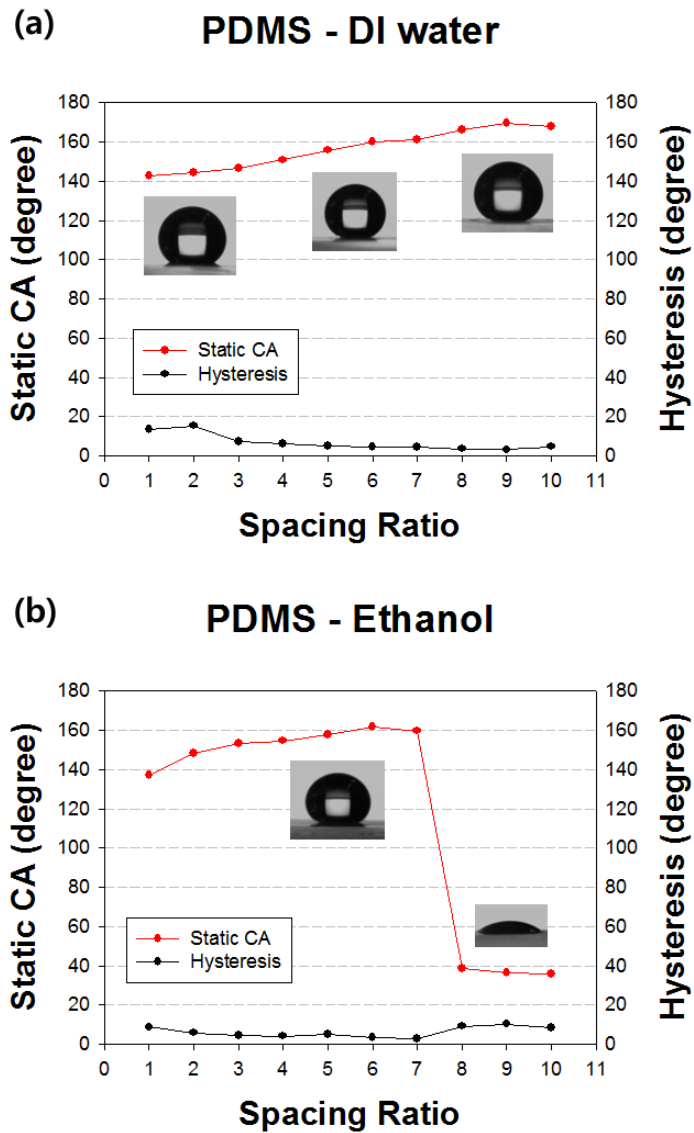


Figure 3-3. Static CAs and CAH graphs of DI water (a) and ethanol (c) on the PDMS micropillar arrays as a function of SR. Inset images are representative CAs at specific SR.

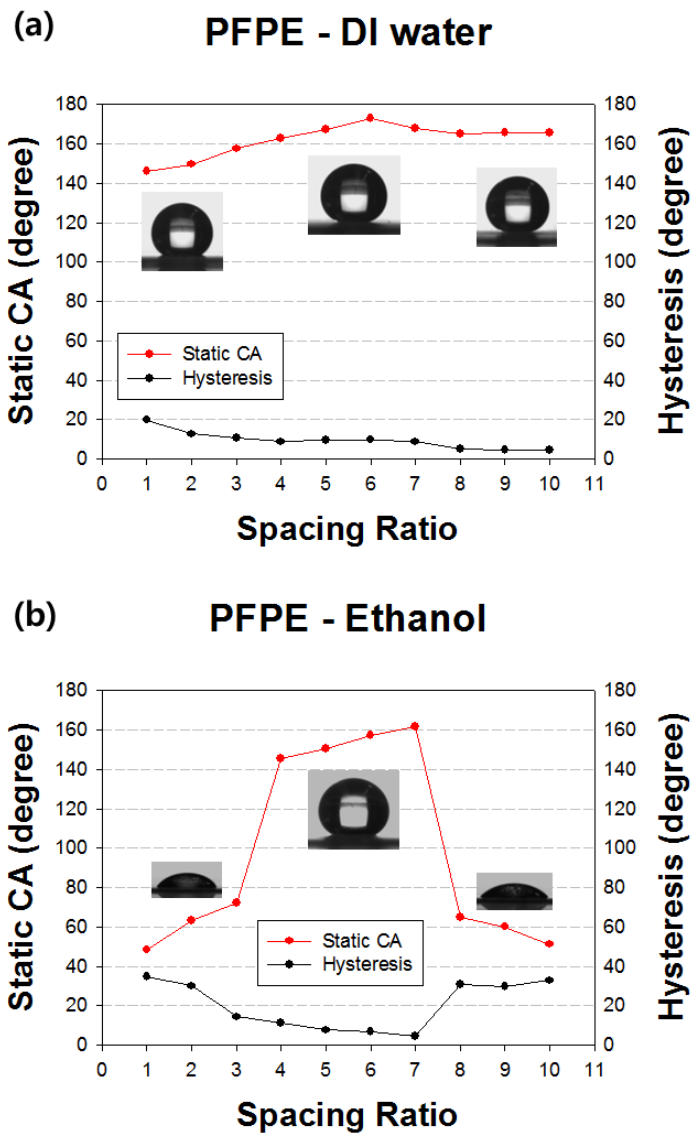


Figure 3-4. Static CAs and CAH graphs of DI water (a) and ethanol (c) on the PFPE micropillar arrays as a function of SR. Inset images are representative CAs at specific SR.

3-3-3. Effect of re-entrant curvature on superomniphobic surfaces

The advantages of mushroom-like, re-entrant profiles of micropillars are well represented in Figure 3-5. Here, the collapse of drops is a result of competition between the internal gravity (P_i) and the critical pressure (P_c , i.e., Laplace pressure),[43-45] which is the maximum sustainable pressure of the Cassie-Baxter state. As shown, the truncated pyramids, which are usual profiles for microfabrication, bring about an immediate collapse of drops since both pressures are acting downward. The overhang structures, which have been employed by many research groups for superomniphobic surfaces, would be useful in resisting the collapse to a certain extent by utilizing the force balance between the two terms. Robust superoleophobicity, however, is hard to expect from this profile as the drops are intrinsically metastable, thus easily penetrating into the structures via external perturbations such as vibration or mechanical loading. It is noted in this regard that the mushroom-like, re-entrant micropillars may be viewed as an extreme case of the overhang structures; the local meniscus would be pinned to the starting point of the undercut profiles (see Figure 3-5(c)), with a strong resistance (or energy barrier) being exerted upward to resist further wetting into the structures. These theoretical descriptions can further be supported by an additional control experiment with regular micropillar arrays of 5 μm diameter and 10 μm height in Figure 3-6. We observed that the wetting angle in this case

was ranged from 60 to 70° for various SRs ($SR < 8$), suggesting that the mushroom-like structure is indeed critical for superomniphobic properties. A trade-off arises here such that the superoleophobicity is diminished by the enhanced solid fraction, i.e., stability of the drops. This appears to be associated with the fact that the surface treatment by C_4F_8 gas polymerization was mainly required in our experiment to obtain superior oleophobicity. For example, the CA of ethanol droplet was increased from 44.1° to 62.5° as a result of the C_4F_8 gas deposition on the PDMS surface. Without such treatment, the surfaces frequently rendered a sharp transition to the Wenzel state even for intrinsic hydrophobic materials like PDMS or PFPE.

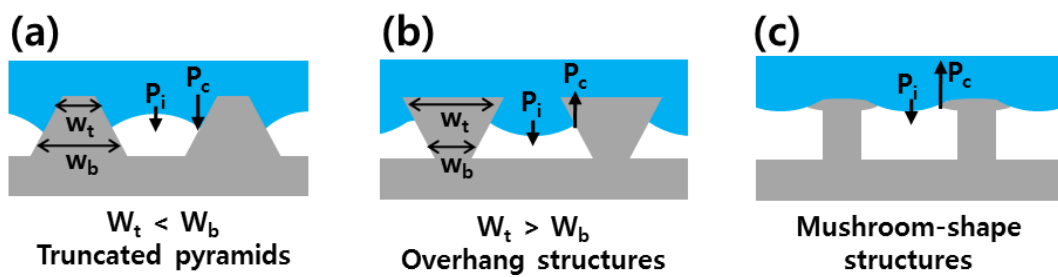


Figure 3-5. Schematic illustrations for the competition between Laplace (P_c) and internal pressures (P_i) of a droplet on truncated pyramids ($W_t < W_b$) (a), overhang structures ($W_t > W_b$) (b), and mushroom-like structures (c). As shown, the mushroom-like shape can be viewed as an extreme case of overhang structures. The arrows denoted relative magnitude and direction of each pressure.

PDMS - Ethanol

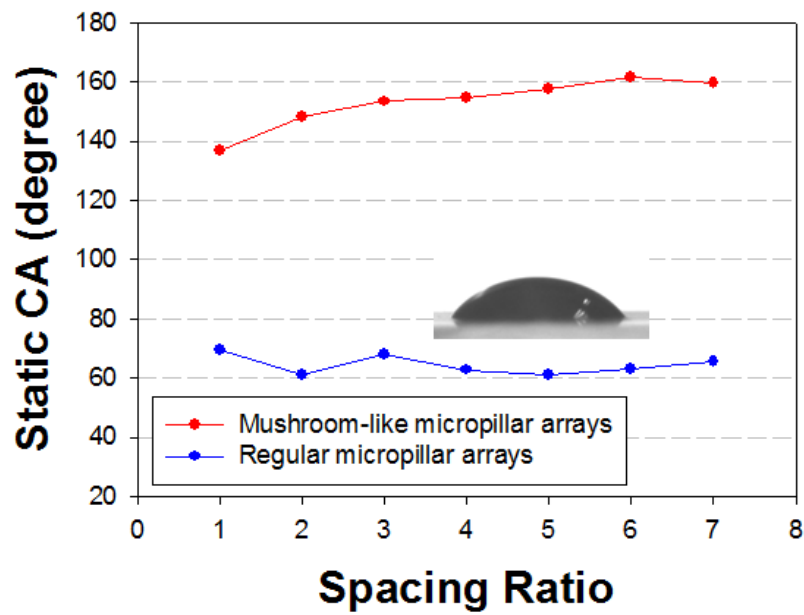


Figure 3-6. Change of static CAs with two types of PDMS micropillar arrays as a function of SR: Red line represents mushroom-like micropillar arrays with ethanol for $SR < 8$, showing superomniphobic properties (see Figure 3-3(b)). Blue line is for regular micropillar arrays having $5 \mu\text{m}$ pillar diameter and $10 \mu\text{m}$ height. The inset photograph shows the wetting shape of ethanol on the surface.

3-3-4. Additional test for various useful applications: (1) Transparency

In addition to superoleophobic properties, we investigated the transparency of the fabricated polymer surfaces with UV/VIS transmittance spectra, for potential applications to flexible display or home appliances. In these applications, windshield and anti-wetting windows would become more and more important to prevent contamination from water and organic liquids. [29, 30, 46] Figure 3-7(a) shows the transmittance profiles of various samples including a bare PDMS, a structured PDMS surface (no C_4F_8 treatment), and structured PDMS and PFPE surfaces with C_4F_8 treatment. The transmittance of a bare PDMS was 93 ~ 94 % in the visible spectral range from 380 to 780 nm, which was slightly reduced to < 90 % (PDMS: 88 ~ 89 %, PFPE: 86 ~ 88 %) when the surfaces were structured with pillar arrays. Nonetheless, the visibility was not significantly deteriorated as seen from the transparent text images in Figure 3-7(b). The relatively large distance between micropillars ($SR = 6$) as well as the small thickness of the deposited layer of fluorocarbon compounds (~50 nm) may attribute to the transparency of fabricated superomniphobic surfaces. These superior optical properties are potentially beneficial for optical applications such as Figure 3-8.

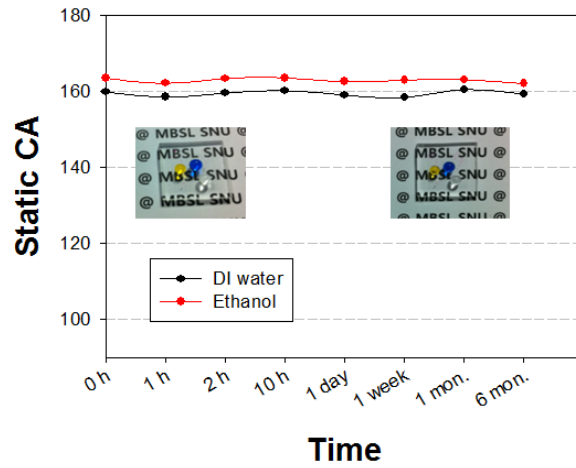


Figure 3-8. Demonstration of superomniphobic surfaces on touch-phone screens. The left figure shows that the superoleophobic surface (PDMS micropillar arrays, $SR = 6$) is not contaminated by various liquids: DI water (transparent), mineral oil (blue), hexadecane (red) and ethanol (yellow). In contrast, the unmodified surface on the right is immediately wetted by the liquids upon contact.

3-3-5. Additional test for various useful applications: (2) Long term stability

Finally, we tested durability of the PDMS and PFPE superomniphobic surfaces at ambient conditions. Figure 3-9 demonstrates the robustness of superomniphobicity using the mushroom-like micropillars of $SR = 6$ over a time period of 6 months, in which no noticeable changes or degradations were observed. The inset photographs show the CAs of various liquids: DI water (transparent), mineral oil (blue), hexadecane (red) and ethanol (yellow) at different time points, indicating that the superomniphobicity can be maintained without aging effects.

(a) Aging Effect of PDMS sample



(b) Aging Effect of PFPE sample

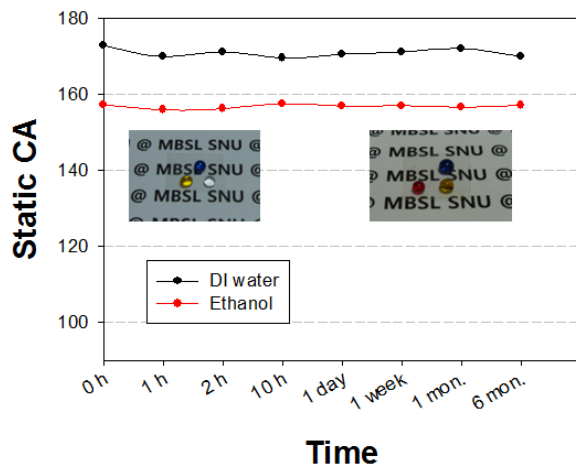


Figure 3-9. (a-b) Measurement of static CAs of the PDMS (a) and PFPE (b) samples (SR = 6) over a time period of 6 months. Inset photographs show the CAs of various liquids: DI water (transparent), mineral oil (blue), hexadecane (red) and ethanol (yellow) at different time points.

3-4. Summary

In this chapter, we have presented a simple fabrication approach to make superomniphobic surfaces with high transmittance ($> 90\%$) and durability (< 6 months). By utilizing re-entrant, mushroom-like structures, which has proven useful in the field of dry adhesives, both superhydrophobic and superoleophobic surfaces were achieved in a one-step molding (replication) process. The method is based on well-established soft lithographic microfabrication, allowing for a simple and low-expertise route to the fabrication of superoleophobic surfaces. Also, the method is applied to other thermal or UV-curable materials, and scalable to the 4 inch wafer level with excellent reproducibility and robustness.

Based on the measurements of CA and CAH of water and ethanol drops, we have derived optimal design parameters for PDMS and PFPE materials: the SR needs to be in the range of $4 \sim 7$ to maintain robust superomniphobicity with an optimum SR of ~ 6 for both materials. Also, the structured surfaces were optically transparent and durable over a long period of time. Despite these advantages, there are potential shortcomings of the current approach. Since the materials are polymer based, the surfaces would be mechanically weak, being prone to scratch, UV, or other harsh environments. Also, the C_4F_8 gas surface treatment was required to render superomniphobicity even for intrinsic hydrophobic materials like PDMS and PFPE. These issues are consistently under investigation to

achieve more viable superomniphobic surfaces. It is envisioned that this simple, yet robust fabrication method would be useful in a wide range of applications in which water and oil-repellent surfaces are required without harsh environmental conditions.

Chapter 4. Directional Water/Oil Sliding Surfaces with Bioinspired Hierarchical Anisotropic Groove Microstructures

Published in *Advanced Materials*, 2013, 25, 5756–5761

4-1. Introduction

Since the discovery of superoleophobic surfaces by Cohen and co-workers,[13] the surfaces that can repel the wetting of various liquids with a wide range of surface tensions have been extensively studied both theoretically[14, 47] and experimentally. [20, 48-51] In general, negative slope structures such as overhang or re-entrant shapes have been employed to resist the energetically favourable Wenzel state. More recently, Aizenberg and co-workers demonstrated remarkable slippery surfaces against liquids of low surface tension by exploiting liquid-infused porous structures. [52] These oil sliding surfaces have many potential applications in microfluidics, mobile market, and oil transportation and semiconductor industry to transport or collect remaining oil efficiently as well as to prevent contamination from the oil. [21, 26, 53-55]

Despite the above significant findings, simple omniphobic surfaces are not capable of inducing a directional oil sliding property even in the presence of high

contact angle (CA) ($> \sim 150^\circ$) and low contact angle hysteresis (CAH) ($< \sim 10^\circ$). This is due to the fact that the omniphobic surfaces usually consist of randomly distributed re-entrant texture or regular arrays of beads or pillars. In contrast to anisotropic oil sliding surfaces, anisotropic wetting[56] or sliding surfaces of water have been well documented with inspirations from nature such as spider web,[57] water-strider legs,[58] butterfly wings[59] and rice leaf. [54, 60] In this case, water droplets tend to move along the parallel direction of the topographically-defined surfaces owing to energy barrier principles, which causes a sliding angle difference from the perpendicular direction. [61, 62] It is also well established that the anisotropic wetting properties can be controlled by modifying topography[63-65] and/or chemical treatment of surfaces. [66, 67]

In this chapter, we present a directional oil sliding surface utilizing re-entrant, anisotropic micro-groove arrays inspired from the microgrooves of rice leaf, so as to secure two primary goals of “omniphobicity“ and “anisotropic sliding“. For the fabrication, a UV-assisted micromolding process with a mixture of photoinitiator and acrylate functionalized prepolymer containing aluminium oxide nanoparticles (Al_2O_3) was used, which offers a geometry-controllable, cheap and low-expertise route to the generation of a superhydrophobic hierarchical structure. Three different cross-sectional shapes of the microgrooves were employed to investigate the entry effect: prism, rectangle, and overhang structures. [68] It was found that the surfaces with overhang line arrays allowed for anisotropic oil

sliding surfaces as judged by low CAs and sliding angles (SAs) with mineral oil ($\gamma_{lv} = 28 \text{ mN/m}$) and conventional photoresist (AZ 1512).

4-2. Experimental

4-2-1. Rice leaf surface

The surface morphologies of a rice leaf are shown in Figure 4-1(a-b), in which wavy structures are shown, consisting of microgrooves of 100 μm width with micro-scale papilla and nano-scale waxes similar to those on a lotus leaf. [54] A droplet of water (volume of 5 μl , $\gamma_{lv} = 72.1 \text{ mN/m}$) placed on the rice leaf displays superhydrophobicity and smoothly slides in the direction of microgrooves (Figure 4-1(c)). Upon dispense of a mineral oil (volume of 5 μl , $\gamma_{lv} = 28 \text{ mN/m}$) on the rice leaf, however, the surface was completely wetted by the oil (Figure 4-1(d)). This suggests that liquids with lower surface tension than water could not maintain a metastable composite solid-liquid-air interface on a rice leaf-like wavy textured surface. This leads us to propose a new design principle for a highly oil sliding surface that may deviate from an optimal water-repelling/sliding surface observed on a rice leaf.

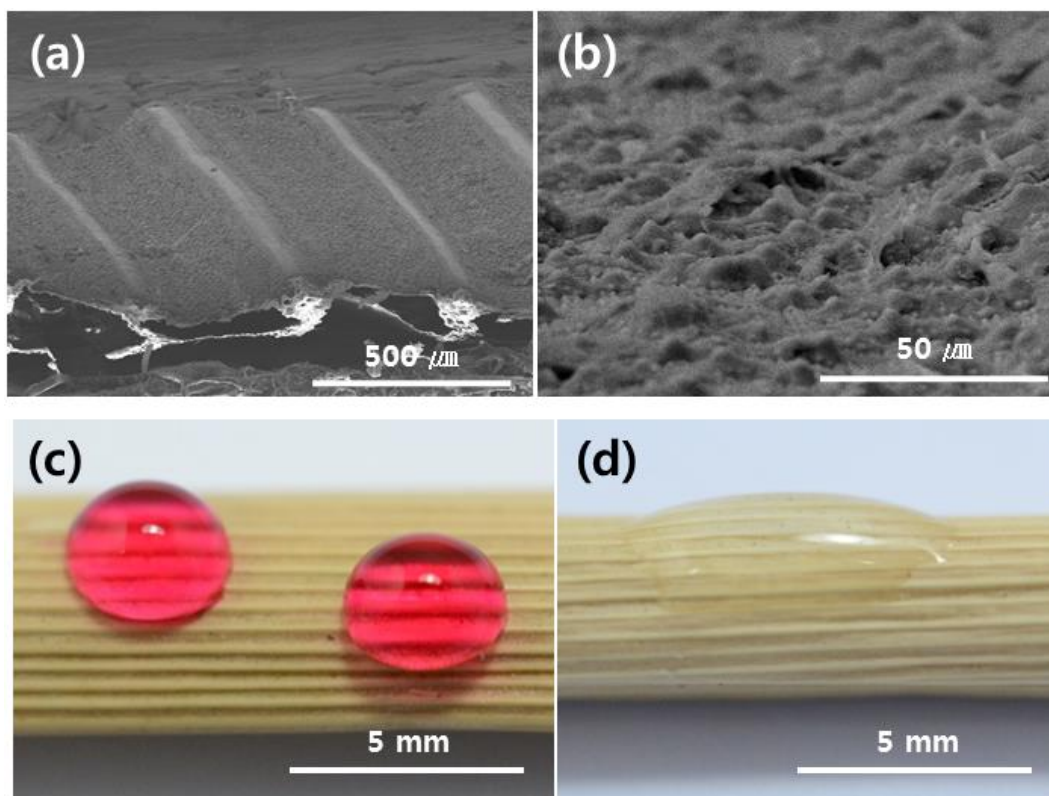


Figure 4-1. (a-b) SEM images for rice leaf surface at two different magnifications. (c-d) Photographs of water (red) and mineral oil (transparent) droplets (volume of 5 μ l) placed on the rice leaf surface.

4-2-2. Preparation of water/oil sliding surfaces

Figure 4-2 shows a schematic fabrication process, which was comprised of replica molding (see *Chapter 2-4*), ozone treatment, and hydrophobic surface treatment. Briefly, the line structures were replica-molded from its respective master using a UV-curable polyurethane acrylate (PUA) precursor mixed with Al_2O_3 nanoparticles of 40 nm diameter. Then, the replica was irradiated to ultraviolet ozone (UVO) for several minutes to expose the nanoparticles while selectively removing the polymer resin. To make the dual-scale surfaces even more omniphobic, hydrophobic chemical treatment was carried out on the surfaces by using octafluorocyclobutane (C_4F_8) gas.

In details, a nanoparticle-embedded prepolymer was purchased from BYK Chemie (product number NANOBYK-3602), which consists of 1,4-hexanediol diacrylate (70 wt%) and Al_2O_3 nanoparticles with 40 nm diameter (30 wt%). As a photoinitiator, Darocur 1173 (2-hydro-2-methyl-1-phenyl-1-propane, Ciba Specialty Chemicals, Switzerland) was mixed in a weight ratio of 5. Then, a blended UV curable precursor was dispensed onto the prepared mold and a polyethylene terephthalate (PET) film (50 μm thickness) was slightly placed on the liquid drop as a supporting layer. The precursor was exposed to UV light ($\lambda = 250\text{--}400$ nm, intensity of ~ 100 W/cm^2 , Fusion Cure System, Minuta Tech, Korea) under different curing time (~ 30 seconds for prism patterned PUA mold and ~ 3

minutes for square and overhang PDMS molds). After separation from the mold, the micro-patterned surfaces were exposed to ultraviolet ($\lambda = 254$ and 185 nm) ozone (UVO) for 10 minutes. During exposure, polymer at the surface decomposes by oxidation reaction with activated oxygen radicals whereas alumina nanoparticles remain in their position, resulting in a nanoscale roughness on the surface. [69] Finally, the fabricated surfaces were treated using C_4F_8 gas for 10 seconds (2000 W ICP power, 10 V bias voltage, 25 mTorr pressure, 150 sccm gas flow rate) in a deep reactive ion etch (DRIE) system (Versaline ICP, Plasma-Therm inc.).

To find an appropriate entry shape with dual-scale architecture, we used three different types of equally-spaced microgrooves: prism (20 μm width), rectangular (20 μm width), and re-entrant line arrays (20 μm bottom and 30 μm top widths). All three structures had the same height of ~ 20 μm , such that the dimensions are similar except for the cross-sectional profile. For the prism and rectangular molds, the fabrication scheme is shown in Figure 4-3.

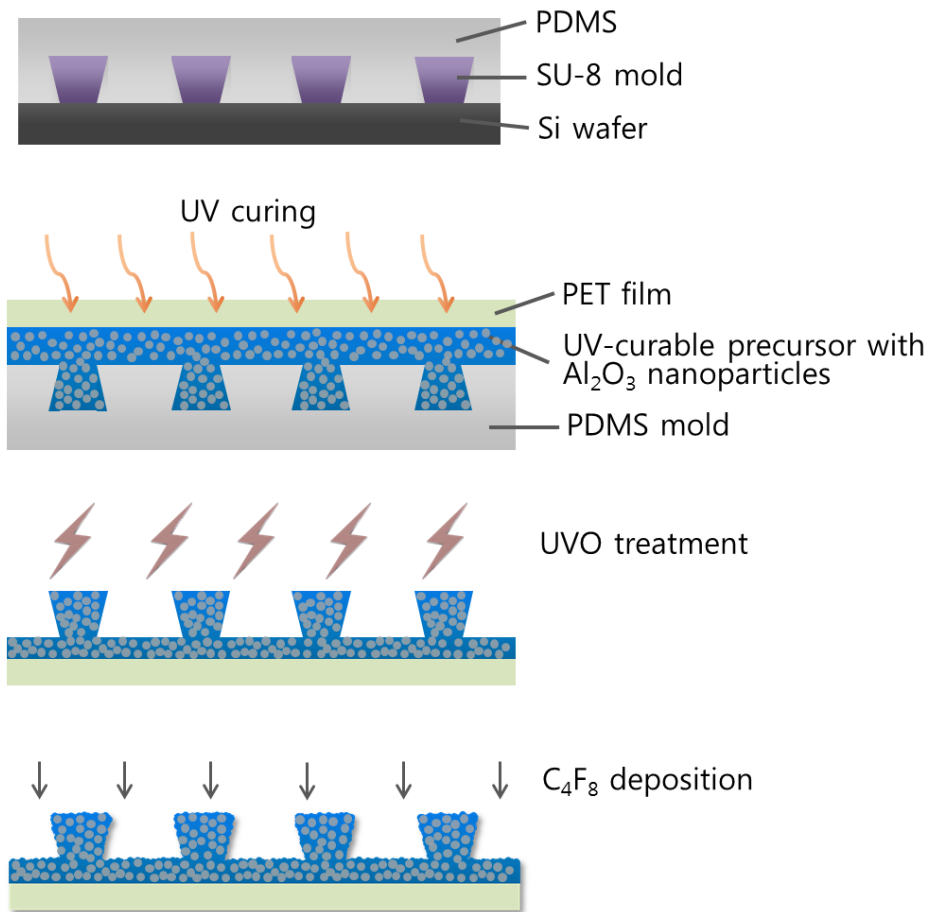


Figure 4-2. Fabrication scheme of anisotropic line arrays with dual-scale hierarchical roughness.

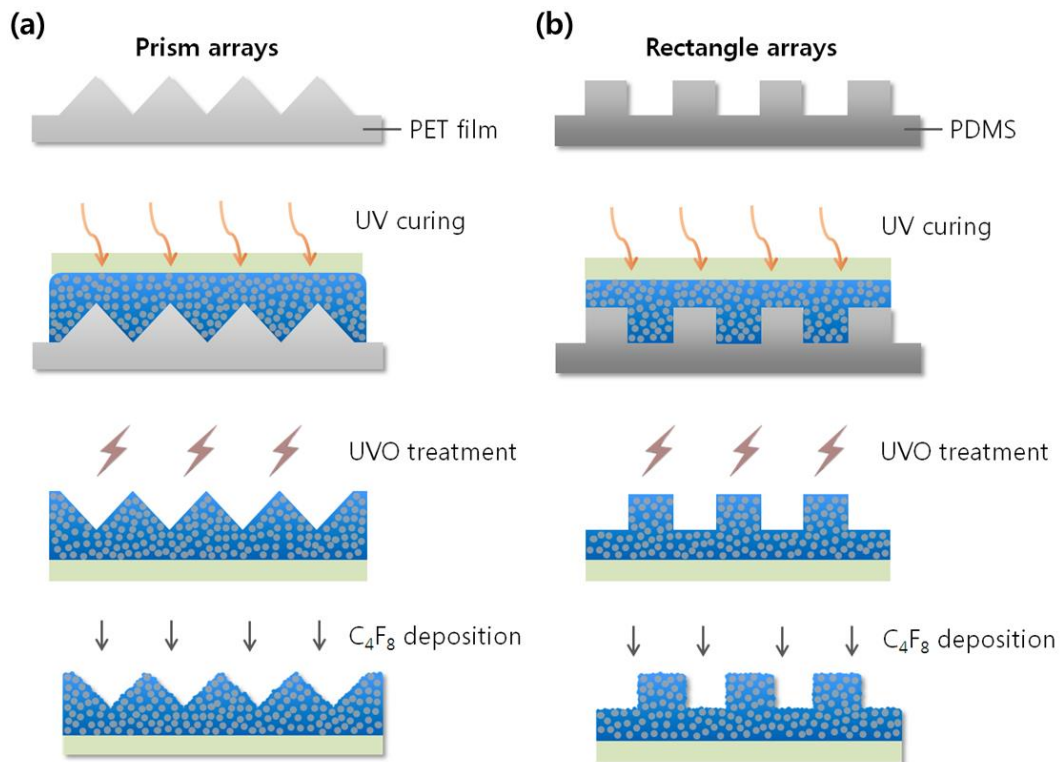


Figure 4-3. Fabrication scheme of dual-scale prism (a) and rectangle (b) line arrays. The dimensions of the three line arrays were chosen in such a way that length scales are similar except for the cross-sectional profile.

4-2-3. Sample characterization

The static CAs and SAs were measured at ambient temperature using a contact angle analyzer (Drop Shape Analysis System DSA100, Kruss, Germany). The static CAs were measured by gently placing a small volume of drop ($\sim 5 \mu\text{l}$) onto the fabricated surfaces. The SAs were measured by tilting the substrate until the droplets started to slide. The morphologies were examined by a HITACHI S-48000 scanning electron microscope (SEM, Hitachi, Japan) at 5 kV. To avoid charging effects on the surfaces, a platinum (Pt) layer with 20-nm-thickness was deposited prior to measurement.

4-3. Results and Discussion

4-3-1. Morphologies of fabricated rice-leaf-inspired line arrays

SEM images of the fabricated line arrays with three different cross-sectional shapes are shown in Figure 4-4, in which the structures have high pattern fidelity with well-defined edge profiles. In order to indicate the shape anisotropy, two directions were defined as ‘parallel’ and ‘perpendicular’ with respect to the groove direction (see Figure 4-4(a)). Figure 4-4(d-f) exhibit magnified cross-sectional SEM images of the structures, clearly demonstrating the dual-scale roughness with exposed nanoparticles. Compared with the microgroove arrays prior to UVO treatment (see Figure 4-5), the entire surfaces including the top, front and side locations have nanoscale roughness via the exposure of 40 nm diameter Al_2O_3 nanoparticles (see each inset image of Figure 4-4(d-f)). Also, the structures were neatly formed over large areas with high integrity and less defects, as shown in Figure 4-6.

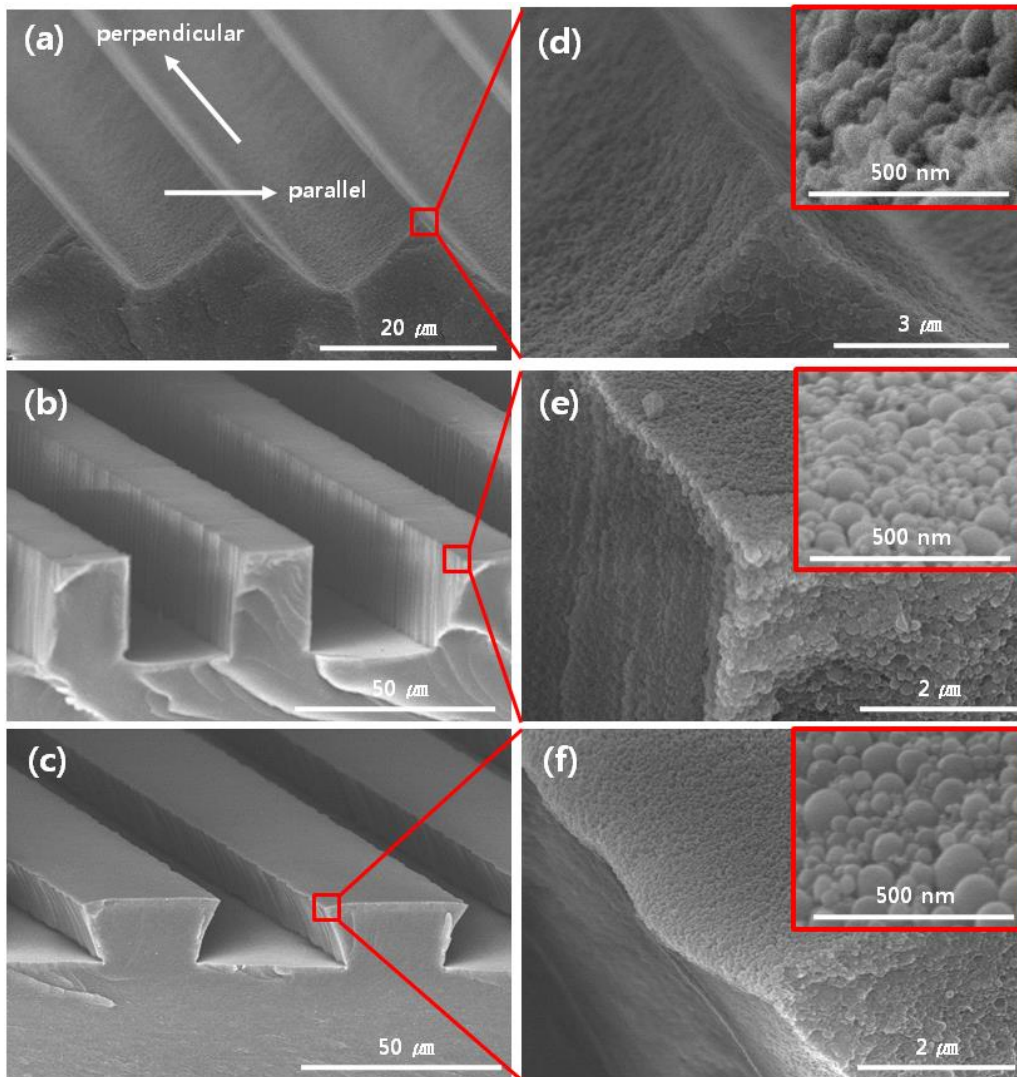


Figure 4-4. (a-c) SEM images of prism, rectangle and overhang groove microstructures where each magnified view is shown in (d-f). The arrows indicate the parallel and perpendicular directions with respect to the direction of microgrooves. The inset clearly shows the presence of a nanoroughness with 40 nm- Al_2O_3 nanoparticles after UVO treatment.

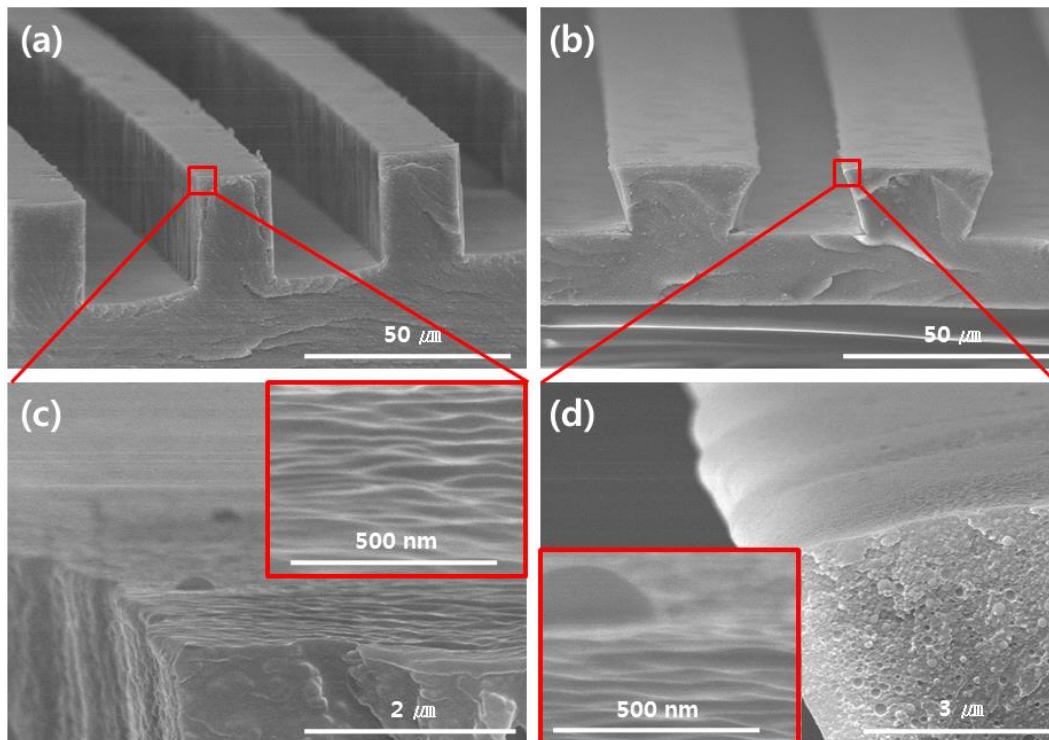


Figure 4-5. SEM images of micro-only line arrays with rectangle (a) and overhang (b) shapes. (c-d) Magnified SEM images of the fabricated micro line arrays where the inset shows smooth surface without nanoroughness.

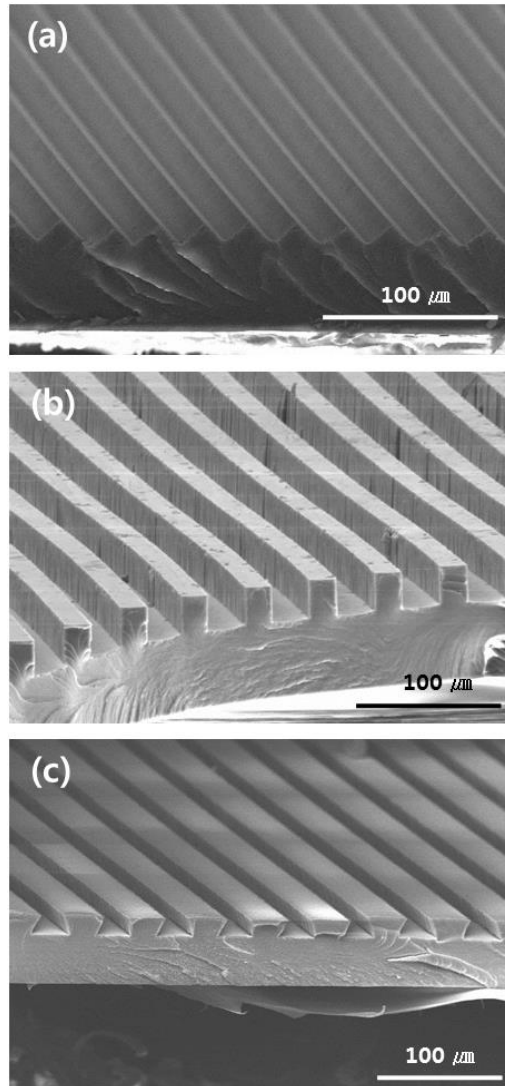


Figure 4-6. These SEM images indicate that the fabrication can be conducted over large areas with high physical integrity and pattern fidelity.

4-3-2. Directional hydrophobicity on the fabricated surfaces

With the various microgrooves with different entry shapes, we measured static CAs (advancing + receding) and SAs for water as shown in Figure 4-7. First, the hydrophobicity of DI water was significantly improved on the dual-roughness surfaces with all the three groove microstructures (Figure 4-7(a-b)). As is well known, these non-wetting phenomena are associated with the dual-scale roughness that can possess an air pocket underneath a water droplet. [22, 70] As a consequence, the SA of water on the hierarchical prism arrays was much lower than that of micro-only prism arrays. For the dual-scale hierarchical prism arrays inspired from rice leaf, the surfaces exhibited low SAs along the parallel and perpendicular directions with 4° and 10° (for a $5 \mu\text{l}$ droplet of DI water), respectively, being similar to those of the actual rice leaf ($\sim 3^\circ/9^\circ$). [54] Such a synergistic role of nanoroughness on the anisotropic water sliding surface was also confirmed from the increase of perpendicular CAs in the rectangle and overhang hierarchical line arrays (Figure 4-7(a)) and the decrease of SAs in the same hierarchical patterns (Figure 4-7(b)). The largest CA on the dual-scale prism-shape line arrays is readily understood according to the Cassie-Baxter equation, in that the solid fraction of the liquid-solid-air interface becomes minimized on the prism shape (Figure 4-8 for CA images).

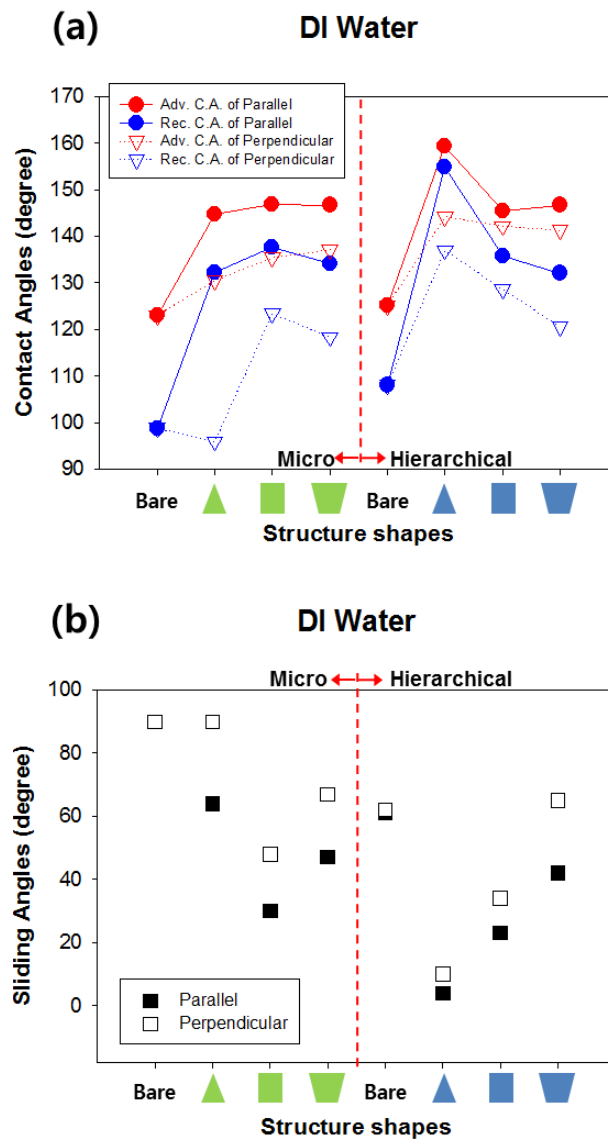


Figure 4-7. Advancing and receding CAs (a) and SAs (b) of DI water on the fabricated surfaces (flat, prism, rectangle and overhang structures, respectively) along the parallel and perpendicular directions. The SA of 90° means that the droplet would not slide on the surface with any tilting angle of substrate.

		Bare	Prism		Rectangle		Overhang	
			//	⊥	//	⊥	//	⊥
Micro Only	DI Water							
	Mineral Oil							
Hierarchical	DI Water							
	Mineral Oil							

Figure 4-8. CA images of DI water and mineral oil on the various microgroove structures in the parallel and perpendicular directions.

4-3-3. Directional oleophobicity on the fabricated surfaces

Next, we investigated the CAs and SAs of mineral oil on the fabricated surfaces as shown in Figure 4-9. In accordance with the Cassie-Baxter theory, both the advancing and receding CAs along the parallel direction increased linearly with the decrease of edge angle in the order of prism < rectangular < overhang for the micro-only and hierarchical groove structures. In contrast, the CAs in the perpendicular direction exhibited less dependence on the edge angle, with the values much lower than those of DI water. This is due to the fact that the oil penetrates into the grooves to a certain depth, so that the solid fraction is elevated per each entry geometry (see Figure 4-10).

The SAs shown in Figure 4-9(b) reveal more intriguing behaviors. First, the SAs on the prism and rectangular line arrays were immeasurable since the oil directly wetted the surfaces upon being inclined (indicated as “Wenzel” in Figure 4-9(b)). This suggests that the surfaces are highly metastable and prone to collapse even with a small perturbation such as inclining. Second, only the overhang line arrays demonstrated sliding at a certain angle where the hierarchical surface rendered a higher SA than that of the micro-only grooves. This is opposite to what has been observed for water droplets: the presence of nanoroughness generally contributes to a larger CA as well as a smaller SA as seen from the lotus effect. Based on this observation, we conclude that the oil is able to wet the

nanoroughness due to its low surface tension, and thus the “microstructure only” would be more appropriate in designing an oil repelling/sliding surface.

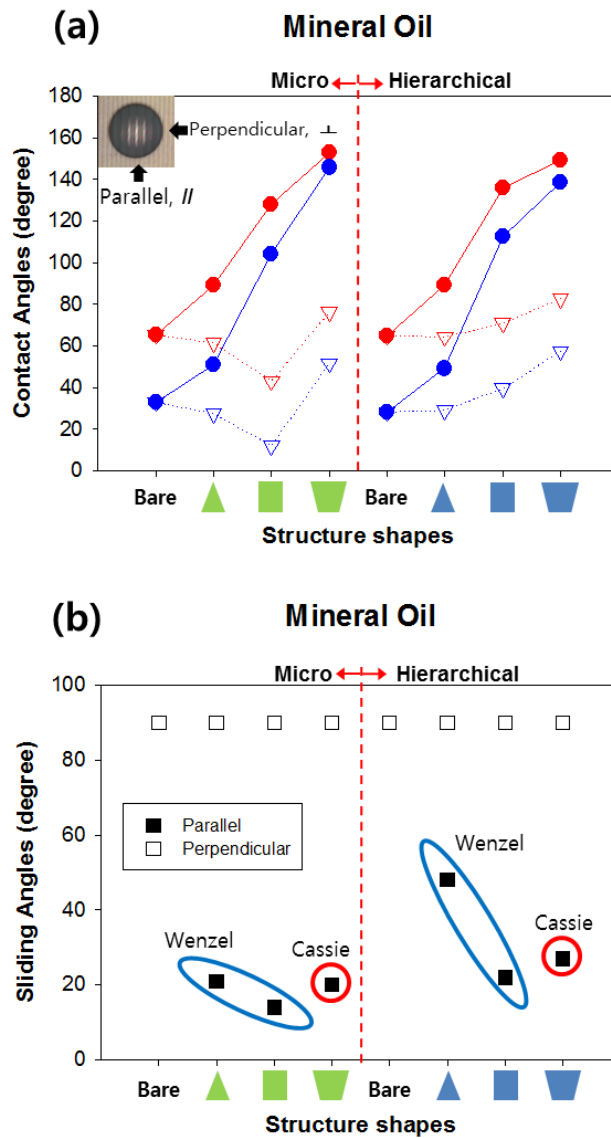


Figure 4-9. Advancing and receding CAs (a) and SAs (b) of mineral oil on the fabricated surfaces (flat, prism, rectangle and overhang structures, respectively) along the parallel and perpendicular directions (see the inset image).

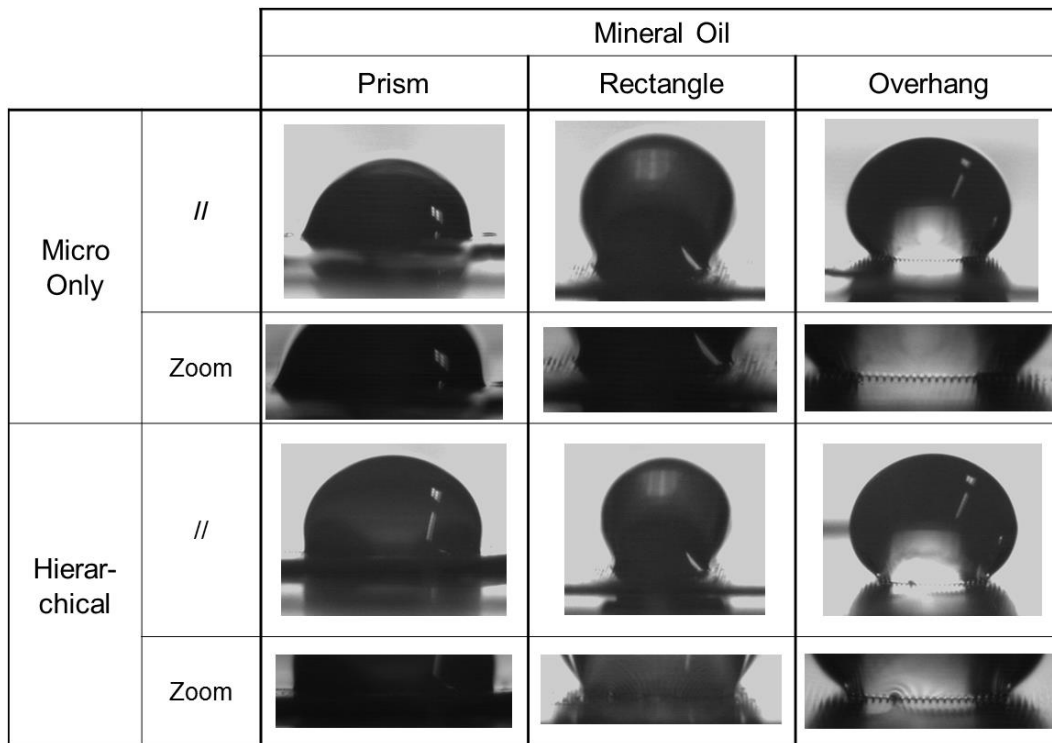


Figure 4-10. Optical microscope (OM) images showing the existence of air pocket between a mineral oil and an underlying overhang structure (see the zoomed areas). In the case of prism and rectangle structures, the grooves were wetted by the oil. In particular, the overhang structures were not wetted before and even after an external perturbation such as inclining, which means that the surface is stable with the Cassie state.

4-3-4. Theoretical analysis of directional oil sliding phenomenon

To elaborate on these anisotropic sliding behaviors, a simple theory is presented in Figure 4-11 and Figure 4-12 based on the competition between internal gravity (P_i) and Laplace pressure (P_c). [44] As shown in Figure 4-11(a), both pressures are acting downward in the prism and rectangle structures, so that the surfaces would be initially metastable with the trapped air and then prone to collapse with a small perturbation. In contrast, the overhang structures would be more stable since the Laplace pressure is resisting against the gravity. For an oil droplet of 5 μl , for example, P_c can be written as

$$P_c = -\frac{\gamma f \cos \theta^*}{(1-f)(A/L)}$$

where γ is the surface tension of mineral oil ($= 28 \text{ mN/m}$), f is the solid fraction at the liquid-solid-air interface ($= 0.6$), θ^* is the equilibrium contact angle on flat surface ($= 62^\circ$), A is the cross sectional area ($= 5 \times 10^{-10} \text{ m}^2$), and L is the perimeter of overhang structure ($= 6.12 \times 10^{-5} \text{ m}$). For the conditions used in this work, the calculated P_c is about $2.4 \times 10^3 \text{ Pa}$. On the other hand, P_i can be calculated as

$$P_i = \frac{V\rho g}{A_{\text{contact}}} = \frac{V\rho g}{\pi(R(\theta))^2}$$

$$R(\theta) = \left[\frac{6V}{\pi(1-\cos\theta)(3\sin^2\theta + (1-\cos\theta)^2)} \right]^{\frac{1}{3}}$$

where V is the volume of a liquid droplet ($= 5 \times 10^{-9} \text{ m}^3$), ρ is the density of liquid ($= 0.8 \times 10^3 \text{ kg/m}^3$), g is the gravitational constant ($= 9.8 \text{ m/s}^2$), $R(\theta)$ is the radius of droplet on the fabricated surface ($= 1.065 \times 10^{-3} \text{ m}$), θ is the static CA of droplet ($= 150^\circ$). The calculated P_i is about $1.1 \times 10 \text{ Pa}$. Therefore, it can be said that P_c ($= 2.4 \times 10^3 \text{ Pa}$) is high enough to withstand the collapse of an oil droplet exerted by P_i ($= 1.1 \times 10 \text{ Pa}$), and the droplet could slide smoothly on the overhang structure without the wetting transition from Cassie to Wenzel state.

Also, it is worthwhile noting that the SAs in the perpendicular direction were all 90° , meaning that the sliding was not observed for all the tested shapes. A liquid with low surface tension such as mineral oil would form the meniscus at an intermediate point of the grooves as illustrated in Figure 4-11(b). This appears to be in contrast to the wetting of DI water; only the upper surface of structures would be wetted by DI water (see Figure 4-12(b-c)). Thus, the critical angle ($\theta_{c,w}$), which acts as the energy barrier against the sliding of a droplet, would be higher with the oil than the water. Namely, the critical angle of DI water ($\theta_{c,w}$) is similar to or slightly higher than the equilibrium CA on a planar surface (θ_w^*), $\theta_{c,w} \sim \theta_w^*$, whereas a higher critical angle of oil is expected. i.e., $\theta_{c,o} = \theta_o^* + (180 - \alpha_o)$ in which α is the edge angle subtended by the different microstructures (prism, rectangular, or overhang). [50, 71] It is noted that the $\theta_{c,o}$ would be always larger

than $\theta_{c,w}$, suggesting that it is more difficult for an oil droplet to overcome the energy barrier associated with the sliding to the perpendicular direction. According to the geometric conditions of the overhang structure ($\theta_w^* = 120^\circ$, $\theta_o^* = 65^\circ$ and $\alpha_o = 75^\circ$), the calculated values are $\theta_{c,w} \sim 120^\circ$ and $\theta_{c,o} = 170^\circ$. Based on this simple analysis, the oil droplet would not slide along the perpendicular direction with any tilting angle of substrate, in good agreement with our experimental observations (Figure 4-9(b)).

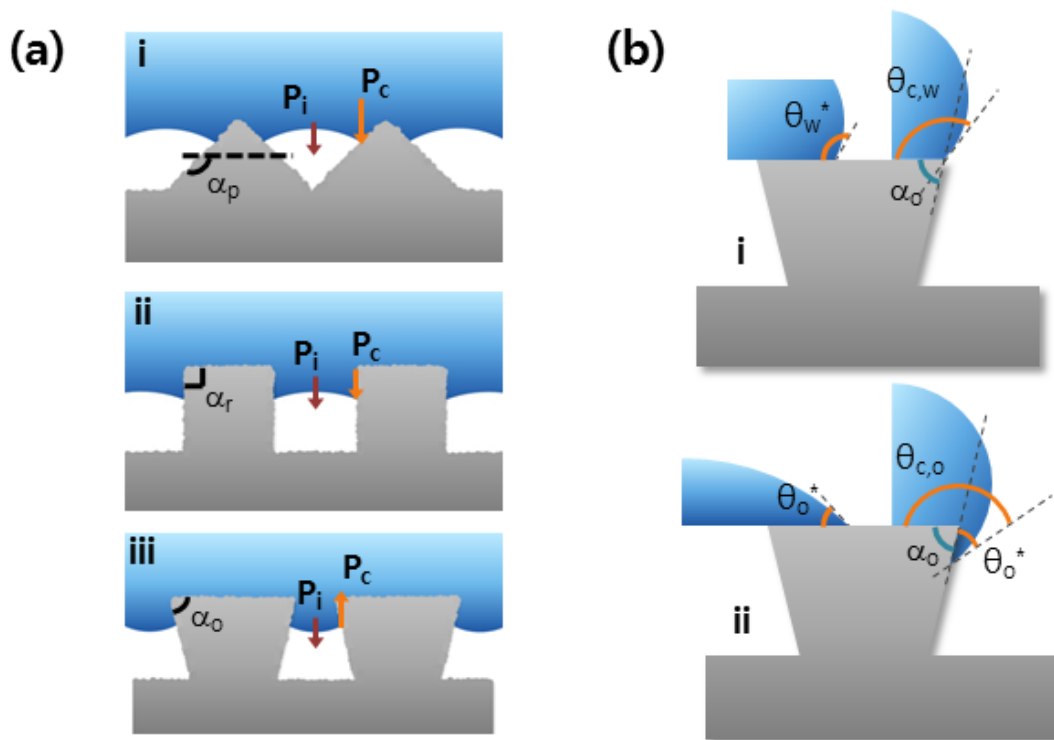


Figure 4-11. (a) Schematic illustration for the competition between internal (P_i) and Laplace (P_c) pressures of an oil droplet on the prism (i), rectangle (ii), and overhang structures (iii). The arrows indicate the direction and relative magnitude of each pressure. The edge angle α is determined by the cross-sectional shape of microgrooves. (b) Schematic illustration of critical contact angle at the edge in the perpendicular direction for DI water (i) and mineral oil (ii).

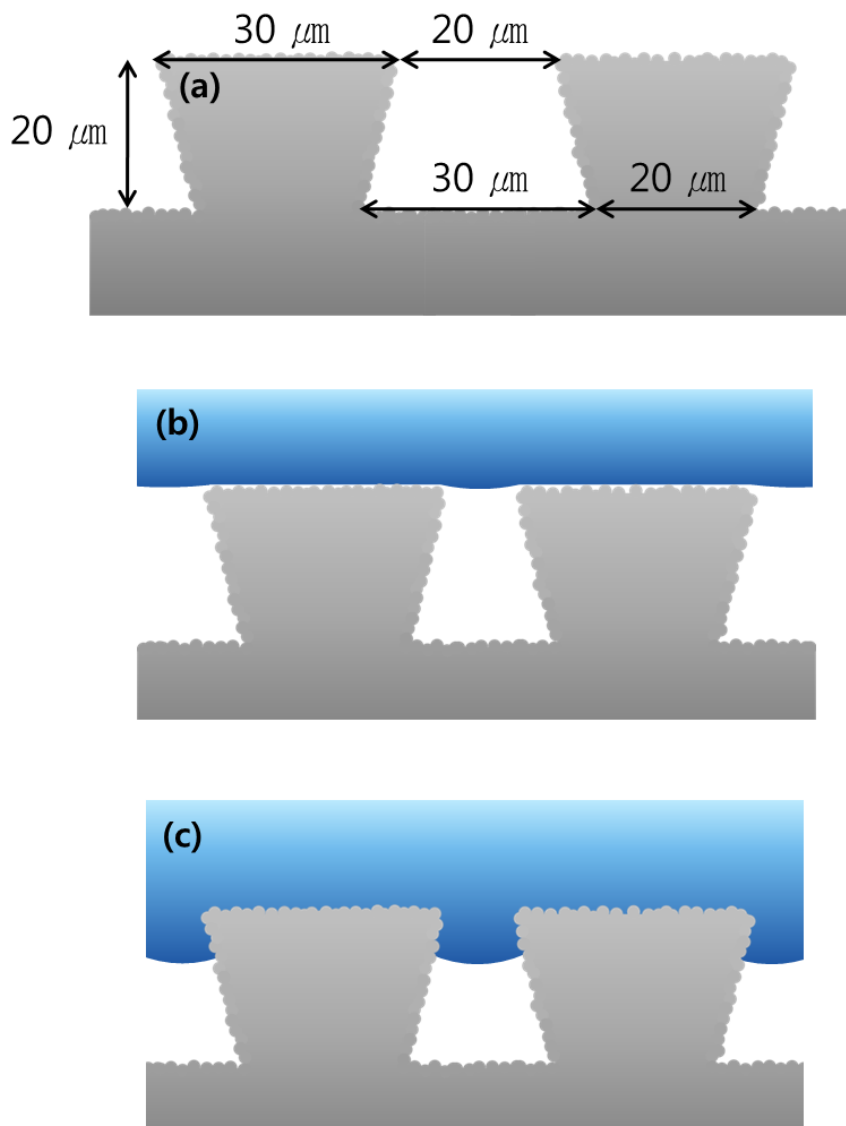


Figure 4-12. (a) Geometric description of overhang structures. Liquid-solid-air interface with DI water (b) and mineral oil (c) on the fabricated overhang structures.

To represent the asymmetric oil sliding property mentioned above, we introduce a suitable design parameter, termed “Anisotropic Factor (AF)“, which is defined as[56]

$$AF = \sin\left(\frac{|\theta_{//} - \theta_{\perp}|}{2}\right)$$

where $\theta_{//}$ and θ_{\perp} are the SAs in the parallel and perpendicular directions, respectively. Therefore, AF is a measure of the difference of two SAs, and can be used to predict/describe how the surface has the potential to guide the migration of a droplet in one direction. Shown in Figure 4-13 is the plotted AF for two liquids of DI water and mineral oil on the fabricated surfaces. The AF of DI water on the hierarchical prism structure is similar to that of rice leaf (AF ~ 0.052). For reference, the AF of lotus leaf is essentially zero, indicating that the surface shows isotropic sliding in any direction. As previously described, the AF of oil can be made much larger than that of DI water by utilizing the re-entrant microgrooves. Taken together, the overhang line arrays without nanoroughness possess anisotropic oil sliding properties at the expense of slightly reduced water repellency.

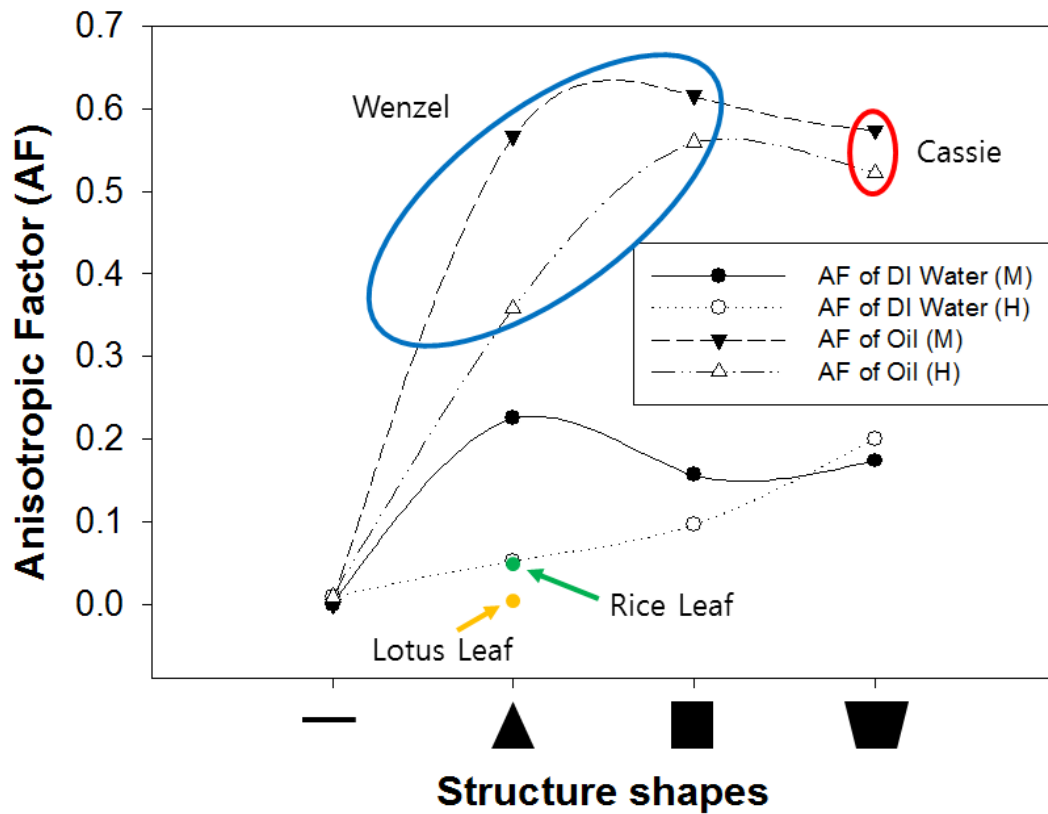


Figure 4-13. Anisotropic factors (AFs) on the fabricated surfaces with DI water and mineral oil where the characters *M* and *H* represent micro only and hierarchical structures, respectively. The rice leaf has a low AF of 0.052 and that of lotus leaf is almost zero.

4-3-5. Additional experiments using directional sliding properties for practical applications

By taking advantage of the anisotropic omniphobic sliding surfaces presented here, we demonstrate three experiments for the potential uses of overhang line arrays. First, Figure 4-14(a) shows spontaneous sliding of conventional photoresist (AZ1512) on an inclined surface with the oil sliding surface shown in Figure 4-4(c). In contrast to the wetted flow on the rice leaf-like prism arrays (i), the PR droplet was smoothly sliding on the overhang structures (ii), which would be particularly useful for the cleaning of spin-coating machine. Second, we designed a S-shaped track to guide the sliding of a mineral oil as shown in Figure 4-14(b). Here, the inverse-character *S* was prepared with the overhang line arrays along the curved direction. Upon tilting the substrate, the mineral oil droplet started to slide along the line arrays indicated by the arrows.

In addition to anisotropic sliding properties for an oil droplet, we investigated line tracing ability of several droplets of water and mineral oil. Figure 4-14(c) shows the initial shapes of water and mineral oil drops on the horizontal and inclined surfaces, respectively. As shown in the figure, the droplets of water (blue, red and yellow color) and oil (transparent) maintain their initial positions on the spots when tilted in the perpendicular direction at an angle of 60° . Following this observation, an anisotropic line-tracing railroad was designed (Figure 4-14(d)), in

such a way that the two droplets of water (red and yellow dyes) with a small distance of 1 mm were slowly moving along the track on a 4-inch silicon wafer at the speed of 1.3 and 1 mm/s, respectively, without any collision and mixing. The insets show several sequential snapshots of the sliding droplets along the guided railroad. Such an anisotropic sliding surface would be useful for a droplet-based PCR in an open-channel format.

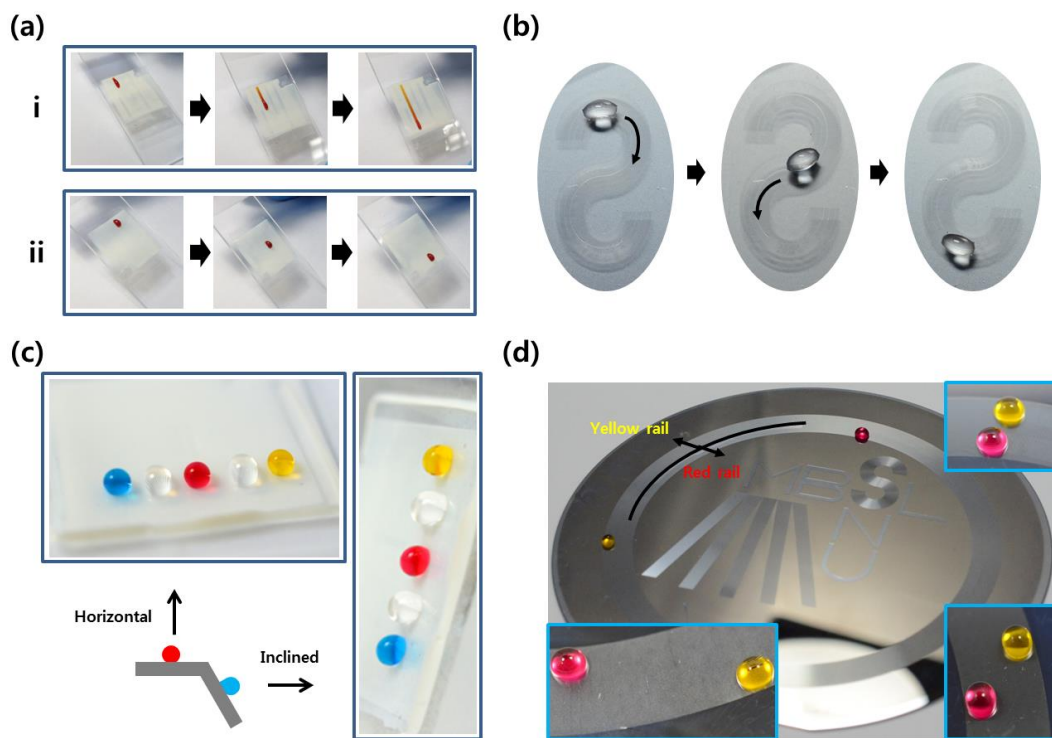


Figure 4-14. (a) Surface sliding of photoresist (AZ 1512) on (i) rice leaf-like prism arrays and (ii) overhang line arrays. (b) Curved line tracing of mineral oil on the S-shaped overhang structure. The arrows indicate the direction of oil sliding. (c) Droplet images of DI water (blue, red, and yellow) and mineral oil (transparent) on the horizontal and inclined surfaces (tilting angle = 60°). (d) Anisotropic liquid sliding railroad where each DI water droplet (red and yellow) smoothly slides along the path without any collision or mixing.

4-4. Summary

In this chapter, we have presented a simple fabrication method and design rules to make anisotropic omniphobic sliding surfaces. Various single- and dual-scale microgroove structures were prepared with different entry shapes such as prism, rectangle, and overhang by using UVO etching on replica-molded, UV-cured polymer resins mixed with Al_2O_3 nanoparticles. It turned out that negatively sloped, overhang microgrooves have ability to repel the wetting of various liquids from water to mineral oil and to guide spontaneous sliding of an oil droplet on a tilted substrate. Also, it was demonstrated that a different design rule would be needed to prepare an oil sliding surface, as judged by the observation that a nanoroughness did not yield a larger CA and a smaller SA as seen from the well-known lotus effect. It is envisioned that the current directional oil sliding surfaces would find many uses in various oil-related applications such as microfluidics, precision industry, and oil recovery.

Chapter 5. Robust, Flexible Anti-Reflection and Self-Cleaning Surfaces with Hierarchical Pyramidal Arrays for Efficiency Enhancement of Perovskite Solar Cells

Published in Journal of Materials Chemistry A, 2014, 2, 20017–20021

5-1. Introduction

Since the first report on the solid-state perovskite solar cell with a power conversion efficiency (PCE) of 9.7% in 2012,[72] researches on perovskite solar cell have been triggered. As a result, PCEs of 15% were reported in 2013,[73, 74] which was surpassed to more than 19% in 2014. [75] The PCE of 17.9% is highest among the certification values. Perovskite solar cell based on organometal halide has the potential for further improvement in PCE. [76, 77] Despite superb photovoltaic performance from the organometal halide perovskite materials, there are open issues to be addressed such as stability and toxicity. [78] One of critical issues is that $\text{CH}_3\text{NH}_3\text{PbI}_3$ is very soluble in water and even in low humidity condition. Moreover $\text{CH}_3\text{NH}_3\text{PbI}_3$ in contact with water can convert to PbI_2 that is moderately water-soluble and whose use is banned in many countries. Thus protection of $\text{CH}_3\text{NH}_3\text{PbI}_3$ from water is important in terms of stability and environmental concern.

Anti-reflection (AR) and self-cleaning (SC) surfaces have been studied theoretically[79-82] and experimentally[53, 83-86] to develop high efficiency solar cells with self-cleaning ability. AR and SC technologies are of importance in terms of harvesting light more efficiently because of minimizing the absorption loss by reflection and shade. In general, moth-eye inspired nano structures such as nanocone,[82, 87] nanopillar,[88, 89] nanopore[90, 91] or nanodorm structures[92] have been employed to reduce absorption loss by enhancing structural AR effect. These nanotextured surfaces which have submicron structures with compact spacing ratio have demonstrated appealing performance on light trapping effect. Despite the above significant AR effect, however, simple nano-structured AR films are not sufficient for the SC property requiring high static contact angle (CA) ($> \sim 150^\circ$) and low roll-off angle (ROA) ($< \sim 10^\circ$) with long term stability. It is well established that the simple nano-structured surfaces are not capable of possessing low ROAs surfaces according to the Wenzel and Cassie-Baxter models. [53] Besides, in terms of fabrication process, there have been extensive efforts to make an anti-reflective self-cleaning structure by using conventional fabrication techniques such as electrochemical wet etching,[93] photolithography,[94, 95] electron-beam lithography, [93] nanosphere lithography,[96, 97] and self-assembly approaching. [90] However, with these methods, the widespread use for perovskite solar cells has been limited in that they are time-consuming and high-cost processes for mass production. Moreover,

the additional heat and UV curing procedures of these methods could deteriorate the performance of perovskite solar cells.

In this chapter, we report a water-repellent perovskite solar cell based on the robust and flexible polydimethylsiloxane (PDMS) films with lotus leaf-inspired dual-scale hierarchical pyramidal arrays having bifunctional roles of anti-reflection and self-cleaning. Notably, we demonstrate not only AR effect by utilizing a micro pyramid structure but robust SC property with high CA ($\sim 157^\circ$) and low ROA ($\sim 7^\circ$) by creating hierarchical nano wrinkles on the pyramidal arrays. We fabricated the dual-roughness pyramidal structures by utilizing simple soft micromolding lithography and Ar ion surface treatment, which is a geometry-controllable, low-expertise and cost-effective route for practical applications. [89, 98] It was found that the light harvesting effect and the external protection from dust particles of perovskite solar cell devices were substantially improved as evidenced by photovoltaic and water-repellent experiments with the fabricated hierarchical pyramidal structures.

5-2. Experimental

5-2-1. Fabrication of pyramid-shaped anti-reflection and self-cleaning PDMS films

The schematic of fabrication process is shown in Figure 5-1, which comprises the PDMS replica molding, the Ar ion treatment and the fabrication of perovskite solar cell device. The pyramid-shaped master used in this work was produced by mechanical cutting method. The procedure is described in detail elsewhere. [99] After the preparation of the pyramid-shaped masters, the UV-curable polyurethane-acrylate (PUA) prepolymer solution was drop-dispensed on the master and covered by a flexible polyethylene-terephthalate (PET) film (~50 μm thickness). Subsequently, the PUA was cured by UV exposure ($\lambda = 250$ to ~400 nm, intensity of ~100 W/cm^2 , Fusion Cure System, Minuta Tech, Korea) for a few tens of seconds and the inverse pyramid PUA replica on the PET film was demold from the master. After overnight curing (>12 h) of PET film mold, to ensure a rigidity of PUA structures, PDMS precursor (Sylgard 184 Silicon elastomer, Dow Corning) and curing agent with a 10:1 ratio by weight was poured on the negative pyramid PET film mold and was placed at 70 $^{\circ}\text{C}$ for 1 h. Then, the fully cured PDMS micro pyramid arrays with a dimension of 30- μm width and 15- μm height was gently peeled off from the PET film mold.

Sequentially, the PDMS replica is exposed to Ar ion plasma for a few tens of seconds to form nano-wrinkles on the micro pyramid arrays by varying stiffness of a PDMS surface. [100, 101] Ar ion irradiation on a PDMS surface leads to the generation of a thin elastic crust layer on the top of the PDMS surface. Due to the higher stiffness (~ 100 times) of the thin crust atop than PDMS under layer, compressive stress is induced on the PDMS surface which in turn creates nano-wrinkles, whereas no wrinkled surface is formed without Ar treatment as shown in Figure 5-2. To make the dual-scale hierarchical pyramid (H.P.) PDMS arrays with enhanced superhydrophobicity, chemical deposition is conducted on the surface by using octafluorocyclobutane (C_4F_8) gas which is contained with Ar ion plasma in an inductively coupled plasma (ICP) etching system. The fabricated H.P. PDMS film is smoothly attached on the glass side (front side) of perovskite solar cell device without covering other adhesives owing to the strong van der Waal force between PDMS and bare glass.

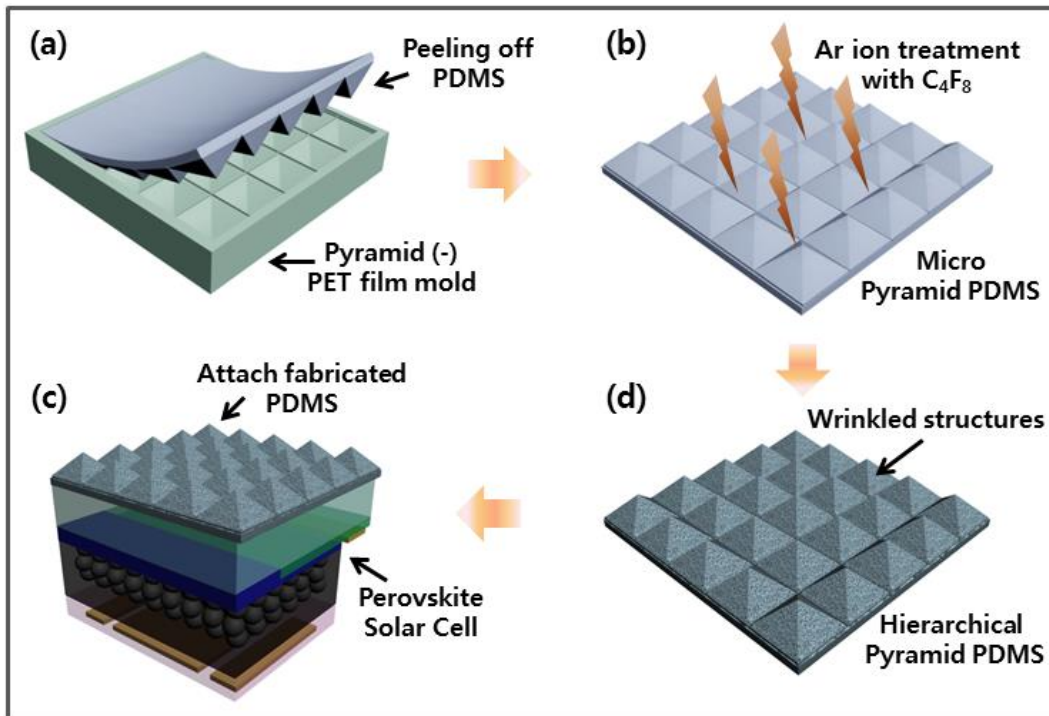


Figure 5-1. Fabrication scheme of dual-scale hierarchical pyramid (H.P.) PDMS arrays and perovskite solar cell device with the H.P. PDMS film on the glass-side.

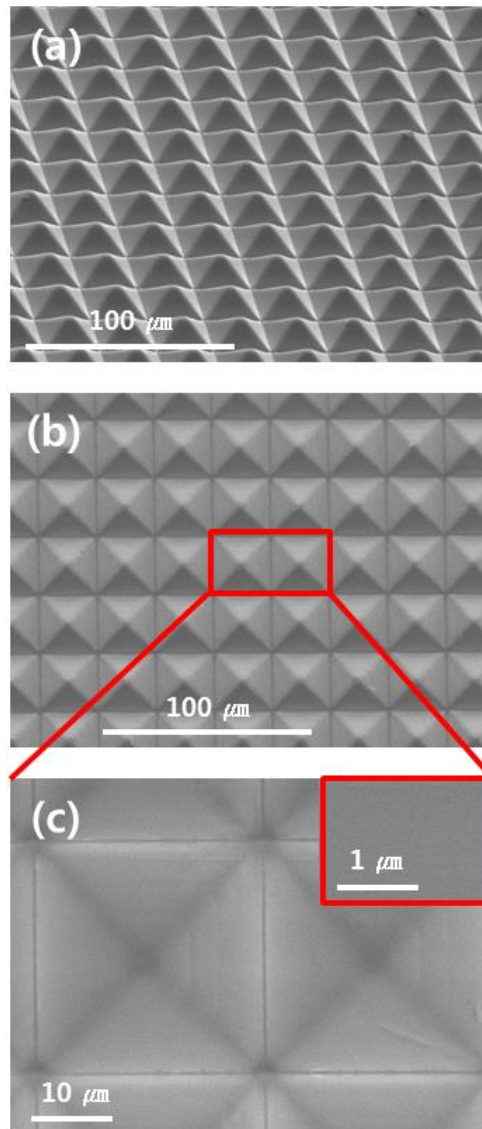


Figure 5-2. (a-c) SEM images of micro pyramidal arrays before Ar ion treatment.

5-2-2. Preparation of perovskite solar cells

The fluorine-doped tin oxide-coated (FTO) glass substrate was purchased from Pilkington (TEC-8, $8\Omega/\text{sq}$) and cleaned sequentially using UVO treatment for 15 min and sonication process with detergent liquid, acetone, ethanol and DI water. A compact blocking layer TiO_2 was deposited by spin-coating titanium diisopropoxide di(acetylacetonate) (Sigma-Aldrich, 75 wt% in isopropanol) 0.15 M in 1-butanol (Sigma-Aldrich, 99.8%) solution at 2000 rpm for 40 sec and sintered at $125\text{ }^\circ\text{C}$ for 5 min. Mesoporous 50-nm sized TiO_2 nanoparticles layer was formed on the TiO_2 blocking layer using TiO_2 paste, which consist of TiO_2 precursor, terpineol, ethylcellulose and lauric acid with a nominal ratio of 1.25: 6 : 0.9 : 0.3 wt%. To deposite on the substrate in liquid phase, 1.4 g of synthesized TiO_2 paste was diluted in 10 mL ethanol. The diluted TiO_2 paste solution was spin coated on the TiO_2 blocking layer at 2000 rpm for 20 s and annealed at 550 for 1h. After UVO treatment for 30 min, the substrate was immersed in titanium chloride solution (TiCl_4 , Sigma-Aldrich, > 98 %) 20 mM in DI water at $90\text{ }^\circ\text{C}$ for 10 min in water bath, followed by washing with DI water and sintered at $500\text{ }^\circ\text{C}$ for 30 min. The $\text{CH}_3\text{NH}_3\text{PbI}_3$ perovskite active layer was deposited on the mesoporous TiO_2 layer by using two-step process. First, 1 M (1.844 g) of PbI_2 (Sigma-Aldrich, 99 %) in 4 mL of N,N-dimethylformamide (DMF, Sigma–Aldrich, 99.8%) was spin-coated on the substrate at 6000 rpm for 20 s and dried sequentially at $40\text{ }^\circ\text{C}$

for 3 min and 100 °C for 10 min. Second, 0.3 g of the home-made methylammonium iodide[102] in 30 mL of 2-propanol (Sigma–Aldrich, 99.5%) was spun on the substrate at 3000 rpm for 20 sec and the same drying process with previous step was carried out. After washing with pure 2-propanol to remove unreacted perovskite residue, the hole transport material (HTM) was deposited on the substrate by spin coating a 72.3 mg of spiro-MeOTAD solution in 1 ml Chlorobenzene with 28.8 µL of 4-tertbutyl pyridine and 17.5 µL of lithium bis(trifluoromethanesulfonyl) imide solution of 520 mg Li-TSFI in 1 ml acetonitrile (Sigma–Aldrich, 99.8 %) at 4000 rpm for 20 s. For the counter electrode, gold (Au) was thermally deposited on the top of the HTM by evaporation under $\sim 10^{-6}$ Torr vacuum condition through a shadow mask.

5-2-3. Characterization

The morphologies of the fabricated hierarchical pyramid PDMS surfaces were examined by using high-resolution scanning electron microscope (SEM, HITACHI S-48000, Japan) at 5 kV. A 20 nm-thick platinum (Pt) layer was deposited on the surfaces to avoid charging effect. The chemical components of the PDMS surfaces were detected by energy dispersive spectroscopy (EDS, JSM-7600F, JEOL KOREA). The transmittance and reflectance were measured by using UV/Vis spectrometer (PerkinElmer Lambda 45, USA) in the range from 300

to 800 nm. Current-voltage characteristics of perovskite solar cells were measured under AM 1.5G one sun illumination (100 mW/cm^2) using a solar simulator (Oriel Sol 3A class AAA) equipped with a Keithley 2400 source meter and a 450 W Xenon lamp (Newport 6279NS). External quantum efficiency (EQE) was collected using IPCE system (PV measurement Inc.) equipped with a 75 W Xenon lamp (USHIO, Japan). The static CAs and ROAs of DI water on the fabricated PDMS films were measured by a contact angle analyzer (Drop Shape Analysis System DSA100, Kruss, Germany). To capture the optical images of CAs, a droplet of DI water ($\sim 5 \text{ }\mu\text{L}$) was gently placed onto the surfaces. The ROAs were measured by tilting the substrate until the droplet start to rolling-off on the surfaces.

5-3. Results and Discussion

5-3-1. The structure of fabricated PDMS film and perovskite solar cell device

SEM images of the fabricated bifunctional micro/nano-wrinkled pyramid arrays are shown in Figure 5-3. It is demonstrated that the structures have well-defined shapes with high structural fidelity and integrity. Figure 5-3(c) exhibits the magnified SEM images of the H.P. PDMS structure, where the inset clearly shows the formation of nano-wrinkles on the PDMS surface.

We have examined AR and SC effects of the H.P. PDMS film by using perovskite solar cell. The structure of perovskite solar cell is schematically illustrated in Figure 5-4(a). Perovskite solar cell is composed of a thin TiO_2 layer as a blocking layer (bl- TiO_2), a mesoporous TiO_2 (mp- TiO_2) layer, a $\text{CH}_3\text{NH}_3\text{PbI}_3$ perovskite film deposited on the mp- TiO_2 layer by two-step process, a spiro-MeOTAD hole transporting layer (HTM), and a gold electrode. Detailed fabrication sequence and a real device is shown in Figure 5-4(c). In the focused ion beam assisted cross-sectional SEM image (see Figure 5-4(b)), each layer is distinctly shown and the pores of mp- TiO_2 layer are fully infiltrated with the perovskite. It is clearly seen that the perovskite capping layer is formed on top of the mp- TiO_2 layer and induces heterojunction with the organic HTM layer.

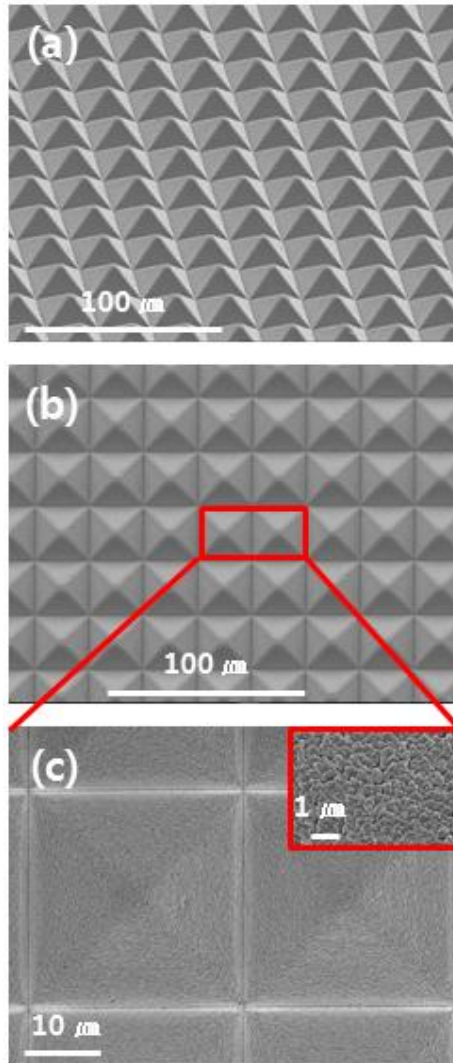


Figure 5-3. (a-c) SEM images for H.P. structures with different magnifications and view angles. The inset clearly shows the nano-wrinkled roughness on the fabricated micro pyramid arrays after Ar ion treatment. There are no significant structural different between micro pyramidal arrays and H.P. structures (see Figure 5-2), but roughness of pyramid surface as shown in inset image of (c).

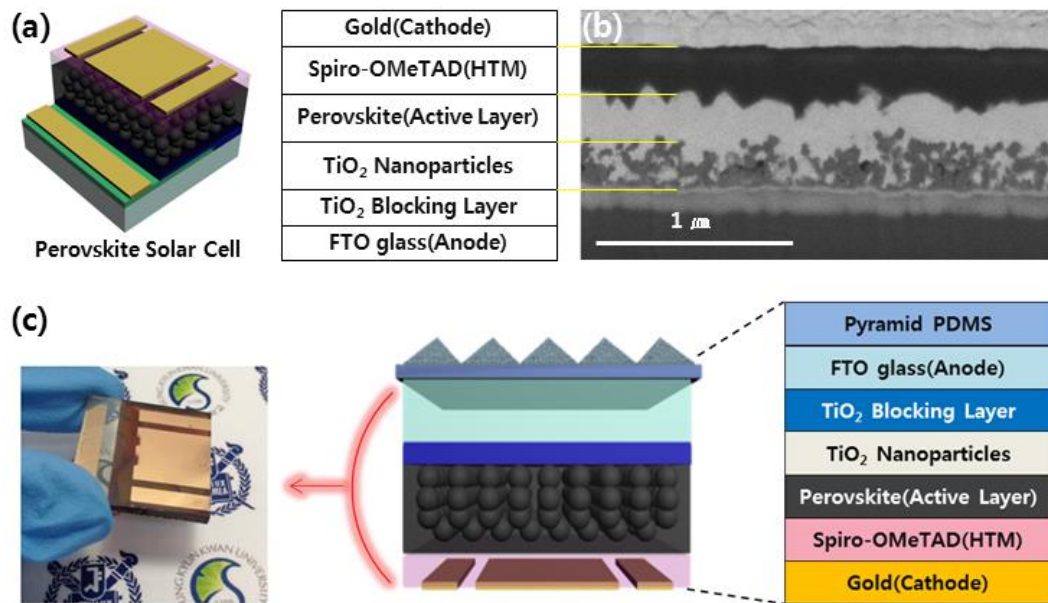


Figure 5-4. (a) Schematic illustration for structure of perovskite solar cell and (b) focused ion beam assisted cross-sectional SEM image of the perovskite solar cell with two-step deposition process. mp-TiO₂ and bl-TiO₂ represent mesoporous TiO₂ and blocking layer TiO₂, respectively. (c) The photograph and schematics of fabricated perovskite solar cells device with multi-functional H.P. PDMS film.

5-3-2. Anti-reflection effect of the fabricated H.P. PDMS film

We have investigated the transmittance and reflectance of the fabricated H.P. PDMS film to characterize optical property of the pyramidal structures. Figure 5-5 show the transmittance and reflectance spectra of three different samples including a bare FTO glass, a FTO glass with flat PDMS and a FTO glass with H.P. PDMS. Note that both of the ‘with flat PDMS’ and ‘with H.P. PDMS’ are attached on the bare FTO glass. The laminated surface of a FTO glass with a fabricated thin and flexible H.P. PDMS film is shown as inset photograph in Figure 5-5(a). The average transmittance of a bare FTO glass is ~76% in the wavelength range from 350 to 800 nm, which is insignificantly increased to ~77% with a flat PDMS film on the FTO glass. On the contrary, the FTO glass with the H.P. PDMS film shows substantially an improved transmittance over ~80%, which is indicative of strong anti-reflection effect. In the same manner, the average reflectance of the H.P. PDMS film on the FTO glass is ~5.2%, which is much lower than those of the bare FTO glass (~8.6%) and with a flat PDMS film (~ 6.8%).

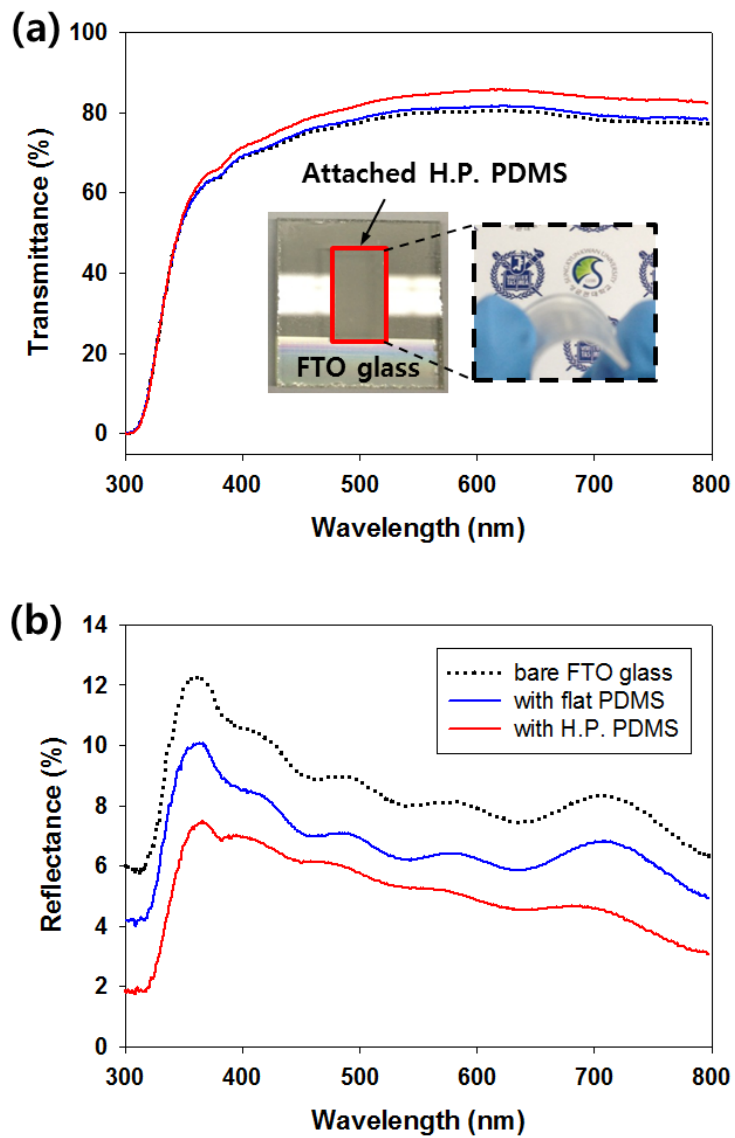


Figure 5-5. Transmittance (a) and reflectance spectra (b) of FTO glass with three different cases, bare FTO, flat PDMS and H.P. PDMS. The inset photographs represent the fabricated flexible H.P. PDMS film attached on a FTO glass showing visual effect of anti-reflection.

5-3-3. Analysis of the optical property of H.P. PDMS film

In previous work, *Chapter 3*, we demonstrated flexible and transparent superomniphobic polymeric surface with mushroom-like micropillar arrays. Similar to H.P. PDMS film in this work, the mushroom-shaped surface was fabricated by using PDMS replication method. In addition, the superomniphobic surface could repellent liquid with a wide range of surface tension, which property also included self-cleaning effect (not only DI water but various liquids). However, the optical property of mushroom-like micropillar arrays could be lower than that of pyramidal structures. Due to the wide and flat tip of mushroom-like micropillar, it is disturbed that the direction of incident light to penetrate perpendicular to the surface. On the other hand, the H.P. PDMS film has structural anti-reflection effect with light harvesting property. The compared properties with mushroom-shaped arrays and H.P. structures are illustrated in Figure 5-6. In this regard, we prepared H.P. PDMS film to enhance efficiency of solar cell device using following structural optical advantages.

First, the observed increase in anti-reflection effect of the fabricated H.P. PDMS film results from a relatively low refractive index (n) of the PDMS ($n \sim 1.43$), which is intermediate material between air ($n \sim 1$) and the FTO glass substrate ($n \sim 1.53$) as shown in Figure 5-7(b). In this reason, the interfacial Fresnel's reflectance coefficient is expected to be decreased by attaching the

PDMS film on the FTO glass, which causes the graded refractive index distribution of medium along light path (see Figure 5-7(c-d)). [103, 104] The Fresnel's reflectance coefficient R is briefly defined as,

$$R = \left(\frac{n_2 - n_1}{n_2 + n_1} \right)^2$$

where n_1 and n_2 represent the refractive index of transmitting medium and incident substrate, respectively. It is noted that the value of R is higher at the interface between air and glass ($R_{ag} \sim 4.3\%$) than those of between air and PDMS ($R_{ap} \sim 3.1\%$). The reflected light at the interface between PDMS and glass will be disregarded owing to the relatively small value of $R_{pg} \sim 0.1\%$. It follows that the intermediate PDMS material ensures a lower reflection at the FTO glass substrate. In addition, there is a structural double reflection effect of pyramidal structures as shown in Figure 5-7(b). The detailed morphologies of the fabricated anti-reflection PDMS surface are represented in Figure 5-7(a), in which pyramid arrays are shown in shape of isosceles triangle with 45° angle of bottom edge side. Figure 5-7(b) demonstrates the dynamics of incident light schematically, assuming that the direction of incident light is perpendicular to the surface of substrate. The optical advantage of this pyramidal structure is that the first reflected light at front surface heads for other adjacent one again. Also, the second transmitting light into pyramidal PDMS is totally reflected in the interface between air and PDMS surface. Light trapping effect in the H.P. PDMS surface induced by such a process of double reflection mechanism enhances transmittance

and reduces reflectance of the FTO glass.

The Snell's law is given as follows,

$$n_1 \sin \theta_1 = n_2 \sin \theta_2$$

where n_1 and n_2 are the refractive indices of transmitting medium (air) and incident substrate (PDMS), θ_1 and θ_2 are the incidence and refraction angle of light, respectively. As illustrated in Figure 5-8, θ_3 and θ_4 occur at second reflection surface by double reflection effect. According to the above equation, the value of θ_2 is defined as 30° with assumption that the direction of incident light is perpendicular to the PDMS surface of substrate, $n_1 \sim 1$, $n_2 \sim 1.43$ and $\theta_1 \sim 45^\circ$. Sequentially, at second reflection surface the equation is summarized as,

$$\frac{\sqrt{6}}{2} = \sin \theta_4$$

so, $\theta_4 > 1$, which means that the second transmitting light into PDMS is totally reflected in the interface between air and pyramidal PDMS. In this case, the second reflective light is the only reflection light of the incident light at the interface between air and PDMS (see also Figure 5-7(b)). Also, the Fresnel's reflectance coefficient R is described as, in detail,

$$R(\text{reflectance coefficient}) = \frac{|r_s|^2 + |r_p|^2}{2}$$

$$r_s = \frac{n_1 \cos \theta_1 - n_2 \cos \theta_2}{n_1 \cos \theta_1 + n_2 \cos \theta_2}$$

$$r_p = \frac{n_2 \cos \theta_1 - n_1 \cos \theta_2}{n_1 \cos \theta_2 + n_2 \cos \theta_1}$$

where, r is the ratio of the reflective light amplitude to that of the incident light. The subscript s and p mean s-polarized and p-polarized light, respectively. It is noted that the calculated reflection coefficient of first reflection, R is ~3.94% based on the value of r_s ~0.27 and r_p ~0.077. Finally, the value R of total reflected light is estimated to be about 0.16% by the double reflection effect on the substrate.

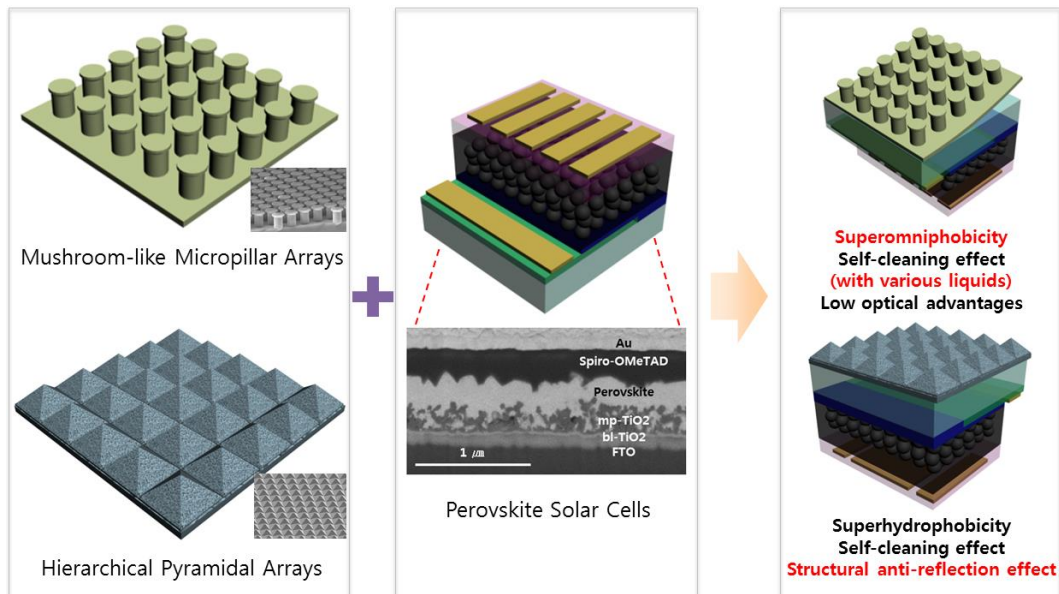


Figure 5-6. Self-cleaning and optical properties of two different micro structures. Superomniphobicity and low optical advantages of mushroom-like micropillar arrays. Superhydrophobicity and structural anti-reflection effect of H.P. PDMS film.

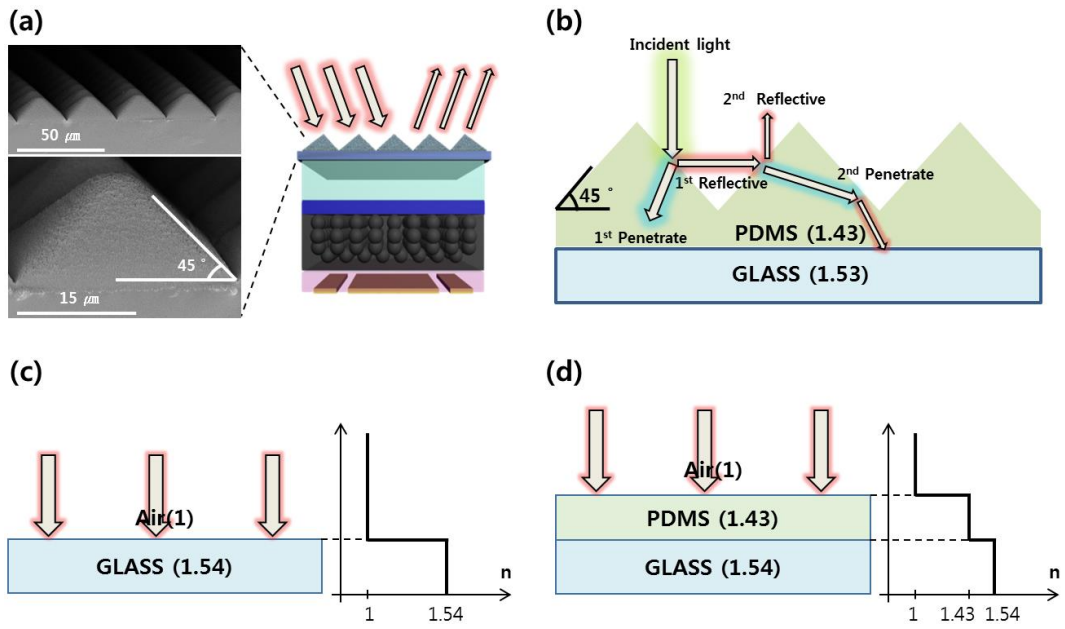


Figure 5-7. (a) SEM images of the H.P. arrays with 45° angle of bottom edge side. The H.P. PDMS film serves as anti-reflection layer on the perovskite solar cell device. (b) Theoretical scheme of anti-reflection mechanism on the H.P. PDMS film. The size and color of arrows indicate relative magnitude and direction of each light. (c-d) Refractive index profiles of the bare FTO glass and the FTO glass with a flat PDMS layer.

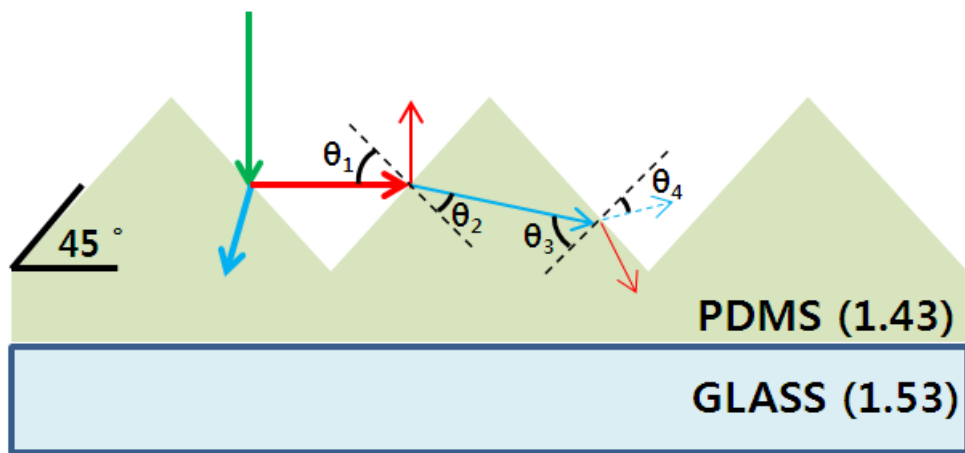


Figure 5-8. The path of the incident light (green) with reflection (red) and transmission (blue) between air and pyramid PDMS surfaces. The length and width of arrows roughly indicate the direction and intensity of each path way. Parentheses represent refractive indices.

5-3-4. Performances of perovskite solar cell device with H.P. PDMS film

Figure 5-9 compares current density-voltage curves and EQE spectra with and without the H.P. PDMS film on the perovskite solar cell. The photovoltaic parameters of perovskite solar cells with and without the H.P. PDMS film are listed in Table 5-1. Since our H.P. PDMS film can be easily attached on or detached from FTO glass, same device is used to measure the current-voltage curves and EQE spectra of both ‘bare FTO glass’ and ‘with H.P. PDMS’ samples in Figure 5-9 to ensure that the performance improvement of perovskite solar cell results from the H.P. PDMS film. The short-circuit photocurrent density (J_{sc}) is increased from 19.34 to 20.87 mA/cm² after covering the FTO surface with the H.P. PDMS film, which results in increase in PCE from 13.12% to 14.01%, corresponding to 6.8% increment. The open-circuit voltage (V_{oc}) and fill factor (FF) are hardly changed, which implies that the improved PCE is mainly due to the anti-reflection effect from the H.P. structure. The anti-reflection effect contributes to the entire wavelength range as shown in EQE spectra in Figure 5-9(b), which proves that the H.P. PDMS film is effective in harnessing visible light. Integrated J_{sc} s from EQE are calculated to be 15.95 mA/cm² for ‘bare FTO’ and 16.49 mA/cm² for ‘with H.P. PDMS’ sample, respectively. The mismatch of the integrated J_{sc} s from EQE and the J_{sc} s from IV measurements is probably related to

charge collection rate slower than detection limit in the given EQE setup. [105,
106]

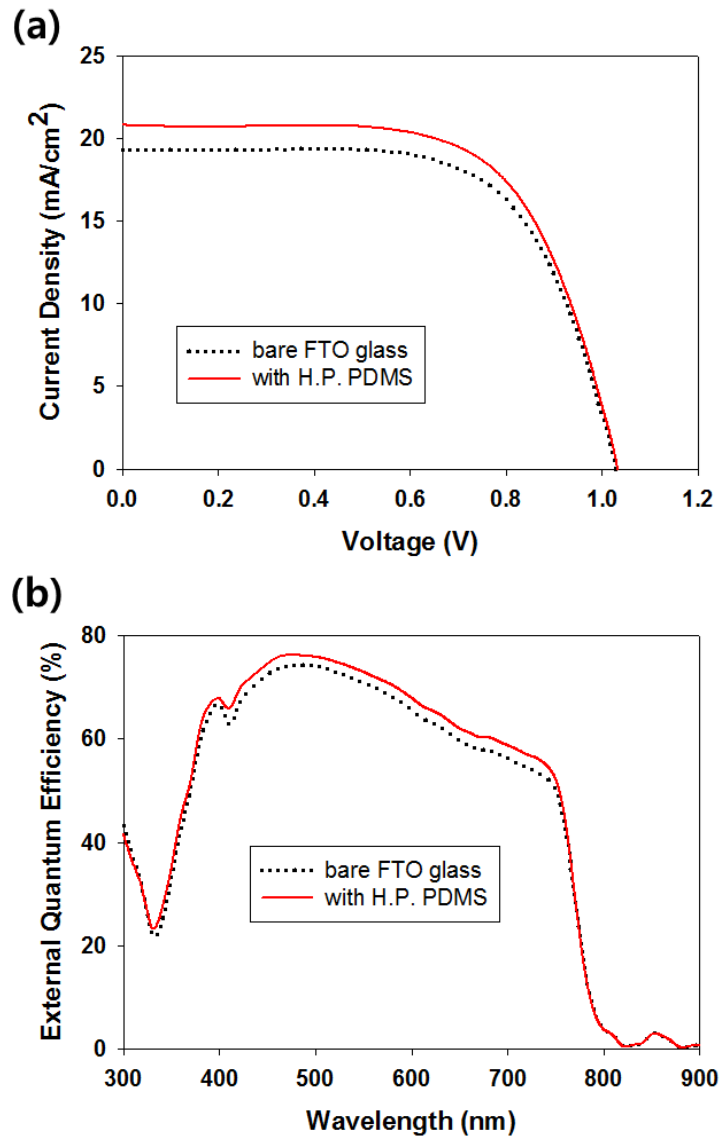


Figure 5-9. (a) Current density-voltage curves and (b) EQE of perovskite solar cell devices with and without (bare FTO) the H.P. PDMS film.

Device	J_{sc} (mA/cm ²)	V_{oc} (V)	FF	PCE (%)
Bare FTO	19.34	1.028	0.66	13.12
With H.P PDMS	20.87	1.033	0.65	14.01

Table 5-1. Short-circuit photocurrent density (J_{sc}), open-circuit voltage (V_{oc}), fill factor (FF), and power conversion efficiency (PCE) of the perovskite solar cells with and without the H.P. PDMS film. The data were collected under AM 1.5G one sun illumination (100 mW/cm²).

5-3-5. Superhydrophobicity and Self-cleaning effect of the fabricated H.P. PDMS film

In addition to anti-reflection effect, we further demonstrate the self-cleaning property of the H.P. PDMS film. In the outdoor environment, the harmful dust particles or rain drop could have ill influence on the performance of perovskite solar cell. Futhermore, protection from water is important to keep long-term stability of perovskite solar cell. The CAs and ROAs of DI water (volume of 5 μ L) on the H.P. PDMS film are compared those of the bare FTO and the flat PDMS in Figure 5-10(a). The H.P. PDMS film demonstrates extremely high CA of 157° and low ROA of 7° , which is indicative of superhydrophobicity. The flat PDMS film shows CA of 109° higher than the bare FTO glass (CA = 48°), however, its ROA of 90° is similar to the bare FTO glass, which means that the droplet would not roll off on the surfaces for all the tested tilting angle of the substrates. The inset images show the droplet shapes placed on the each surfaces. We have also tested the long-term stability of the superhydrophobic H.P. PDMS film under ambient condition over a time period of 1 month (see Figure 5-10(b)). The robustness of superhydrophobic characteristics using the H.P. PDMS are demonstrated without any noticeable changes or degradations. The inset photograph shows the different CAs of several water droplets (coloured with red dye to demonstrate visually) on a perovskite solar cell, where a part is attached

with the H.P. PDMS film. These superhydrophobicity of the fabricated H.P. PDMS surfaces leads to without doubt self-cleaning effect. The self-cleaning process is schematically illustrated in Figure 5-11(a), where the dust particles can be easily removed by rolling off a water droplet across the surface. The self-cleaning of dust is important in keeping the performance of solar cell or module constant because contamination on solar panels by dust particles or dirty water would block sunlight and consequently degrade the photovoltaic performance. The self-cleaning abilities with and without H.P. PDMS on the perovskite solar cell are shown in Figure 5-11(b). In contrast to the wetted flow on the perovskite solar cell without the H.P. PDMS film (i), the DI droplets easily and quickly rolled-off with the dust particles on the H.P. PDMS patterned surface, which demonstrated the self-cleaning behavior (ii). This self-cleaning effect renders the perovskite solar cell water-repellent.

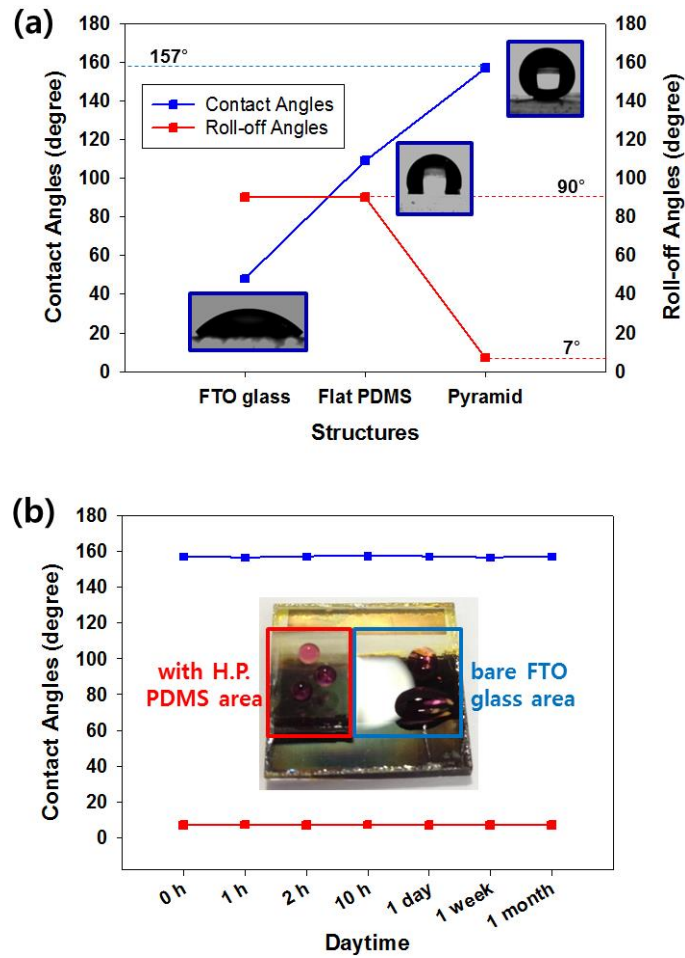


Figure 5-10. (a) Static CAs (green line) and ROAs (blue line) of de-ionized (DI) water on the three different surfaces. Microscope images of a droplet on the each surface are shown in the insets. (b) Time-dependent CA and ROA of the H.P. PDMS film measured over a time period of one month. Inset photograph shows the degree of reflectivity and superhydrophobicity for the different areas with and without a H.P. PDMS film on the same perovskite solar cell. Water was coloured with red dye to demonstrate visually.

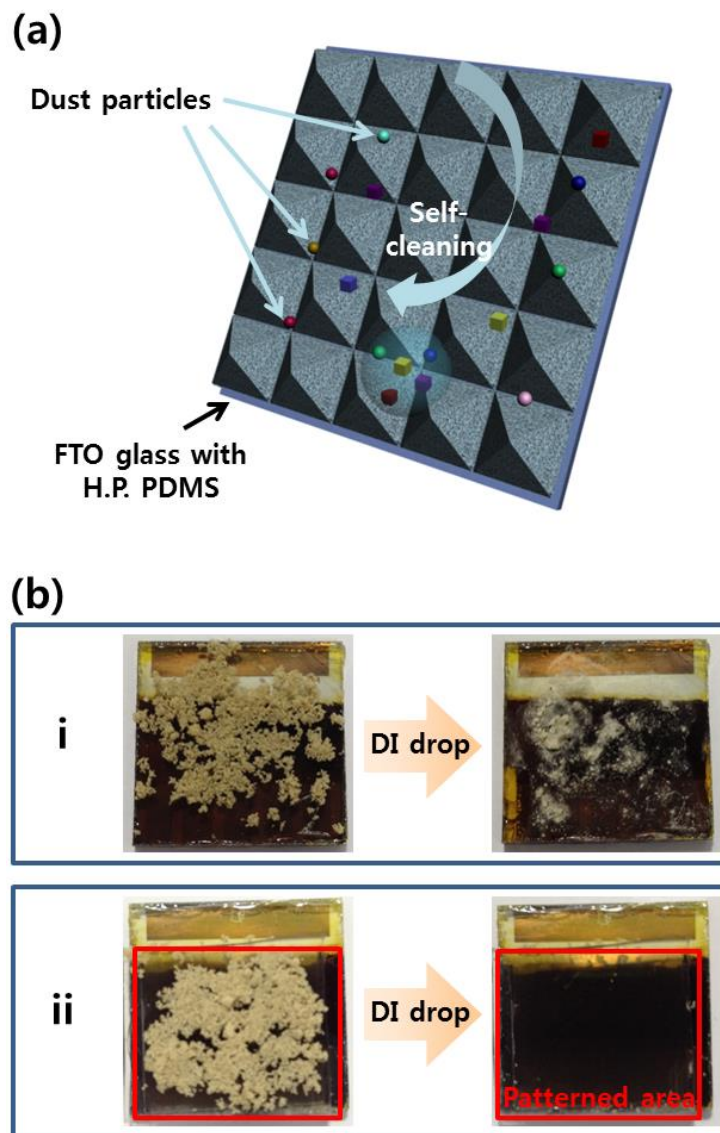


Figure 5-11. (a) Schematic illustration of self-cleaning effect on the H.P. PDMS surface. (b) Self-cleaning experiments for the perovskite solar cell devices without (i) and with (ii) the H.P. PDMS film.

5-4. Summary

In this study, we presented a robust and flexible anti-reflection film with enhanced self-cleaning ability using hierarchical pyramidal arrays with wrinkled surfaces for water-repellent perovskite solar cell. The hierarchical pyramidal PDMS film with bifunctionality was successfully fabricated by micromolding and Ar ion surface treatment, which was found to be easily attached to the bare FTO glass surface without any additional adhesives. It turned out that the hierarchical pyramidal PDMS film enhanced photocurrent due to the anti-reflection property for visible light and demonstrated excellent self-cleaning behavior due to superhydrophobicity. Such bifunctional property is highly beneficial to solar cell applications, especially in areas requiring water-repellent condition like perovskite solar cell.

References

- [1] B. Bhushan, "Biomimetics: lessons from nature - an overview," *Philosophical Transactions of the Royal Society a-Mathematical Physical and Engineering Sciences*, vol. 367, pp. 1445-1486, 2009.
- [2] Z. G. Guo, W. M. Liu, and B. L. Su, "Superhydrophobic surfaces: From natural to biomimetic to functional," *Journal of Colloid and Interface Science*, vol. 353, pp. 335-355, 2011.
- [3] A. Jagota and C. Y. Hui, "Adhesion, friction, and compliance of bio-mimetic and bio-inspired structured interfaces," *Materials Science & Engineering R-Reports*, vol. 72, pp. 253-292, 2011.
- [4] L. H. Shu, K. Ueda, I. Chiu, and H. Cheong, "Biologically inspired design," *Cirp Annals-Manufacturing Technology*, vol. 60, pp. 673-693, 2011.
- [5] W. G. Bae, H. N. Kim, D. Kim, S. H. Park, H. E. Jeong, and K. Y. Suh, "25th Anniversary Article: Scalable Multiscale Patterned Structures Inspired by Nature: the Role of Hierarchy," *Advanced Materials*, vol. 26, pp. 675-699, 2014.
- [6] P. Ball, "Engineering - Shark skin and other solutions," *Nature*, vol. 400, pp. 507-509, 1999.
- [7] R. Blossey, "Self-cleaning surfaces - virtual realities," *Nature Materials*, vol. 2, pp. 301-306, 2003.
- [8] P. B. Clapham and M. C. Hutley, "Reduction of Lens Reflection by Moth Eye Principle," *Nature*, vol. 244, pp. 281-282, 1973.
- [9] H. E. Jeong, J. K. Lee, H. N. Kim, S. H. Moon, and K. Y. Suh, "A nontransferring dry adhesive with hierarchical polymer nanohairs," *Proceedings of the National Academy of Sciences of the United States of America*, vol. 106, pp. 5639-5644, 2009.
- [10] B. Bhushan and Y. C. Jung, "Natural and biomimetic artificial surfaces for superhydrophobicity, self-cleaning, low adhesion, and drag reduction,"

- Progress in Materials Science*, vol. 56, pp. 1-108, 2011.
- [11] A. B. D. Cassie and S. Baxter, "Wettability of porous surfaces.," *Transactions of the Faraday Society*, vol. 40, pp. 0546-0550, 1944.
- [12] R. N. Wenzel, "Resistance of solid surfaces to wetting by water," *Industrial and Engineering Chemistry*, vol. 28, pp. 988-994, 1936.
- [13] A. Tuteja, W. Choi, M. L. Ma, J. M. Mabry, S. A. Mazzella, G. C. Rutledge, G. H. McKinley and R. E. Cohen, "Designing superoleophobic surfaces," *Science*, vol. 318, pp. 1618-1622, 2007.
- [14] A. Tuteja, W. Choi, J. M. Mabry, G. H. McKinley, and R. E. Cohen, "Robust omniphobic surfaces," *Proceedings of the National Academy of Sciences of the United States of America*, vol. 105, pp. 18200-18205, 2008.
- [15] R. Kwak, H. E. Jeong, and K. Y. Suh, "Fabrication of Monolithic Bridge Structures by Vacuum-Assisted Capillary-Force Lithography," *Small*, vol. 5, pp. 790-794, 2009.
- [16] Z. H. Nie and E. Kumacheva, "Patterning surfaces with functional polymers," *Nature Materials*, vol. 7, pp. 277-290, 2008.
- [17] Y. N. Xia and G. M. Whitesides, "Soft lithography," *Angewandte Chemie-International Edition*, vol. 37, pp. 550-575, 1998.
- [18] D. M. Cannon, T. C. Kuo, P. W. Bohn, and J. V. Sweedler, "Nanocapillary array interconnects for gated analyte injections and electrophoretic separations in multilayer microfluidic architectures," *Analytical Chemistry*, vol. 75, pp. 2224-2230, 2003.
- [19] J. Y. Park, H. Y. Chae, C. H. Chung, S. J. Sim, J. Park, H. H. Lee and P. J. Yoo, "Controlled wavelength reduction in surface wrinkling of poly(dimethylsiloxane)," *Soft Matter*, vol. 6, pp. 677-684, 2010.
- [20] X. Deng, L. Mammen, H. J. Butt, and D. Vollmer, "Candle Soot as a Template for a Transparent Robust Superamphiphobic Coating," *Science*, vol. 335, pp. 67-70, 2012.
- [21] L. Feng, S. H. Li, Y. S. Li, H. J. Li, L. J. Zhang, J. Zhai, Y. Song, B. Liu, L. Jiang and D. Zhu, "Super-hydrophobic surfaces: From natural to artificial," *Advanced Materials*, vol. 14, pp. 1857-1860, 2002.

- [22] A. Lafuma and D. Quere, "Superhydrophobic states," *Nature Materials*, vol. 2, pp. 457-460, 2003.
- [23] S. Wang and L. Jiang, "Definition of superhydrophobic states," *Advanced Materials*, vol. 19, pp. 3423-3424, 2007.
- [24] L. J. Cheng, M. T. Kao, E. Meyhofer, and L. J. Guo, "Highly efficient guiding of microtubule transport with imprinted CYTOP nanotracks," *Small*, vol. 1, pp. 409-414, 2005.
- [25] S. Yang, K. Khare, and P. C. Lin, "Harnessing Surface Wrinkle Patterns in Soft Matter," *Advanced Functional Materials*, vol. 20, pp. 2550-2564, 2010.
- [26] W. Choi, A. Tuteja, S. Chhatre, J. M. Mabry, R. E. Cohen, and G. H. McKinley, "Fabrics with Tunable Oleophobicity," *Advanced Materials*, vol. 21, pp. 2190-2195, 2009.
- [27] X. J. Liu, W. C. Wu, X. L. Wang, Z. Z. Luo, Y. M. Liang, and F. Zhou, "A replication strategy for complex micro/nanostructures with superhydrophobicity and superoleophobicity and high contrast adhesion," *Soft Matter*, vol. 5, pp. 3097-3105, 2009.
- [28] H. Zhao, K. Y. Law, and V. Sambhy, "Fabrication, Surface Properties, and Origin of Superoleophobicity for a Model Textured Surface," *Langmuir*, vol. 27, pp. 5927-5935, 2011.
- [29] K. Ellinas, A. Tserepi, and E. Gogolides, "From Superamphiphobic to Amphiphilic Polymeric Surfaces with Ordered Hierarchical Roughness Fabricated with Colloidal Lithography and Plasma Nanotexturing," *Langmuir*, vol. 27, pp. 3960-3969, 2011.
- [30] M. Im, H. Im, J. H. Lee, J. B. Yoon, and Y. K. Choi, "A robust superhydrophobic and superoleophobic surface with inverse-trapezoidal microstructures on a large transparent flexible substrate," *Soft Matter*, vol. 6, pp. 1401-1404, 2010.
- [31] F. Xia and L. Jiang, "Bio-inspired, smart, multiscale interfacial materials," *Advanced Materials*, vol. 20, pp. 2842-2858, 2008.
- [32] X. Yao, J. Gao, Y. L. Song, and L. Jiang, "Superoleophobic Surfaces with

- Controllable Oil Adhesion and Their Application in Oil Transportation," *Advanced Functional Materials*, vol. 21, pp. 4270-4276, 2011.
- [33] A. K. Epstein, B. Pokroy, A. Seminara, and J. Aizenberg, "Bacterial biofilm shows persistent resistance to liquid wetting and gas penetration," *Proceedings of the National Academy of Sciences of the United States of America*, vol. 108, pp. 995-1000, 2011.
- [34] J. P. Zhang and S. Seeger, "Superoleophobic Coatings with Ultralow Sliding Angles Based on Silicone Nanofilaments," *Angewandte Chemie-International Edition*, vol. 50, pp. 6652-6656, 2011.
- [35] M. Im, H. Im, J. H. Lee, J. B. Yoon, and Y. K. Choi, "Analytical Modeling and Thermodynamic Analysis of Robust Superhydrophobic Surfaces with Inverse-Trapezoidal Microstructures," *Langmuir*, vol. 26, pp. 17389-17397, 2010.
- [36] A. Tuteja, W. Choi, G. H. McKinley, R. E. Cohen, and M. F. Rubner, "Design Parameters for Superhydrophobicity and Superoleophobicity (vol 33, pg 757, 2008)," *Mrs Bulletin*, vol. 33, pp. 996-996, 2008.
- [37] T. Verho, C. Bower, P. Andrew, S. Franssila, O. Ikkala, and R. H. A. Ras, "Mechanically Durable Superhydrophobic Surfaces," *Advanced Materials*, vol. 23, pp. 673-678, 2011.
- [38] S. Kim, E. Cheung, and M. Sitti, "Wet Self-Cleaning of Biologically Inspired Elastomer Mushroom Shaped Microfibrillar Adhesives," *Langmuir*, vol. 25, pp. 7196-7199, 2009.
- [39] M. K. Kwak, C. Pang, H. E. Jeong, H. N. Kim, H. Yoon, H. S. Jung and K. Y. Suh, "Towards the Next Level of Bioinspired Dry Adhesives: New Designs and Applications," *Advanced Functional Materials*, vol. 21, pp. 3606-3616, 2011.
- [40] J. Lee and R. S. Fearing, "Contact self-cleaning of synthetic gecko adhesive from polymer microfibers," *Langmuir*, vol. 24, pp. 10587-10591, 2008.
- [41] K. Kollias, H. Y. Wang, Y. Song, and M. Zou, "Production of a superhydrophilic surface by aluminum-induced crystallization of

- amorphous silicon," *Nanotechnology*, vol. 19, 2008.
- [42] N. Verplanck, E. Galopin, J. C. Camart, V. Thomy, Y. Coffinier, and R. Boukherroub, "Reversible electrowetting on superhydrophobic silicon nanowires," *Nano Letters*, vol. 7, pp. 813-817, 2007.
- [43] K. Y. Suh, S. J. Choi, S. J. Baek, T. W. Kim, and R. Langer, "Observation of high-aspect-ratio nanostructures using capillary lithography," *Advanced Materials*, vol. 17, pp. 560-564, 2005.
- [44] C. I. Park, H. E. Jeong, S. H. Lee, H. S. Cho, and K. Y. Suh, "Wetting transition and optimal design for microstructured surfaces with hydrophobic and hydrophilic materials," *Journal of Colloid and Interface Science*, vol. 336, pp. 298-303, 2009.
- [45] L. L. Cao, H. H. Hu, and D. Gao, "Design and fabrication of micro-textures for inducing a superhydrophobic behavior on hydrophilic materials," *Langmuir*, vol. 23, pp. 4310-4314, 2007.
- [46] M. Kim, K. Kim, N. Y. Lee, K. Shin, and Y. S. Kim, "A simple fabrication route to a highly transparent super-hydrophobic surface with a poly(dimethylsiloxane) coated flexible mold," *Chemical Communications*, pp. 2237-2239, 2007.
- [47] W. Choi, A. Tuteja, J. M. Mabry, R. E. Cohen, and G. H. McKinley, "A modified Cassie-Baxter relationship to explain contact angle hysteresis and anisotropy on non-wetting textured surfaces," *Journal of Colloid and Interface Science*, vol. 339, pp. 208-216, 2009.
- [48] R. Dufour, P. Brunet, M. Harnois, R. Boukherroub, V. Thomy, and V. Senez, "Zipping Effect on Omniphobic Surfaces for Controlled Deposition of Minute Amounts of Fluid or Colloids," *Small*, vol. 8, pp. 1229-1236, 2012.
- [49] A. Grigoryev, Y. Roiter, I. Tokarev, I. Luzinov, and S. Minko, "Colloidal Occlusion Template Method for Micromanufacturing of Omniphobic Surfaces," *Advanced Functional Materials*, vol. 23, pp. 870-877, 2013.
- [50] V. Liimatainen, V. Sariola, and Q. Zhou, "Controlling Liquid Spreading Using Microfabricated Undercut Edges," *Advanced Materials*, vol. 25, pp.

2275-2278, 2013.

- [51] J. D. Smith, R. Dhiman, S. Anand, E. Reza-Garduno, R. E. Cohen, G. H. McKinley and K. K. Varanasi, "Droplet mobility on lubricant-impregnated surfaces," *Soft Matter*, vol. 9, pp. 1772-1780, 2013.
- [52] T. S. Wong, S. H. Kang, S. K. Y. Tang, E. J. Smythe, B. D. Hatton, A. Grinthal and J. Aizenberg, "Bioinspired self-repairing slippery surfaces with pressure-stable omniphobicity," *Nature*, vol. 477, pp. 443-447, 2011.
- [53] S. M. Kang, S. M. Kim, H. N. Kim, M. K. Kwak, D. H. Tahk, and K. Y. Suh, "Robust superomniphobic surfaces with mushroom-like micropillar arrays," *Soft Matter*, vol. 8, pp. 8563-8568, 2012.
- [54] D. Wu, J. N. Wang, S. Z. Wu, Q. D. Chen, S. A. Zhao, H. Zhang, H. B. Sun and L. Jiang, "Three-Level Biomimetic Rice-Leaf Surfaces with Controllable Anisotropic Sliding," *Advanced Functional Materials*, vol. 21, pp. 2927-2932, 2011.
- [55] J. Wan, A. Bick, M. Sullivan, and H. A. Stone, "Controllable microfluidic production of microbubbles in water-in-oil emulsions and the formation of porous microparticles," *Advanced Materials*, vol. 20, pp. 3314-3318, 2008.
- [56] N. A. Malvadkar, M. J. Hancock, K. Sekeroglu, W. J. Dressick, and M. C. Demirel, "An engineered anisotropic nanofilm with unidirectional wetting properties," *Nature Materials*, vol. 9, pp. 1023-1028, 2010.
- [57] Y. M. Zheng, H. Bai, Z. B. Huang, X. L. Tian, F. Q. Nie, Y. Zhao, J. Zhai and L. Jiang, "Directional water collection on wetted spider silk," *Nature*, vol. 463, pp. 640-643, 2010.
- [58] J. Gao, Y. L. Liu, H. P. Xu, Z. Q. Wang, and X. Zhang, "Mimicking Biological Structured Surfaces by Phase-Separation Micromolding," *Langmuir*, vol. 25, pp. 4365-4369, 2009.
- [59] Y. M. Zheng, X. F. Gao, and L. Jiang, "Directional adhesion of superhydrophobic butterfly wings," *Soft Matter*, vol. 3, pp. 178-182, 2007.
- [60] S. G. Lee, H. S. Lim, D. Y. Lee, D. Kwak, and K. Cho, "Tunable Anisotropic Wettability of Rice Leaf-Like Wavy Surfaces," *Advanced Functional Materials*, vol. 23, pp. 547-553, 2013.

- [61] K. H. Chu, R. Xiao, and E. N. Wang, "Uni-directional liquid spreading on asymmetric nanostructured surfaces," *Nature Materials*, vol. 9, pp. 413-417, 2010.
- [62] M. J. Hancock, K. Sekeroglu, and M. C. Demirel, "Bioinspired Directional Surfaces for Adhesion, Wetting, and Transport," *Advanced Functional Materials*, vol. 22, pp. 2223-2234, 2012.
- [63] L. B. Xu, R. G. Karunakaran, J. Guo, and S. Yang, "Transparent, Superhydrophobic Surfaces from One-Step Spin Coating of Hydrophobic Nanoparticles," *Acs Applied Materials & Interfaces*, vol. 4, pp. 1118-1125, 2012.
- [64] U. A. Gurkan, S. Tasoglu, D. Kavaz, M. C. Demirel, and U. Demirci, "Emerging Technologies for Assembly of Microscale Hydrogels," *Advanced Healthcare Materials*, vol. 1, pp. 149-158, 2012.
- [65] T. I. Kim and K. Y. Suh, "Unidirectional wetting and spreading on stooped polymer nanohairs," *Soft Matter*, vol. 5, pp. 4131-4135, 2009.
- [66] Y. K. Lai, F. Pan, C. Xu, H. Fuchs, and L. F. Chi, "In Situ Surface-Modification-Induced Superhydrophobic Patterns with Reversible Wettability and Adhesion," *Advanced Materials*, vol. 25, pp. 1682-1686, 2013.
- [67] C. A. Stan, L. Guglielmini, A. K. Ellerbee, D. Caviezel, H. A. Stone, and G. M. Whitesides, "Sheathless hydrodynamic positioning of buoyant drops and bubbles inside microchannels," *Physical Review E*, vol. 84, 2011.
- [68] S. H. Lee, H. N. Kim, R. K. Kwak, and K. Y. Suh, "Effects of Mold Rising Angle and Polymer Concentration in Solvent-Assisted Molding," *Langmuir*, vol. 25, pp. 12024-12029, 2009.
- [69] S. J. Choi, K. Y. Suh, and H. H. Lee, "Direct UV-replica molding of biomimetic hierarchical structure for selective wetting," *Journal of the American Chemical Society*, vol. 130, pp. 6312-6313, 2008.
- [70] R. G. Karunakaran, C. H. Lu, Z. H. Zhang, and S. Yang, "Highly Transparent Superhydrophobic Surfaces from the Coassembly of Nanoparticles (≤ 100 nm)," *Langmuir*, vol. 27, pp. 4594-4602, 2011.

- [71] S. M. Kim, D. H. Kang, J. H. Koh, H. S. Suh, H. Yoon, K. Y. Suh and K. H. Char, "Thermoresponsive switching of liquid flow direction on a two-face prism array," *Soft Matter*, vol. 9, pp. 4145-4149, 2013.
- [72] H. S. Kim, C. R. Lee, J. H. Im, K. B. Lee, T. Moehl, A. Marchioro, S. J. Moon, R. H. Baker, J. H. Yum, J. E. Moser, M. Gratzel and N. G. Park, "Lead Iodide Perovskite Sensitized All-Solid-State Submicron Thin Film Mesoscopic Solar Cell with Efficiency Exceeding 9%," *Scientific Reports*, vol. 2, 2012.
- [73] J. Burschka, N. Pellet, S. J. Moon, R. Humphry-Baker, P. Gao, M. K. Nazeeruddin and M. Gratzel, "Sequential deposition as a route to high-performance perovskite-sensitized solar cells," *Nature*, vol. 499, pp. 316-319, 2013.
- [74] M. Z. Liu, M. B. Johnston, and H. J. Snaith, "Efficient planar heterojunction perovskite solar cells by vapour deposition," *Nature*, vol. 501, pp. 395-398, 2013.
- [75] H. P. Zhou, Q. Chen, G. Li, S. Luo, T. B. Song, H. S. Duan, J. Hong, J. You, Y. Liu and Y. Yang, "Interface engineering of highly efficient perovskite solar cells," *Science*, vol. 345, pp. 542-546, 2014.
- [76] N. G. Park, "Organometal Perovskite Light Absorbers Toward a 20% Efficiency Low-Cost Solid-State Mesoscopic Solar Cell," *Journal of Physical Chemistry Letters*, vol. 4, pp. 2423-2429, 2013.
- [77] H. J. Snaith, "Perovskites: The Emergence of a New Era for Low-Cost, High-Efficiency Solar Cells," *Journal of Physical Chemistry Letters*, vol. 4, pp. 3623-3630, 2013.
- [78] M. Gratzel, "The light and shade of perovskite solar cells," *Nature Materials*, vol. 13, pp. 838-842, 2014.
- [79] M. L. Brongersma, Y. Cui, and S. H. Fan, "Light management for photovoltaics using high-index nanostructures," *Nature Materials*, vol. 13, pp. 451-460, 2014.
- [80] J.-G. Kim, H. J. Choi, K.-C. Park, R. E. Cohen, G. H. McKinley, and G. Barbastathis, "Multifunctional Inverted Nanocone Arrays for Non-Wetting,

- Self-Cleaning Transparent Surface with High Mechanical Robustness," *Small*, vol. 10, pp. 2487-2494, 2014.
- [81] K. S. Liu, X. Yao, and L. Jiang, "Recent developments in bio-inspired special wettability," *Chemical Society Reviews*, vol. 39, pp. 3240-3255, 2010.
- [82] H. K. Raut, V. A. Ganesh, A. S. Nair, and S. Ramakrishna, "Anti-reflective coatings: A critical, in-depth review," *Energy & Environmental Science*, vol. 4, pp. 3779-3804, 2011.
- [83] B. Bhushan, Y. C. Jung, and K. Koch, "Self-Cleaning Efficiency of Artificial Superhydrophobic Surfaces," *Langmuir*, vol. 25, pp. 3240-3248, 2009.
- [84] J. G. Cai, J. F. Ye, S. Y. Chen, X. W. Zhao, D. Y. Zhang, S. Chen, Y. Ma, S. Jin and L. Qi, "Self-cleaning, broadband and quasi-omnidirectional antireflective structures based on mesocrystalline rutile TiO₂ nanorod arrays," *Energy & Environmental Science*, vol. 5, pp. 7575-7581, 2012.
- [85] X. F. Gao, X. Yan, X. Yao, L. Xu, K. Zhang, J. H. Zhang, B. Yang and L. Jiang, "The dry-style antifogging properties of mosquito compound eyes and artificial analogues prepared by soft lithography," *Advanced Materials*, vol. 19, pp. 2213-2217, 2007.
- [86] R. S. Wang, H. Q. Tan, Z. Zhao, G. Q. Zhang, L. W. Song, W. F. Dong and Z. C. Sun, "Stable ZnO@TiO₂ core/shell nanorod arrays with exposed high energy facets for self-cleaning coatings with anti-reflective properties," *Journal of Materials Chemistry A*, vol. 2, pp. 7313-7318, 2014.
- [87] B. M. Wang and P. W. Leu, "Enhanced absorption in silicon nanocone arrays for photovoltaics," *Nanotechnology*, vol. 23, 2012.
- [88] Z. Y. Fan, R. Kapadia, P. W. Leu, X. B. Zhang, Y. L. Chueh, K. Takei, K. S. Yu, A. Jamshidi, A. A. Rathore, D. J. Ruebusch, M. Wu and A. Javey, "Ordered Arrays of Dual-Diameter Nanopillars for Maximized Optical Absorption," *Nano Letters*, vol. 10, pp. 3823-3827, 2010.
- [89] Z. Y. Fan, H. Razavi, J. W. Do, A. Moriwaki, O. Ergen, Y. L. Chueh, P. W. Leu, J. C. Ho, T. Takahashi, L. A. Leichert, S. Neale, K. S. Yu, M. Wu, J.

- W. Ager and A. Javey, "Three-dimensional nanopillar-array photovoltaics on low-cost and flexible substrates," *Nature Materials*, vol. 8, pp. 648-653, 2009.
- [90] S. Guldin, P. Kohn, M. Stefik, J. Song, G. Divitini, F. Ecarla, C. Ducati, U. Wiesner and U. Steiner, "Self-Cleaning Antireflective Optical Coatings," *Nano Letters*, vol. 13, pp. 5329-5335, 2013.
- [91] X. Y. Lai, J. E. Halpert, and D. Wang, "Recent advances in micro-/nano-structured hollow spheres for energy applications: From simple to complex systems (vol 5, pg 5604, 2012)," *Energy & Environmental Science*, vol. 5, pp. 9944-9944, 2012.
- [92] J. Zhu, C. M. Hsu, Z. F. Yu, S. H. Fan, and Y. Cui, "Nanodome Solar Cells with Efficient Light Management and Self-Cleaning," *Nano Letters*, vol. 10, pp. 1979-1984, 2010.
- [93] Y. Liu, A. Das, S. Xu, Z. Y. Lin, C. Xu, Z. L. Wang, A. Rohatgi and C. P. Wong, "Hybridizing ZnO Nanowires with Micropyramid Silicon Wafers as Superhydrophobic High-Efficiency Solar Cells," *Advanced Energy Materials*, vol. 2, pp. 47-51, 2012.
- [94] S. M. Kang, C. Lee, H. N. Kim, B. J. Lee, J. E. Lee, M. K. Kwak and K. Y. Suh, "Directional Oil Sliding Surfaces with Hierarchical Anisotropic Groove Microstructures," *Advanced Materials*, vol. 25, pp. 5756-5761, 2013.
- [95] C. H. Liu, P. L. Niu, and C. K. Sung, "Integrating anti-reflection and superhydrophobicity of moth-eye-like surface morphology on a large-area flexible substrate," *Journal of Physics D-Applied Physics*, vol. 47, 2014.
- [96] E. Garnett and P. D. Yang, "Light Trapping in Silicon Nanowire Solar Cells," *Nano Letters*, vol. 10, pp. 1082-1087, 2010.
- [97] Y. Yao, J. Yao, V. K. Narasimhan, Z. C. Ruan, C. Xie, S. H. Fan and Y. Cui, "Broadband light management using low-Q whispering gallery modes in spherical nanoshells," *Nature Communications*, vol. 3, 2012.
- [98] Y. M. Song, Y. Z. Xie, V. Malyarchuk, J. L. Xiao, I. Jung, K. J. Choi, Z. Liu, H. S. Park, C. F. Lu, R. H. Kim, R. Li, K. B. Crozier, Y. Huang and J.

- A. Rogers, "Digital cameras with designs inspired by the arthropod eye," *Nature*, vol. 497, pp. 95-99, 2 2013.
- [99] H. Yoon, S. G. Oh, D. S. Kang, J. M. Park, S. J. Choi, K. Y. Suh, K. H. Char and H. H. Lee, "Arrays of Lucius microprisms for directional allocation of light and autostereoscopic three-dimensional displays," *Nature Communications*, vol. 2, 2011.
- [100] S. F. Ahmed, G. H. Rho, K. R. Lee, A. Vaziri, and M. W. Moon, "High aspect ratio wrinkles on a soft polymer," *Soft Matter*, vol. 6, pp. 5709-5714, 2010.
- [101] J. B. Kim, P. Kim, N. C. Pegard, S. J. Oh, C. R. Kagan, J. W. Fleischer, H. A. Stone and Y. L. Loo, "Wrinkles and deep folds as photonic structures in photovoltaics," *Nature Photonics*, vol. 6, pp. 327-332, 2012.
- [102] J. H. Im, C. R. Lee, J. W. Lee, S. W. Park, and N. G. Park, "6.5% efficient perovskite quantum-dot-sensitized solar cell," *Nanoscale*, vol. 3, pp. 4088-4093, 2011.
- [103] S. Y. Heo, J. K. Koh, G. Kang, S. H. Ahn, W. S. Chi, K. Kim and J. H. Kim, "Bifunctional Moth-Eye Nanopatterned Dye-Sensitized Solar Cells: Light-Harvesting and Self-Cleaning Effects," *Advanced Energy Materials*, vol. 4, 2014.
- [104] J. W. Leem, S. Kim, S. H. Lee, J. A. Rogers, E. Kim, and J. S. Yu, "Efficiency Enhancement of Organic Solar Cells Using Hydrophobic Antireflective Inverted Moth-Eye Nanopatterned PDMS Films," *Advanced Energy Materials*, vol. 4, 2014.
- [105] J. W. Lee, D. J. Seol, A. N. Cho, and N. G. Park, "High-Efficiency Perovskite Solar Cells Based on the Black Polymorph of $\text{HC}(\text{NH}_2)_2\text{PbI}_3$," *Advanced Materials*, vol. 26, pp. 4991-4998, 2014.
- [106] D. Y. Son, J. H. Im, H. S. Kim, and N. G. Park, "11% Efficient Perovskite Solar Cell Based on ZnO Nanorods: An Effective Charge Collection System," *Journal of Physical Chemistry C*, vol. 118, pp. 16567-16573, 2014.

국문초록

본 학위 논문에서는 자연모사 방식의 멀티스케일 설계 및 제작 기술을 통하여 옴니포빅(superomniphobic) 표면을 개발하고 이를 에너지 디바이스 플랫폼에 적용하는 것을 목적으로 하였다. 고분자 마이크로/나노 패터닝 기술을 이용하여 구조적인 설계와 더불어 표면의 화학적 처리를 통하여 초소수성(superhydrophobic) 및 초발유성(superoleophobic) 표면을 제작하고 마이크로 유체역학을 기반으로 이론적인 분석을 함께 진행하였다. 이와 같이 제작된 자연모사 고분자 표면의 초발유성, 비대칭의 방향성 있는 액적 유동, 자가 세정, 반사 방지 효과 등의 다양한 옴니포빅 성질을 이용한다면 산업계와 에너지 디바이스 분야에 유용하게 적용할 수 있다.

먼저, 본 논문에서는 자연모사 기반의 고분자 옴니포빅 표면을 제작하기 위해 재현성과 신뢰성이 뛰어나고 복잡하지 않은 건식 식각 방식을 제시하였다. 건식 접착제를 비롯한 다양한 분야에 응용되고 있는 게코(gecko) 도마뱀의 발바닥의 섬모 형태는 끝 단이 평평한 마이크로 기둥모양의 버섯 형태의 요각(re-entrant) 구조로 이루어져 있고 이를 옴니포빅 표면에 적용하였다. 전통적인 건식 식각 방식을 이용하여 산화실리콘(SiO_2) 식각 정지 층(etching stop layer)을 지니는 실리콘 웨이퍼를 실제 깊이보다 더 깎아 들어가는 과도 식각(over-etching)방법으로 식각 정지 층과 인접한 실리콘 층을 기본 패턴의

지름보다 넓히고, 이를 유연하고 투명한 고분자로 전사하여 옴니포빅 표면을 제작하였다. 제작된 고분자 옴니포빅 표면의 성질을 측정하기 위해 물부터 에탄올까지 다양한 표면 장력을 지니는 액체들에 대한 접촉각(static contact angles)과 이력각(contact angle hysteresis)을 측정하여 학계가 인정하는 옴니포빅 표면의 기준인 접촉각 $> 150^\circ$, 이력각 $< 10^\circ$ 를 만족함을 보였다. 또한 해당 표면의 투과도 및 장기 안정성 측정을 통해 다양한 응용분야로의 가능성도 확인할 수 있었다.

다음으로, 본 논문에서는 벚잎(rice leaf)의 표면 구조에서 영감을 얻어 요각 형태의 마이크로 선형 구조를 제작하여 옴니포빅 성질과 비대칭의 방향성 있는 액적의 유동을 함께 보여주었다. 저가의 손쉽게, 대면적 공정이 가능한 산화 알루미늄(Al_2O_3) 나노 입자가 포함된 UV 경화성 폴리머 패터닝 방식을 이용하여 마이크로/나노 계층 선형 구조를 제작하였다. 물 뿐만 아니라 오일 또한 젖지 않고 한쪽 방향으로 흘러내리는 표면을 개발하기 위해 프리즘, 직사각형, 요각 구조의 세 가지 형태의 절단면을 지니는 마이크로 선형 계층구조를 제작하여 실험을 진행하였다. 프리즘 형태의 절단면을 지니는 선형 계층 구조의 경우, 기존의 자연계에서 존재하는 벚잎의 기능과 유사한 접촉각 및 구름각을 나타내었으며 절단면의 형태가 요각 구조인 경우, 물 뿐만 아니라 오일까지 한쪽방향으로 젖지 않고 흐르는 비대칭 옴니포빅 성질을 보였다. 이에 더불어, 반도체 산업 현장에서 많이 사용되는 포토감광용액(photoresist)에 대한 방향성 옴니포빅 실험을

진행하여 성공하였고, 원하는 형태의 다양한 선형을 제작하여 표면상에서 물과 오일이 각각의 경로를 따라 젖지 않고 이동하는 현상을 보여주었다. 이는 제작된 요각 구조의 선형 마이크로/나노 계층 표면이 학문적으로 의미가 있을 뿐만 아니라, 반도체 업계 및 송유관 시스템 등의 구체적인 산업 현장에 적용될 수 있음을 암시하였다.

마지막으로, 이러한 초소수성 및 초발유성 표면을 제작하여 페로브스카이트(perovskite) 태양 전지와 같은 에너지 디바이스로 적용할 수 있는 방법에 대해 논의하였다. 연꽃잎(lotus leaf)의 이중 계층 구조를 본 떠 휘어짐 특성이 좋고 투과도가 좋은 PDMS 고분자를 이용하여 마이크로/나노 계층 피라미드 구조를 제작하고 이를 페로브스카이트 태양 전지의 유리판에 부착하여 성능의 향상을 유도하였다. PDMS 마이크로 피라미드 구조를 전통적인 실리콘-폴리머 전사 방식을 통하여 제작하고 표면의 아르곤(Ar) 플라즈마 처리 방식을 이용하여 나노 주름을 덧입혀 마이크로/나노 피라미드 계층 구조를 형성할 수 있었다. 이렇게 형성된 마이크로 피라미드 구조 위의 나노 주름 구조는 기존의 피라미드 구조에 의한 반사 방지 기능과 더불어 ‘연꽃잎 효과(Lotus effect)’라고 불리는 자가 세정 기능까지 나타내어 태양광을 통해 에너지를 발생시키는 페로브스카이트 태양 전지의 성능 향상에 일조하였다. 반사 방지 기능을 통해 태양 전지 디바이스 안으로 흡수되는 태양빛의 양을 증가시켰고, 자가 세정 기능을 통해 먼지나 유해 물질에 의한 외부 오염으로부터 태양 전지의 유리판을 지켜주는

역할을 한다. 또한 PDMS 고분자의 특징인 높은 반데르 발스 힘(Van der Waals force)을 통해 페로브스카이트 태양 전지의 유리판에 추가적인 접착제 없이 손쉽게 탈·부착이 가능하여 투명 기판을 사용하는 다양한 에너지 산업에 유용하게 사용할 수 있음을 확인하였다.

주요어: 자연모사, 요각 구조, 버섯 구조, 연꽃잎 효과, 옴니포빅, 비대칭 액적 유동, 비대칭 젖음 현상, 멀티스케일 계층 구조, 자가세정, 반사 방지, 페로브스카이트 태양 전지

학번: 2010-20648